Heliogyro Control

Richard S. Blomquist

CMU-RI-TR-yy-xx

Submitted in partial fulfillment of the
requirements for the degree of
Doctor of Philosophy in Robotics

The Robotics Institute
Carnegie Mellon University
Pittsburgh, Pennsylvania 15213

April 2009

Dissertation Committee:
William L. Whittaker, Chair
Dimitrios Apostolopoulos
George Kantor
Andreas von Flotow

© 2009 Richard S. Blomquist. All rights reserved.

Abstract

Heliogyros with blade length-to-width aspect ratios of 1000 can achieve ambitious science mission goals, but such designs have not been analyzed with rigor. Archived heliogyro analyses indicate that aspect ratios of 1000 are feasible, but the calculations supporting this claim are based on the simplifying assumptions of decoupled twist, vertical deflection, and in-plane deflection of the blades. In making such simplifications, the equations become more tractable, but crucial behavioral characteristics are possibly lost. Without a more rigorous analytical investigation, the reliability and robustness of the heliogyro remains in doubt. However, with verified control models and an appropriate operations strategy, performance of aggressive heliogyro designs can be presumed. This thesis asserts that heliogyro blades with aspect ratios of 1000:1 can sufficiently operate in space. The crux of this investigation is a high-fidelity model that accurately represents a heliogyro blade. Pitch controls command the thrust vector of the large sail structure. Although the validation model mimics a real solar sail, the controller is driven toward the most simplified configuration. The results of this research validate that a model-based controller that neglects blade twist, coning, and wrinkling can sufficiently control the thrust vector of a suitably designed heliogyro.

Acknowledgments

I would like express my deepest appreciation for everyone who supported me in this task. First, to Sarah, my wife, who provided the love and support required to finish I thank you most in this world. Then, to Red, who saw me through to the end, thank you. Thanks to Dimi, George, and Andy, Dot, Michele, and all the students who worked on Solar Blade. A special thank you goes to Dan Dewey, who provided over 20 Macs for me to run particle blade simulations. Another special thanks goes out to Sarah's family and my family, especially Phil, Mary, Elijah (cuteness level 1000000000000) and Caleb. Big help! Everyone, big thanks!

Dedication

To Sarah

Table of Contents

Abstract **i**

Acknowledgements **ii**

List of Figures **viii**

List of Tables **x**

1 Introduction **1**

1.1 Motivation 1

1.2 Thesis Statement 3

1.3 History 6

1.4 Technical Approach and Methodology 9

1.5 Notation 10

2 Numerical Models **12**

2.1 MacNeal's Equations 14

2.1.1 Twist Behaviors 18

2.1.2 Vertical Deflection Behaviors 21

2.1.3 Inplane Deflection Behaviors 23

2.1.4 Calculated Behavior of a Sample Heliogyro 24

2.2 Stiff Blade Heliogyro 24

2.3 Particle Blade 31

2.4 Kane Blade Heliogyro 44

2.4.1 Core 45

2.4.2 Blade 46

3 Blade Behavior **59**

3.1 Twist 59

3.2 Tip Pitch vs. Root Pitch 64

3.3 Step Response 74

3.4 Chord-wise Blade Curl 75

4 Pitch Control **78**

4.1 Requirements 78

4.2 Design and Analysis 84

4.3 Implementation 91

5 Conclusions **97**

5.1 Impact/Significance 97

5.2 Future Work 97

BIBLIOGRAPHY **99**

APPENDICES **104**

A Pitch Parameter Transition **105**

B Particle Forces and Their Derivatives **110**

B.1 Spring Force 110

B.2 Damping Force 112

B.3 Gravitational Force 113

B.4 Solar Force 113

C Sinusoid_fit.m: A Matlab Script for Sinusoid Curve Fitting. [16] **116**

D Sine Fit Parameters **118**

List of Figures

1.1 Three types of solar sail. 2
1.2 Original heliogyro concept [21]. 7

2.1 Rigid blade rotating about a longitudinal axis. 13
2.2 Pitch response for varying initial stiff blade pitch angles. 14
2.3 Free-body diagram of a differential element under centripetal stress 15
2.4 Centripetal force on a two dimensional differential element. [21] 16
2.5 Nondimensional, steady-state twist curve. 20
2.6 Twist vs. Relative Pitch Frequency. 21
2.7 Nondimensional vertical deflection curves. 23
2.8 Heliogyro with reference frames. 26
2.9 Shear force diagram for a square in a membrane mesh. 36
2.10 Batten implementation in heliogyro blade [22] 39
2.11 Spring configuration for a batten, incorporated into the mesh of tension and shear springs that comprise a section of blade. The linear batten springs appear as three lines together. 40
2.12 Nonlinear stiffness relation for various values of K. 41
2.13 Heliogyro model corresponding to Kane derivation. 44
2.14 Frames for Single Blade Derivation. 47
2.15 The use of ζ and s to describe stretch of a blade. 52

3.1 Ratio of twist to twist at root for different blade lengths, and for solar pressure present and not present. Solar pressure makes negligible difference. 61
3.2 Nonlinear stiffness factors at the blade root for the 100 m and 1000 m blades spinning at 2 rpm. 62

3.3 Twist curves for 100 meter and 1000 meter blades with same blade root stress. Twist curve for 100 meter blade with same spin rate as 1000 meter blade appears as a reference. 63
3.4 Nonlinear curve fit of twist at tip and at 90% of span for a 1000m blade, pitch rate = 0.6*rotation rate, solar pressure present. Plots a, b, and c are for the tip and d,e, and f are for the 90% point. 66
3.5 Ratio of tip twist amplitude to root pitch amplitude vs. ratio of root pitch frequency to heliogyro rotation frequency. 67
3.6 Twist response at tip and 90% along the span due to a step decrease at the root from 0.52 radians (30 degrees) to 0.44 radians (25 degrees) over one radian of rotation. 74
3.7 Comparison of 1000 m blades, one with battens and one without. These are snapshots of the blades after 55 rotations around a vertical axis. 76

4.1 Cyclic Pitch Maneuver. [21] 80
4.2 Collective-cyclic Pitch Maneuver. [21] 81
4.3 Collective Pitch Maneuver. [21] 82
4.4 Half-P Pitch maneuver. [21] 83
4.5 Diagram of pitch controller. 85
4.6 Model diagram of pitch controller. Main actuator is above, secondary is below. 86
4.7 Tracking of the main actuator (top) and the secondary actuator (bottom) to a sinusoidal reference. 90
4.8 Schematic diagram of pitch controller. 92
4.9 Arrangement of axial, in-plane and vertical spring-dampers, attached to pitch controller. 93
4.10 Pitch controller tracking a reference input. On the left are the reference and the main actuator responses only. On the right are the reference, the main and secondary actuators, and blade responses. Top to bottom: collective to cyclic transition (a, b);cyclic (c, d); and step (e, f). 94
4.11 Z axis tracking path for 3-blade heliogyro with stiff 100 m blades spinning at 1 rpm. The entire trajectory takes approximately 25 hours. 96

A.1 Sine function for transition scaling factor 106
A.2 Transition applied between two profiles 109

List of Tables

1.1 Three solar sail-enabled missions. 4
1.2 Possible heliogyro parameters for Sun-Earth sub-L1, solar-polar, and interstellar missions. 5

2.1 First four natural frequencies for twist, vertical deflection, and in-plane deflection. 24
2.2 Sample heliogyro. 25
2.3 Partial velocities for the stiff-blade model. 30

3.1 Correlation of parameters ϕ between blade root, blade tip, and 90% of span for a 10 meter blade undergoing cyclic pitch and with no solar pressure present. Primary and Secondary curve fits are included. 68
3.2 Correlation of parameters ϕ between blade root, blade tip, and 90% of span for a 10 meter blade undergoing cyclic pitch and with solar pressure present. Primary and Secondary curve fits are included. 69
3.3 Correlation of parameters ϕ between blade root, blade tip, and 90% of span for a 100 meter blade undergoing cyclic pitch and with no solar pressure present. Primary and Secondary curve fits are included. 70
3.4 Correlation of parameters ϕ between blade root, blade tip, and 90% of span for a 100 meter blade undergoing cyclic pitch and with solar pressure present. Primary and Secondary curve fits are included. 71
3.5 Correlation of parameters ϕ between blade root, blade tip, and 90% of span for a 1000 meter blade undergoing cyclic pitch and with no solar pressure present. Primary and Secondary curve fits are included. 72
3.6 Correlation of parameters ϕ between blade root, blade tip, and 90% of span for a 1000 meter blade undergoing cyclic pitch and with solar pressure present. Primary and Secondary curve fits are included. 73

3.7 Comparison of parameters ϕ between blade root, blade tip, and 90% of span for a 1000 meter blade with battens spaced every 50 m and a 1000 m blade without battens. The blades are undergoing cyclic pitch; no solar pressure is present. 77

4.1 Viable motor characteristics. 91

A.1 Values of a and b for parameter sets A and B 107
A.2 Two example pitch profile parameter sets A and B 107

D.1 Primary parameters ϕ for blade root, blade tip, and 90% of span for a 10 meter blade undergoing cyclic pitch and with no solar pressure present. . . 119
D.2 Primary parameters ϕ for blade root, blade tip, and 90% of span for a 10 meter blade undergoing cyclic pitch and with solar pressure present. 120
D.3 Primary parameters ϕ for blade root, blade tip, and 90% of span for a 100 meter blade undergoing cyclic pitch and with no solar pressure present. . . 121
D.4 Primary parameters ϕ for blade root, blade tip, and 90% of span for a 100 meter blade undergoing cyclic pitch and with solar pressure present. 122
D.5 Primary parameters ϕ for blade root, blade tip, and 90% of span for a 1000 meter blade undergoing cyclic pitch and with no solar pressure present. . . 123
D.6 Primary parameters ϕ for blade root, blade tip, and 90% of span for a 1000 meter blade undergoing cyclic pitch and with solar pressure present. 124
D.7 Primary parameters ϕ for blade root, blade tip, and 90% of span for a 1000 meter blade with battens every 50 m undergoing cyclic pitch and with no solar pressure present. 124
D.8 Secondary parameters ϕ for blade root, blade tip, and 90% of span for a 10 meter blade undergoing cyclic pitch and with no solar pressure present. . . 125
D.9 Secondary parameters ϕ for blade root, blade tip, and 90% of span for a 10 meter blade undergoing cyclic pitch and with solar pressure present. 126
D.10 Secondary parameters ϕ for blade root, blade tip, and 90% of span for a 100 meter blade undergoing cyclic pitch and with no solar pressure present. . . 127
D.11 Secondary parameters ϕ for blade root, blade tip, and 90% of span for a 100 meter blade undergoing cyclic pitch and with solar pressure present. 128
D.12 Secondary parameters ϕ for blade root, blade tip, and 90% of span for a 1000 meter blade undergoing cyclic pitch and with no solar pressure present. . . 129

D.13 Secondary parameters ϕ for blade root, blade tip, and 90% of span for a 1000 meter blade undergoing cyclic pitch and with solar pressure present. 130
D.14 Secondary parameters ϕ for blade root, blade tip, and 90% of span for a 1000 meter blade with battens every 50 m, undergoing cyclic pitch and with solar pressure present. 130

Chapter 1

Introduction

1.1 Motivation

Dwelling at artificial LaGrange points, investigating the poles of the Sun, and interstellar travel promise to unlock secrets of the universe, such as the origin of the solar system, connections between the Earth and the Sun, requirements for life, and the possibility of other intelligent life in space. Each is enabled by as yet unproven solar sail technology.

Solar sailing makes possible exotic missions once thought impractical due to large propellant requirements. The advantage of solar sailing in space lies in the continuous propulsion derived from natural solar pressure. Although the pressure from the Sun is less than the pressure felt from a piece of paper on an open hand, its persistent push imparts an accumulated thrust greater than rocket propulsion can provide.

Solar sail concepts have existed for decades, but their implementation has been elusive; to date, no true solar sail craft have flown in space. Because the photon pressure is so low, sails with enormous area-to-mass ratios are required to develop sufficient propulsive power. As the area-to-mass ratio increases, sailcraft flexibility and operational complexity also increase. Shifting centers of dynamic pressure from structural vibrations, sail billow, and imperfections in the sail structure make the solar sail thrust vector hard to predict. The problems may be reduced by adding structure to the sail to make it more flat, stiff, and strong; however, this brings the unwelcome effect of driving sail weight up and performance down.

Spacecraft miniaturization over time has dramatically reduced spacecraft payload mass, shrinking sail size requirements and overall spacecraft mass. The size and weight reduction

now makes solar sail designs eminently more practical and flyable; yet, sail control capability is still lacking.

As a consequence of their flexibility, solar sails, like other gossamer spacecraft, demand surface activation and persistent control attention. Validated solar sail models for this purpose do not exist, because the nonlinear behavior of sails is difficult to ascertain and the gravitational and atmospheric effects on Earth make meaningful preflight deployment and operations tests difficult to conduct. Even with a proper sail model, continuous ground control of gossamer structures during a years-long mission is impractical. These factors combine to create the need for high-fidelity analytical models and onboard solar sail guidance, navigation, and control.

The choice of solar sail has a dramatic effect on the ability to solve the control and deployment issues. Of the three main types of solar sails − the heliogyro, the three axis stabilized square sail, and the spinning disk − the heliogyro has the most understood control strategy and is the least risky to deploy. The heliogyro has the appearance of a Dutch windmill and employs sail control akin to a helicopter. Its multiple solar reflecting blades are attached to a central spacecraft bus and are pitched along their radial axis. Each blade is constructed from ultrathin, highly reflecting film. Deployment consists of spinning up the heliogyro core and unrolling each blade from its spool. During operation, centripetal tension and chord-wise battens provide stiffness and embedded Kevlar rip-stops resist tearing. The spinning sailcraft uses collective and cyclic pitch of these solar blades to control attitude and thrust.

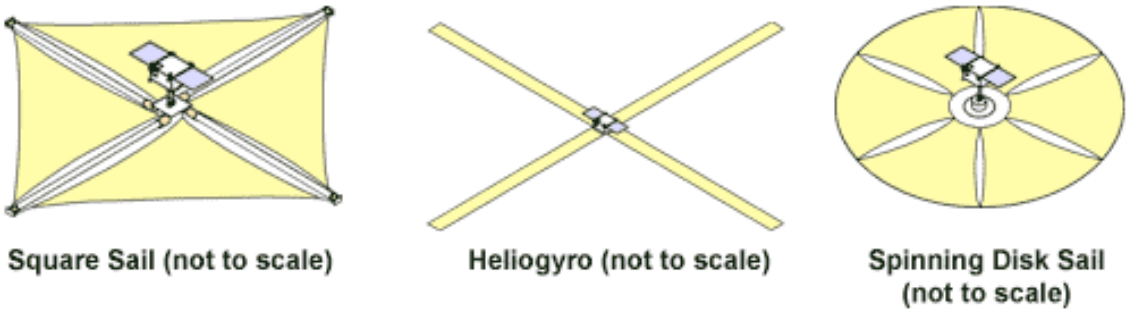


Figure 1.1: Three types of solar sail.

The heliogyro, the concept of choice for this research, is inherently advantaged for near-

term space flight. Its ability to feather its blades enables highly efficient hovering around an artificial LaGrange point and drag minimization during Sun-ward trajectories. It is also favored for pole-sitting missions, where a position over a planetary pole is maintained.

Performance requirements for solar sail-enabled missions indicate that solar sailcraft with total mass-to-area ratios ranging from 25 g/m^2 down to 2 g/m^2 are necessary to adequately propel their payloads. For spacecraft with total accelerated mass in the range of 250 to 450 kg, this translates to solar sail areas on the order of $10,000$ to $100,000$ m^2. As a reference, propulsion requirements and a typical description of Sun-Earth sub-L1, solar polar, and interstellar heliosphere probe missions appear in Table 1.1. Applied to the heliogyro concept, these missions can be accomplished with blade aspect ratios less than 1000:1. A list of possible heliogyro parameters for the three missions appears in Table 1.2.

In comparison to square sails, heliogyros require less sail subsystem mass, and therefore result in a lower overall spacecraft mass, due to the lack of structure needed to suspend the sail material. Centripetal stiffness resists bending of the blades; chord-wise battens prevent curling and provide some resistance to twist. Together, they help keep the blade sufficiently straight and flat for thrust control.

The proposed heliogyro configurations in Table 1.2 are within the proposed limit of heliogyro capability. Archived heliogyro analyses indicate that a heliogyro with 6 to 24 blades, blade thickness of 1 micron, and a length-to-width aspect ratio of 10000 or more should be controllable.[21][22] The calculations supporting this claim are based on the simplifying assumptions of decoupled twist, vertical deflection, and in-plane deflection of the blades. In making such simplifications, the equations become more tractable, but possibly crucial behavioral characteristics are lost. Without a more rigorous analytical and empirical investigation, the reliability and robustness of heliogyro control remains unknown. However, with verified control models and an appropriate operations strategy, aggressive heliogyro designs can be proven.

1.2 Thesis Statement

Heliogyro blades with aspect ratios of 1000:1 can sufficiently operate in space. Blade behavior is sufficiently benign to allow thrust vector control. The blade aspect ratio and surface mass-to-area ratio provide thrust and precession performance sufficient to meet control

Table 1.1: Three solar sail-enabled missions.

	Sun-Earth Sub-L1	Solar Polar	Interstellar Heliosphere
Total S/C mass, kg	298	450	246
S/C mass, w/o sail, kg	251	300	150
Sail subsystem mass, kg	47	150	96
Sail area, m^2	10000	25600	96000
Sail areal density, g/m^2	4.7	5.9	1.0
S/C characteristic acceleration, mm/s^2	0.245	0.415	2.85
Max cone angle, deg	45	50	
Max precess/slew rate, deg $/day$	9	100	
Closest distance to Sun, AU	0.97	0.4	0.25
Farthest distance from Sun, AU	1	1	5
Sun-Earth Sub-L1	Sensors indicate Coronal Mass Ejection events (CME's) at a location Sunward of the L1 Lagrange point to provide greater warning time to facilities on Earth harmed by a CME. The solar sail provides an offset to the solar gravitational pull, creating an artificial Lagrange point where all external forces on the spacecraft balance.		
Solar Polar	Spacecraft analyzes the poles of the Sun from a 75 ° inclined orbit. The solar sail causes the spacecraft to spiral to within 0.4 AU of the Sun, and then cranks the spacecraft orbit to 75 °.		
Interstellar Heliosphere Probe	An investigation of the heliosphere, the mission entails a spacecraft passing to within 0.25 AU of the Sun, then sprinting radially outward to 200 AU within 15 years.		

Table 1.2: Possible heliogyro parameters for Sun-Earth sub-L1, solar-polar, and interstellar missions.

	Sun-Earth Sub-L1	Solar Polar	Interstellar Heliosphere
Number of blades	12	12	24
Blade chord, m	2	2	2
Blade length, m	415	960	2000
Total sail area, m^2	$9,960$	$23,040$	$96,000$
Blade thickness, μm	3.00	3.00	0.670
Blade density, kg/m^2	1400	1400	1400
Rotational period, s	30	480	120
Sail subsystem mass, kg	45	101	96
Non-sail mass, kg	251	300	150
Total S/C mass, kg	296	401	246
Sail areal density, g/m^2	4.5	4.38	1.00
S/C characteristic acceleration, mm/s^2	0.246	0.419	2.85
Precess rate, deg/day	15.3	105.5	56.7

requirements specified in Table 1.2.

The crux of this investigation is a high-fidelity model that accurately represents a heliogyro blade. The research goal is to determine whether a model-based controller that neglects blade twist, coning, and wrinkling can sufficiently control heliogyro blades.

1.3 History

In 1967, a white paper introduced the heliogyro concept with a design weighing 250 kg and consisting of two blades 5700 meters long, 1.5 meters wide, and 6 microns thick [21]. Figure 1.2 contains a sketch of the original design. Neglecting structural dynamics, the paper included uncoupled equations to characterize static blade deformation, control behavior, deployment strategies and orbital maneuvers. Preliminary estimates indicated the time required for planetary escape and round-trip Mars missions using the heliogyro. With no limits on blade aspect ratio, the paper suggested that large, advanced configurations weighing over 45,000 kg and spanning 74 km are possible.

Several years later, a structural dynamics analysis, written as a foundation for engineering development and a further indication of feasibility, utilized uncoupled beam equations to characterize in-plane bending, vertical bending, and twist [22]. Modal analyses confirmed the enabling factor for the heliogyro: when pitched at the same frequency as the heliogyro rotation rate, the blade tip tends to twist at the same frequency, amplitude, and phase as the blade root. The presence of resonant frequencies in the range of operation and the absence of inherent damping in the blades necessitated damper sizing for pitch, in-plane bending, and vertical bending. A blade retention system incorporating the dampers provided a conceptual design for damping hardware.

Mechanical coupling of modes, chordwise curl, and dynamic response to maneuvers appeared at the end of the structural analysis, along with the results of an experimental program. Within a spinning room, a sample blade 196 cm long, 5 cm wide, and 80 microns thick successfully completed pitch maneuvers. Results of the spinning-blade actuation tests compared favorably with the predicted dynamic response. The analysis concluded that the heliogyro is technically feasible.

Heliogyro development progressed past paper studies. As a response to a solar sail-enabled comet rendezvous possibility discovered in the mid 1970's, a 12-blade heliogyro

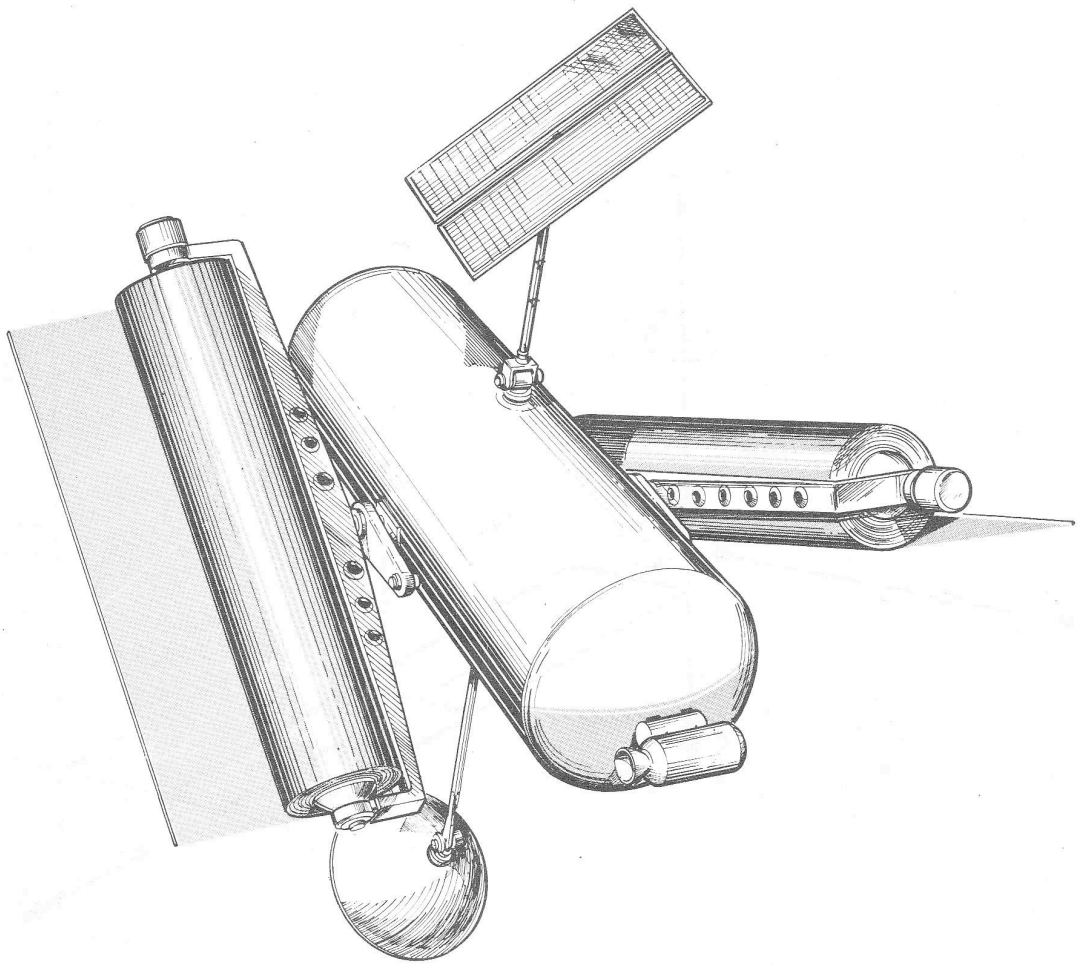


Figure 1.2: Original heliogyro concept [21].

design was undertaken [11]. To sufficiently drive the 3800 kg non-sail mass, each blade was 7500 meters long and 8 meters wide. Two tiers of 6 blades at opposite ends of a cylindrical structure counterrotated to eliminate gyroscopic stiffness, and thus allow the sail to more rapidly precess its spin vector. This scheme also removed nutation and other disturbances that rotate the spacecraft.

It is clear from the design that a framework to keep the blade taut and relatively flat was considered essential. Quad-redundant edge stiffeners not only off-loaded the excessive blade stress, but they also worked together with parabolic tendons, constant tension springs, and battens to pull the blade material taut. The analysis at the time also indicated that edge stiffeners improved uniform cyclic pitch of the blade. However, such a complex design choice decreased the reliability of deployment and drove the weight up. A significantly smaller payload could have led to a simpler design without the parabolic tendons and tension springs. In the end, development halted due to perceived risk [11].

The heliogyro for the comet rendezvous showed the fundamental flaw with sail designs at the time. The payloads were so heavy that the sails to drive them were impractical. A decade later, a different design tack emerged, focusing on relatively tiny heliogyros for low-risk demonstration missions. Driven by a call from the Columbus Quincentenary Jubilee Commission to commemorate the 500th anniversary of Columbus discovering America, a heliogyro with 8 blades, each 100 m long and 1.5 m wide, answered the call for participation in a race to Mars [35]. The novel contributions from this design included a solid-state blade actuation system consisting of two strips of piezoelectric material, one attached from the spacecraft core to the leading edge of the blade root and the other from the spacecraft to the trailing edge of the blade root. When voltage is applied, one piezo strip bends up and the other bends down. Since the pitch force was on the order of 0.1 mN-m, such a flimsy actuator was deemed viable.

With blades 100 m long, no extra support such as edge stiffeners appeared in the design. Analysis showed that deployment of the blades is a straightforward process of slowly unrolling the material, as long as tensile stress along the trailing edge is maintained [3].

1.4 Technical Approach and Methodology

By combining high fidelity off-line modeling and on-line autonomy, layered controls can precisely point the thrust vector of large heliogyros. Such systems can be guided by an outer loop of autonomous mission control which combines high level mission goals with other factors, such as dynamic solar pressure and spacecraft/Earth geometry, to enable robust operations. The foundation for their success, however, is accurate blade pitch models and sufficient blade pitch controls.

The chosen approach to show blade viability is to model heliogyro behavior and use the model to investigate mechanical and control issues. The resulting pitch controller is shown to operate the thrust vector of heliogyro models.

Three analytical models are created: one for the control law, one for blade behavior investigation, and one for control verification. The three models provide different levels of fidelity that work to cross-check each other.

The control law model assumes no blade coning, no blade twist, and no chordwise blade curling. The solar pressure impinging on a heliogyro blade will cause the blade to deform out of plane of the sailcraft, away from the Sun; spinning the heliogyro fast enough to limit coning to approximately 1 degree while maintaining a noncritical blade stress allows for the no-coning assumption. Holding the blade root at a constant collective pitch angle theoretically generates a twist along the blade. With the blade constantly pitching, however, its effect is ameliorated. A remaining issue is to sufficiently dampen harmonic excitations. Incorporated into the blade design are chordwise battens intermittently spaced along the length. Along with providing some resistance to blade twist when the blade is tensioned, they also keep the blade sufficiently flat to allow curling to be ignored.

A finite-difference model consisting of a mesh of particles attached by nonlinear springs is the framework for blade behavior investigation. Based on continuum mechanics, this model allows for large deflections and inherently couples axial, twist, and bending effects. The model is stable where finite element models of microns-thick membranes are not. It provides information regarding blade twist, tip-to-root pitch uniformity, and blade curl.

The verification model is a reasonable representation of a spaceworthy heliogyro. The model arises from the combination of an assumed modes method and Kane's equations. The coupled axial deflection, twist, and deflection provide adequate fidelity to verify heliogyro

control. This model includes the core structure, blade actuators and flexible blades, within a solar environment

Using the validated mesh model, blade twist is numerically computed and compared with analytical results. The degree to which the blade tip follows the blade root in pitch is shown. The response to a step increase in blade pitch provides system information. Inspection of blade shape illustrates the extent that blade curl is an issue. The result is compared to a blade with chordwise battens.

In control system development, the pitch mechanism is designed to provide control of four heliogyro maneuvers: cyclic pitch, collective-cyclic pitch, collective pitch, and half-p pitch. Each maneuver has a small number of parameters and results in a net force and/or torque being applied to the spacecraft. Using these maneuvers, a controller accepts desired force and torque values and finds the appropriate parameter settings to achieve them.

Incorporated into the control model is a model-based pitch controller that dampens low pitch frequency modes and drives the blade root holder to follow the specified sinusoidal pitching trajectory. Consisting of dual actuators and a spiral watch spring, the controller is at once sensitive and robust.

The culmination of the work is a demonstration that blades with large length-to-width aspect ratios are controllable. The pitch controller guides the heliogyro on a trajectory in space.

1.5 Notation

Throughout the dissertation the text uses the following notation. The 3×3 matrix, ${}^{A}R_{B}$, represents the rotation matrix from the B reference frame to the A reference frame. Each reference frame is capitalized and may have a subscript, i, indicating to which heliogyro blade the reference frame is attached. A deviation from this rotation matrix notation is the case in which a rotation matrix is represented by $R_j(\theta)$, where $j = x$, y, or z refers to a rotation of θ radians solely about the x, y, or z axis.

The position vector, ${}^{A}\vec{P}_{BC}$, is the vector from point B to point C in the A reference frame. An uppercase B or C refers to the origin of a reference frame, and a lowercase b or c refers to a particular point other than a reference frame origin. Velocity vectors and acceleration vectors have the same form, with $\dot{}$ or $\ddot{}$ included, as in ${}^{A}\dot{\vec{P}}_{BC}$ and ${}^{A}\ddot{\vec{P}}_{BC}$. Angular

velocity and angular acceleration follow the same form as the position vector notation, with ω and α respectively replacing P.

The transpose of a matrix or vector appears as a superscript to the right of the matrix or vector, as in ${}^{A}R_{B}{}^{T}$, $R_{x}{}^{T}(\theta)$, and ${}^{A}\vec{P}_{BC}{}^{T}$.

Chapter 2

Numerical Models

The uniform motion of each heliogyro blade is due to the fundamental pitch frequency of a rotating beam exactly matching its rate of rotation. This phenomenon is illuminated by the following example. In Figure 2.1, consider a thin rigid blade driven at a constant rate about a rotational axis and unconstrained in longitudinal pitch. The rotational axis and the pitch axis are perpendicular to one another. The blade coning angle, β, is zero and the initial pitch angle is θ. As the system rotates with angular velocity Ω, the blade pitches sinusoidally. The equation of motion for this system is:

$$\ddot{\theta} + \frac{1}{2} c \sin 2\theta = 0 \tag{2.1}$$

where I_x, I_y, and I_z are the mass moments of inertia of the blade and

$$c = \frac{(I_z - I_y)}{I_x} \Omega^2. \tag{2.2}$$

For certain shapes such as the thin rigid blade, $I_z - I_y = I_x$. Assuming θ is small and $\sin 2\theta \approx 2\theta$, the equation becomes

$$\ddot{\theta} + \Omega^2 \theta = 0. \tag{2.3}$$

From the result, the natural pitch frequency of the rigid blade for small values of θ is Ω, the rotational frequency. For larger displacements, numerical analysis indicates the natural frequency of blade pitch decreases as θ increases, with the ratio of pitch frequency

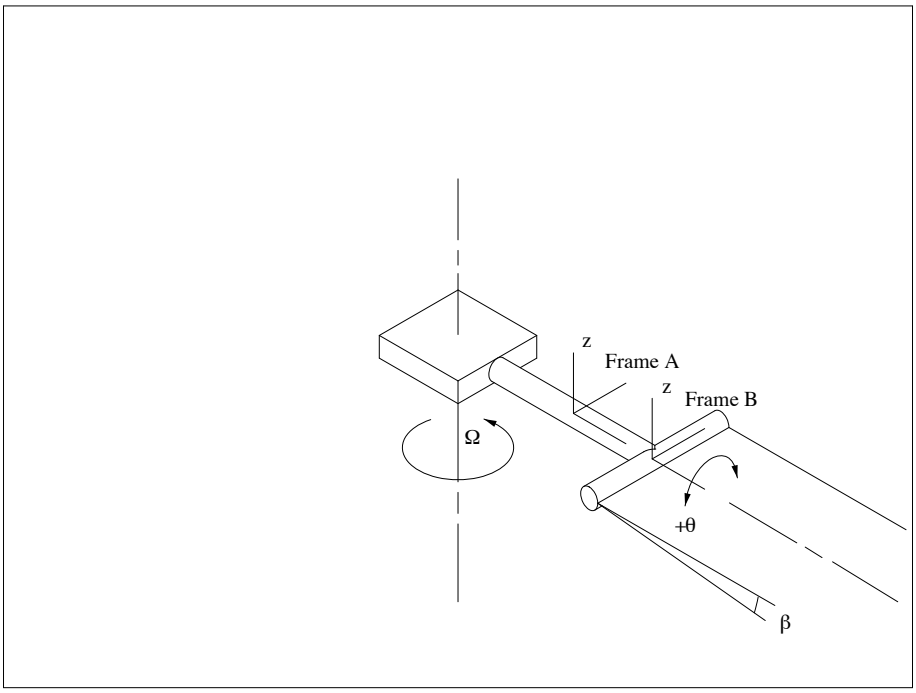


Figure 2.1: Rigid blade rotating about a longitudinal axis.

to rotational frequency about 0.85 for an initial pitch of 45 degrees. A plot of pitch angle vs. rotational angle for initial displacements ranging from 10 to 45deg is depicted in Figure 2.2.

A stiff blade pitches uniformly and tends to match the rotation frequency, as desired for heliogyro control. In reality, the blade is a membrane with centripetal force its main stiffening agent. Control requires taking into account coupling between axial deformation, vertical and in-plane deflection and twist. Blade coning must be limited. Damping must be incorporated to maintain controlled motion. Curling effects must be ameliorated. These efforts begin with proper numerical models.

Within this chapter, the original analytical model for blade behavior is derived. A discretized blade model based on continuum mechanics and a model using Kane's equations and an assumed modes approach follow. The numerical models, taken together, provide a solid basis for analyzing blade behavior, incorporating controls and simulating the results.

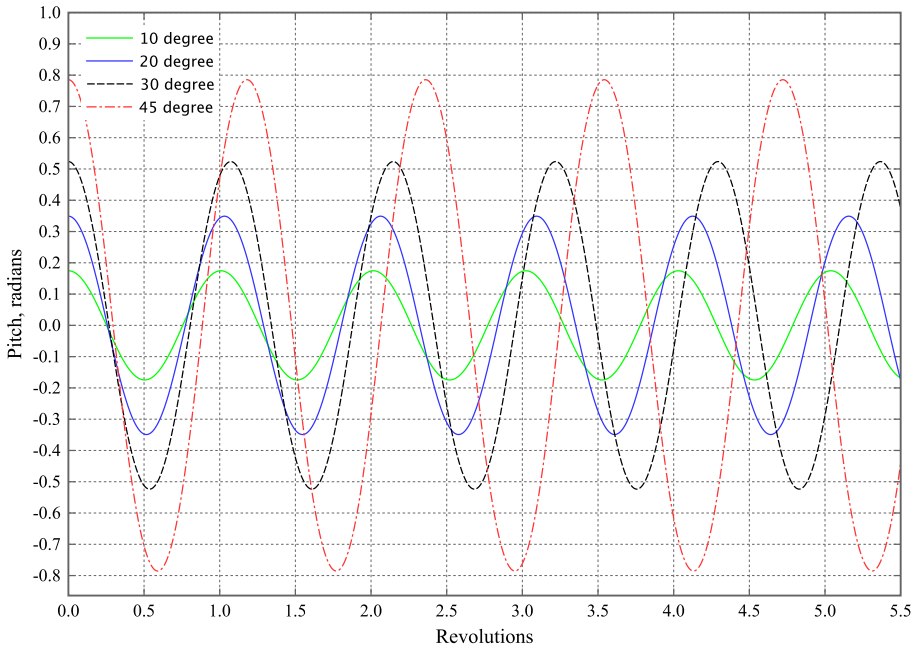


Figure 2.2: Pitch response for varying initial stiff blade pitch angles.

2.1 MacNeal's Equations

The uncoupled equations originally used to describe the behavior of the heliogyro blades are derived as follows. Consider a heliogyro blade modeled as a string with density $\rho(x)$, as shown in Figure 2.3. One end of the string is attached to a vertical axis rotating at a constant angular velocity; the other end is unsupported. Thickness, h, and chord, c, are small compared to the length; rotatory inertia and shear effects are therefore negligible. The string is axially loaded by centripetal force, $\sigma(x)ch$, and laterally by solar pressure, $P_n(x,t)$. Centripetal stiffness is sufficient to keep transverse deflections small.

Following the blade discretization illustrated in Figure 2.3, the equation for transverse motion, w, is

$$\left[\sigma(x) + \frac{\partial\sigma(x)}{\partial(x)}dx\right]\left[\frac{\partial w(x,t)}{\partial x} + \frac{\partial^2 w(x,t)}{\partial x^2}\right]ch - \sigma(x)ch\,\frac{\partial w(x,t)}{\partial x} + P_n(x,t)c\,dx = \rho(x)ch\,\frac{\partial^2 w(x,t)}{\partial t^2}\,dx \tag{2.4}$$

Ignoring second order terms in dx gives

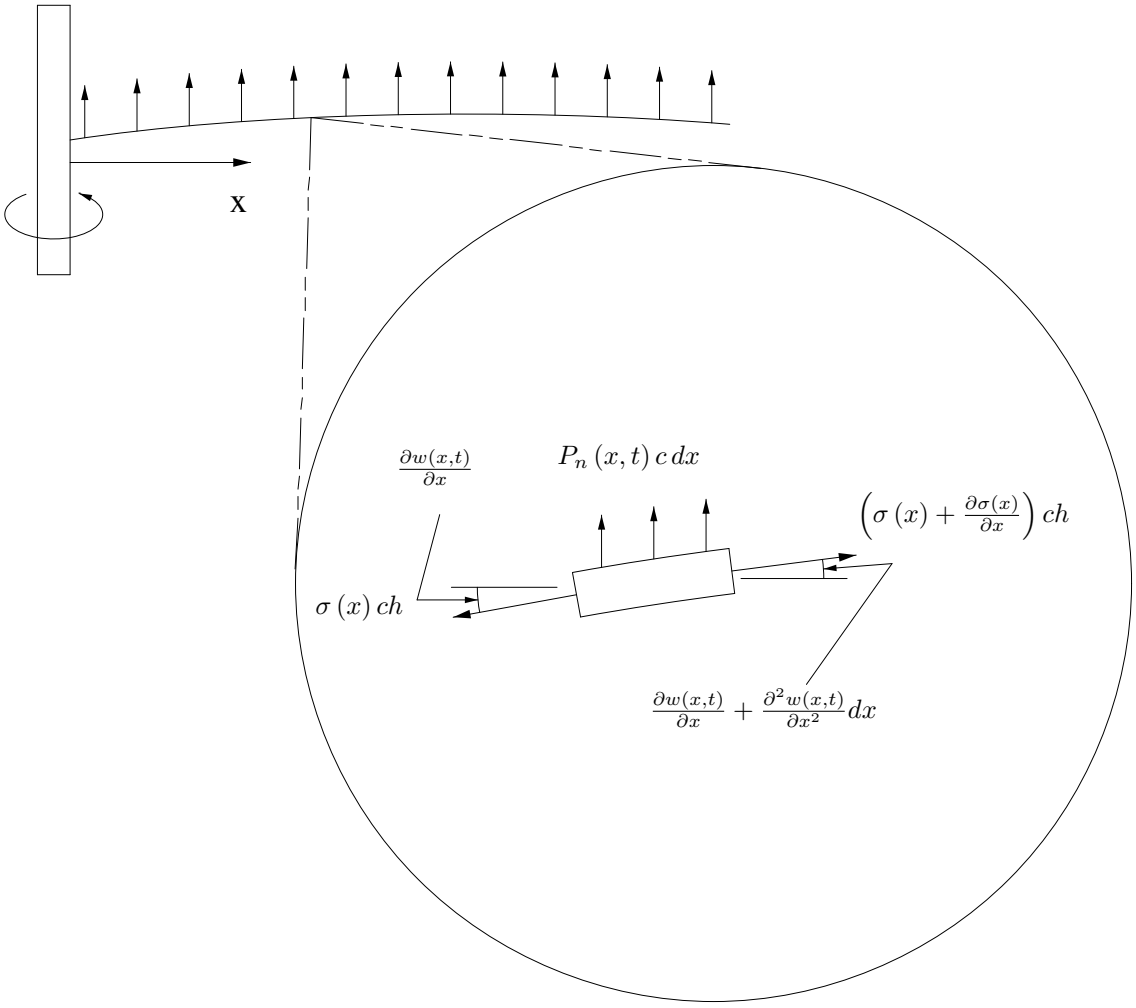


Figure 2.3: Free-body diagram of a differential element under centripetal stress

$$\frac{\partial \sigma(x)}{\partial x}\frac{\partial w(x,t)}{\partial x} ch\, dx + \sigma(x)\frac{\partial^2 w(x,t)}{\partial x^2} ch\, dx + P_n(x,t) c\, dx = \rho(x) ch \frac{\partial^2 w(x,t)}{\partial t^2}\, dx \tag{2.5}$$

Dividing by $ch\, dx$ and writing compactly results in the uncoupled equation for vertical deflection:

$$\frac{\partial}{\partial x}\left[\sigma(x)\frac{\partial w(x,t)}{\partial x}\right] + \frac{P_n(x,t)}{h} = \rho(x)\frac{\partial^2 w(x,t)}{\partial t^2} \tag{2.6}$$

vertical deflection

To derive the equations for in-plane transverse deflection and twist, the blade is considered a tensioned membrane, with centripetal stress in both the longitudinal and transverse directions. Equation 2.6 becomes

$$\frac{\partial}{\partial x}\left[\sigma(x)\frac{\partial w(x,t)}{\partial x}\right] + \frac{\partial}{\partial y}\left[\sigma(y)\frac{\partial w(y,t)}{\partial y}\right] + \frac{P_y(x,t)}{h} = \rho(x)\frac{\partial^2 w(x,t)}{\partial t^2} \tag{2.7}$$

Figure 2.4 represents the centripetal force density on a two-dimensional differential element. Integrating along the length of the blade and then along the chord gives the radial and transverse components of centripetal force at that element [21]:

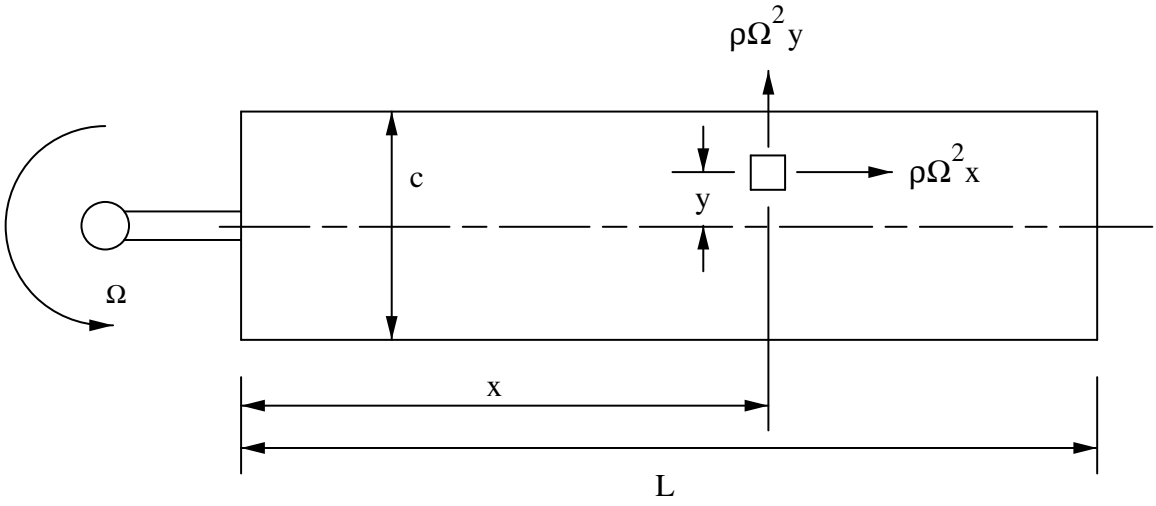


Figure 2.4: Centripetal force on a two dimensional differential element. [21]

$$\sigma(x) = \int_x^L \rho\Omega^2 x\, dx = \frac{1}{2}\rho\Omega^2(L^2 - x^2) \tag{2.8}$$

$$\sigma(y) = \int_y^{\frac{c}{2}} \rho\Omega^2 y\, dy = \frac{1}{2}\rho\Omega^2 \left(\left(\frac{c}{2}\right)^2 - y^2 \right) \tag{2.9}$$

The equation for in-plane transverse deflection now arises from the following steps: replacing w with u in equation 2.7 to represent in-plane transverse deflection; calculating the second term of equation 2.7 using the stress relation in equation 2.9; multiplying the total equation by ch; and inserting a bending stiffness term. The result is

$$-\frac{\partial^2}{\partial x^2}\left[EI\frac{\partial^2 u}{\partial x^2}\right] + \frac{\partial}{\partial x}\left[ch\sigma(x)\frac{\partial u}{\partial x}\right] - \rho ch\Omega^2 u + P_y c = \rho(x)ch\frac{\partial^2 u}{\partial t^2} \quad \textbf{in-plane deflection} \tag{2.10}$$

An important difference between Equation 2.10 and the original equation [21],[22] is the sign of the third term. If the sign for this term is changed to match the original, an improper negative restoring force is present, and the beam destabilizes as the spin rate increases. A more accurate derivation is accomplished when linearization is held until the correct point to avoid improper spin softening. The sign used in the original documents appears in the remainder of this section, to reflect the analysis of the time.

To obtain the uncoupled twist equation, w is set equal to θy in equation 2.7, indicating that vertical deflection is purely due to twist. This gives

$$\frac{\partial}{\partial x}\left[\sigma(x)y\frac{\partial \theta}{\partial x}\right] - \rho(x)\Omega^2 y\theta + \frac{P_n(x,t)}{h} = \rho(x)\frac{\partial^2(\theta y)}{\partial t^2} \tag{2.11}$$

The final form of the equation comes after multiplying equation 2.11 through by yt and integrating over the chord:

$$\frac{\partial}{\partial x}\left[\sigma(x)\frac{\partial \theta}{\partial x}\int_{-\frac{c}{2}}^{\frac{c}{2}} y^2 h\, dy\right] - \rho x\Omega^2\theta\int_{-\frac{c}{2}}^{\frac{c}{2}} y^2 h\, dy + \int_{-\frac{c}{2}}^{\frac{c}{2}} P_n y\, dy = \rho(x)\frac{\partial^2\theta}{\partial t^2}\int_{-\frac{c}{2}}^{\frac{c}{2}} y^2 h\, dy \tag{2.12}$$

or

$$\frac{\partial}{\partial x}\left[I\sigma(x)\frac{\partial\theta}{\partial x}\right] - \rho\Omega^2 I\theta + M_\theta = \rho(x)I\frac{\partial^2\theta}{\partial t^2} \qquad \boxed{\textbf{twist}} \tag{2.13}$$

In Equation 2.13, I is the area moment of inertia with respect to a vertical axis and M_θ is the applied moment with respect to the mid-chord line.

Together, Equations 2.6, 2.10, and 2.13 constitute the uncoupled equations of motion for a heliogyro blade. These give rise to fundamental expressions for heliogyro behavior. Among other things, Equation 2.13 provides steady-state blade twist, torque required to pitch a blade, and natural twist frequencies; Equation 2.6 describes blade coning angle, vertical deflection, and vertical deflection natural frequencies; and Equation 2.10 gives in-plane natural frequencies. The following paragraphs present equations for these behaviors.

2.1.1 Twist Behaviors

To solve Equation 2.13 for the twist along the length of the blade when the root is pitched at the constant angle θ, equation 2.8 is first substituted into equation 2.13 and the result is expanded:

$$I\frac{\partial\theta}{\partial x}\left(-\rho\Omega^2 x\right) + I\left(\frac{1}{2}\rho\Omega^2\left(L^2 - x^2\right)\right)\frac{\partial^2\theta}{\partial x^2} - \rho\Omega^2 I\theta + M_\theta = \rho I\frac{\partial^2\theta}{\partial t^2} \tag{2.14}$$

If M_θ, the applied moment, is 0, then by cancelling $I\rho\Omega^2$ throughout and rearranging terms, equation 2.14 becomes

$$\frac{1}{2}\left(L^2 - x^2\right)\frac{\partial^2\theta}{\partial x^2} - x\frac{\partial\theta}{\partial x} - \theta = \frac{1}{\Omega^2}\frac{\partial^2\theta}{\partial t^2} \tag{2.15}$$

Nondimensionalizing equation 2.15 aids in the solution process. If $\alpha = x/L$, $\tau = \Omega t$, and θ is assumed to be in the form of $e^{i\bar{\omega}\tau}$, equation 2.15 can be written

$$\frac{1}{2}\frac{\partial}{\partial\alpha}\left(\left(1-\alpha^2\right)\frac{\partial\theta}{\partial\alpha}\right) + \left(\bar{\omega}^2 - 1\right)\theta = 0 \tag{2.16}$$

with $\bar{\omega}$ representing the dimensionless angular velocity $\dot{\theta}/\Omega$.

For the steady-state case, $\theta = f(x)$, and 2.16 becomes the homogeneous differential equation

$$\frac{1}{2}\left(1-\alpha^2\right)\frac{d^2\theta}{d\alpha^2}-\alpha\frac{d\theta}{d\alpha}-\theta=0 \tag{2.17}$$

which is an equivalent form of the Legendre equation [22].

A power series about the point $\alpha = 0$ provides the basis for an analytical solution. With the series $\theta = A_0 + A_1\alpha + A_2\alpha^2 + A_3\alpha^3 + \ldots$ and its first and second derivatives substituted into equation 2.17, coefficients of terms of the same power are set equal to 0. The solution leads to the recurrence formula for the coefficients $A_2, A_3, A_4, \ldots$:

$$A_{i+2} = \frac{i\,(i-1)+2i+2}{(i+2)\,(i+1)}A_i \tag{2.18}$$

The twist equation is then

$$\begin{aligned}\theta =& A_0\left(1+\alpha^2+\frac{2}{3}\alpha^4+\frac{11}{15}\alpha^6+\frac{11}{14}\alpha^8+\frac{37}{45}\alpha^{10}+\ldots\right)+\\ & A_1\left(\alpha+\frac{2}{3}\alpha^3+\frac{7}{10}\alpha^5+\frac{16}{21}\alpha^7+\frac{29}{36}\alpha^9+\frac{46}{55}\alpha^{11}+\ldots\right)\end{aligned} \tag{2.19}$$

The coefficients A_0 and A_1 come from the initial conditions $\theta|_{x=0} = \theta_0$ and $\frac{d\theta}{d\alpha}|_{x=L} = 0$. Including the first 3000 terms of equation 2.19 and its derivative and setting them equal to their initial conditions results in $A_0 = \theta_0$ and $A_1 \approx -1.21\theta_0$. Dividing by θ_0, the nondimensional steady-state twist equation becomes

$$\begin{aligned}\frac{\theta}{\theta_0} =& \left(1+\alpha^2+\frac{2}{3}\alpha^4+\frac{11}{15}\alpha^6+\frac{11}{14}\alpha^8+\frac{37}{45}\alpha^{10}+\ldots\right)-\\ & 1.21\left(\alpha+\frac{2}{3}\alpha^3+\frac{7}{10}\alpha^5+\frac{16}{21}\alpha^7+\frac{29}{36}\alpha^9+\frac{46}{55}\alpha^{11}+\ldots\right)\end{aligned} \tag{2.20}$$

A plot of the nondimensional, steady-state twist curve appears in Figure 2.5.

From the twist curve, Equation 2.20, comes the torque required to pitch a blade. The expression for torque at the blade root is

$$T_0 = I\sigma_0 \cdot \left.\frac{\partial\theta}{\partial x}\right|_{x=0} \tag{2.21}$$

where $I\sigma_0$, the product of the cross-sectional moment of inertia and the blade root stress, is included instead of JG, the product of polar inertia and shear modulus. Equation 2.20 gives the derivative of twist at the root as

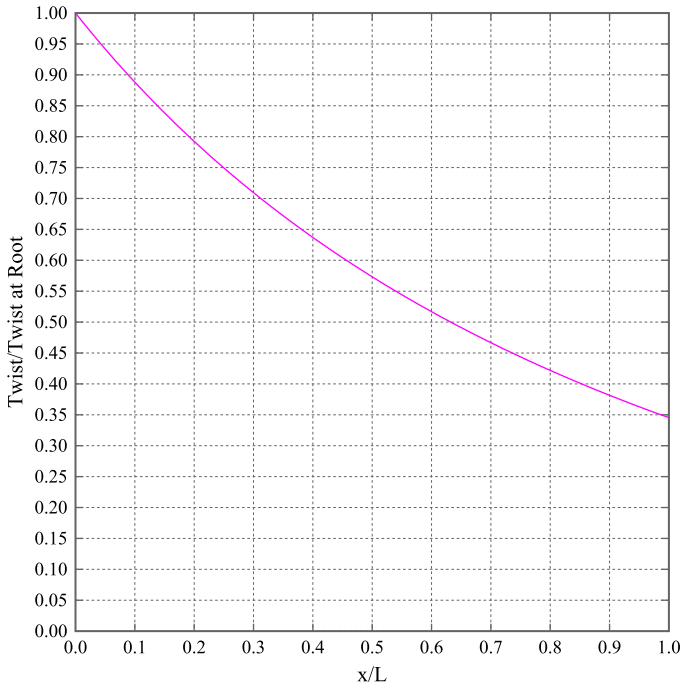


Figure 2.5: Nondimensional, steady-state twist curve.

$$\left.\frac{\partial\theta}{\partial x}\right|_{x=0} = 1.21\frac{\theta_0}{L} \tag{2.22}$$

which makes Equation 2.21

$$T_0 = 1.21 I\sigma_0 \cdot \frac{\theta_0}{L} \tag{2.23}$$

Comparing Equation 2.16 to the typical form of Legendre's equation,

$$\frac{d}{dy}\left(\left(1-y^2\right)\frac{dx}{dy}\right) + n\left(n+1\right)x = 0 \tag{2.24}$$

the twist natural frequency is

$$\bar{\omega} = \sqrt{\frac{n\left(n+1\right)}{2}+1} \tag{2.25}$$

where 0 and the odd values of n take the role of eigenvalues [22]. The first twist natural frequency predicts that the blade will naturally pitch at the rate of rotation. The next twist natural frequency is 1.4 times the spin rate.

At pitch rates other than once per rotation, the blade tip twist amplitude is found by numerically integrating Equation 2.16 [22] or by the power series method described above. Using the power series method, the recurrence formula similar to Equation 2.18 for the case when $\bar{\omega} \neq 0$ is

$$A_{i+2} = \left[\frac{i\,(i-1) + 2i + 2}{(i+2)\,(i+1)} - \bar{\omega}^2 \frac{1}{\sum_0^i (i+1)} \right] A_i \tag{2.26}$$

The relationship between $\theta_{tip_{max}}/\theta_{root_{max}}$ and relative pitch rate via Equation 2.26 is illustrated in Figure 2.6.

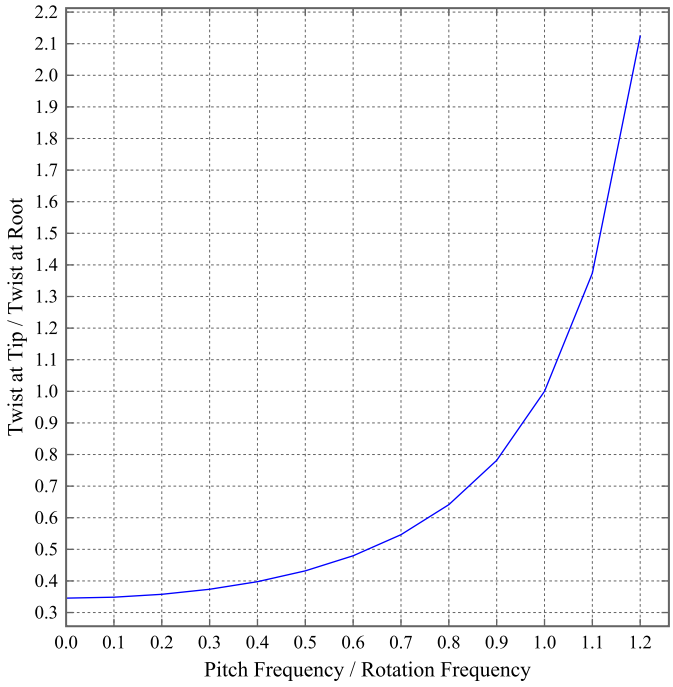


Figure 2.6: Twist vs. Relative Pitch Frequency.

2.1.2 Vertical Deflection Behaviors

Coning angle, β, is equal to $\partial w/\partial x$. Assuming static blade deflection and zero collective pitch, integration of Equation 2.6 gives the expression for local coning angle:

$$\beta = \frac{\partial w}{\partial x} = \frac{1}{\sigma_x} \int_x^L \frac{P_n}{h} \cdot dx = \frac{2P_n}{h\rho\Omega^2\,(R+r)} \tag{2.27}$$

with P_n equal to the solar radiation pressure minus the inertial reaction of the spacecraft, or

$$P_n = \frac{\text{non-sail mass}}{\text{total mass}} \times P_0 \tag{2.28}$$

Equation 2.27 shows that the tip coning angle is half the root coning angle. Integrating once again generates an expression for vertical deflection:

$$w = \frac{2P_n}{h\rho\Omega^2} \ln\left(1 + \frac{r}{R}\right) \tag{2.29}$$

To limit precession due to coning, coupling between in-plane deflection and twist, and loss of thrust, the heliogyro spins at a rate that limits the root coning angle to around $1\,^\circ$. In this case, the coning angle can be assumed to be almost constant. If the coning angle is assumed constant along the blade, the resultant straight blade deflection is instead

$$w = \beta_c x \tag{2.30}$$

where β_c is the constant coning angle. Two choices for β_c are readily available. The first is β_0, the coning angle at the root. The second is β_m, the mean coning angle, defined by the value, when multiplied by the length of the blade, that equals the tip deflection given by Equation 2.29. Hence,

$$\beta_m = \beta_0 \ln(2) \tag{2.31}$$

Figure 2.7 compares vertical deflection given by Equations 2.29 and 2.30. The two straight lines correspond to using the root coning angle and the mean coning angle as the constant coning angle. The curved line correspond to the values calculated via Equation 2.29. All values are nondimensionalized, with the deflection values divided by $\beta_0 L$.

The maximum deviation of deflection obtained using the mean coning angle from that obtained from Equation 2.29 occurs at 44.27% of the blade span. At that point, the actual coning angle equals the mean coning angle. The max deviation is given by

$$\delta = 0.0597\beta_0 L \tag{2.32}$$

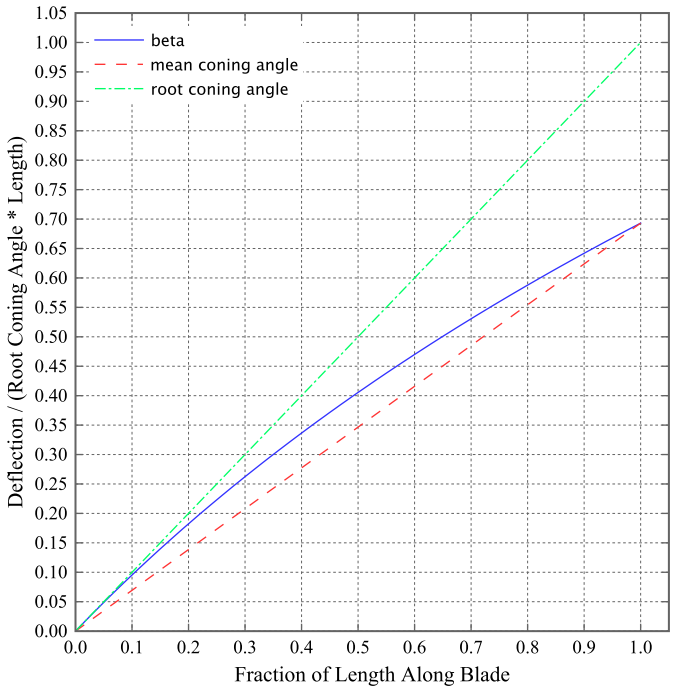


Figure 2.7: Nondimensional vertical deflection curves.

which is 16.3% of the value obtained at $x = .4427\,L$ by Equation 2.29. If the root coning angle is around $1\,^\circ$, the max deviation is 0.1% of L.

The homogeneous, nondimensional equivalent of Equation 2.6, the vertical deflection equation, derives the same way as the twist case. With $\alpha = x/L$, $\tau = \Omega t$, and motion assumed to be in the form of $e^{i\bar{\omega}\tau}$, the nondimensional equation for vertical deflection is

$$\frac{1}{2}\frac{\partial}{\partial\alpha}\left(\left(1-\alpha^2\right)\frac{\partial\bar{w}}{\partial\alpha}\right) + \bar{\omega}^2\bar{w} = 0 \tag{2.33}$$

Comparing this equation to Equation 2.24, the natural frequency for vertical deflection is

$$\bar{\omega} = \sqrt{\frac{n\,(n+1)}{2}} \tag{2.34}$$

2.1.3 Inplane Deflection Behaviors

The homogeneous nondimensional version of the inplane deflection equation 2.10 is obtained as before. With the sign change incorporated as noted after Equation 2.10, The result is

$$-\frac{1}{2}\frac{\partial^2}{\partial\alpha^2}\left[K\frac{\partial^2\bar{u}}{\partial\alpha^2}\right]+\frac{1}{2}\frac{\partial}{\partial\alpha}\left[\left(1-\alpha^2\right)\frac{\partial\bar{u}}{\partial\alpha}\right]+\left(\bar{\omega}^2+1\right)\bar{u}=0 \tag{2.35}$$

with

$$K=\frac{EI}{\frac{1}{2}\Omega^2 chL^4} \tag{2.36}$$

Typically, K is negligible for heliogyros. Hence, the first term of Equation 2.35 disappears. The resulting natural inplane frequencies are

$$\bar{\omega}=\sqrt{\frac{n\left(n+1\right)}{2}-1} \tag{2.37}$$

2.1.4 Calculated Behavior of a Sample Heliogyro

Table 2.1 lists the first four natural frequencies starting at $n = 1$ for twist, vertical deflection, and in-plane deflection. Table 2.2 lists the characteristics and behaviors of a representative spacecraft with blades 1000 m long, 1 m wide and 3 μ thick, spinning at 2 rpm. The numbers arise from the equations in this section, and are based on the original heliogyro calculations appearing in the literature.

Table 2.1: First four natural frequencies for twist, vertical deflection, and in-plane deflection.

Twist (Eq. 2.22)	Vertical (Eq. 2.30)	In-Plane (Eq. 2.33)
1.414	1.000	0.000
2.646	2.449	2.236
4.000	3.873	3.742
5.385	5.292	5.196

2.2 Stiff Blade Heliogyro

The stiff-blade heliogyro model consists of n_b flat, rigid blades symmetrically spaced around a rigid-body central core. As seen in Figure 2.8, each blade attaches to the core through

Table 2.2: Sample heliogyro.

Spacecraft Characteristic	Value	
S/C non-sail mass, kg	251	
S/C total mass, kg	296	
Ratio, non-sail mass/total mass	0.85	
Heliogyro Period, s	30	
Spin rate, rad/s	0.2094	
Blade Characteristic	**Value**	
Blade length, m	1000	
Blade chord, m	1	
Blade thickness, μ	3	
Blade material density, kg/m^3	1400	
Cross-sectional moment of inertia, m^4	2.25×10^{-18}	
Blade Behavior	**Value**	**Equation Number**
Blade root stress, MPa	30.7	Eq. 2.5
Torque for collective pitch, Nm/rad	8.36×10^{-14}	Eq. 2.20
Twist at tip with root pitched $pi/6$ rad	0.181	Eq. 2.17
Root coning angle, rad	8.28×10^{-05}	Eq. 2.23
Mean coning angle, rad	5.74×10^{-05}	Eq. 2.27
Max vertical deflection, m	0.0574	Eq. 2.25
Max deviation from a straight line, m	0.0049	Eq. 2.28

an arm and a blade pitching mechanism. Blade spacing around the core is given by the rotation angle γ_i, taken counterclockwise about the z axis of Frame Q, from the x axis of Q to the respective arm. Figure 2.8 illustrates the measurement of γ_2, as an example. The mass center of blade i lies at the origin of Frame A_i in the xy plane of Frame Q, a distance *arm* from the core. Each blade root holder pitches independently about the line connecting the origins of Frame Q and Frame A_i, based on a control strategy.

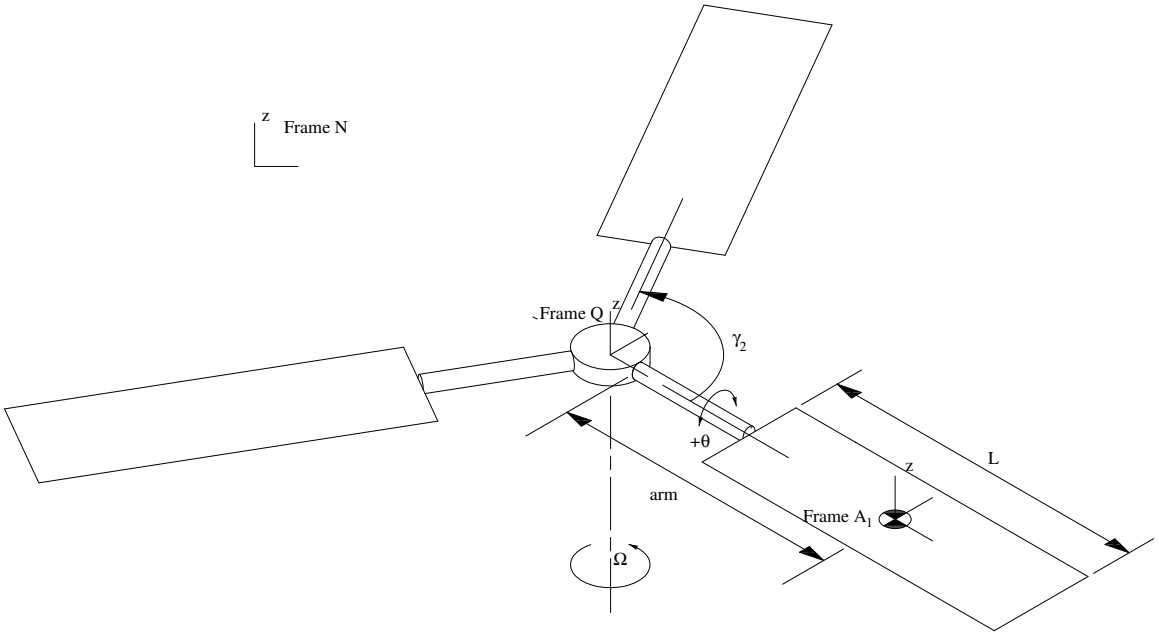


Figure 2.8: Heliogyro with reference frames.

Appropriate generalized coordinates for the governing equations of motion come from the position vector of the core, the core orientation, and the pitch angle of each blade. Coordinates q_1 through q_3 represent the x, y, and z components of the position vector from an inertial reference frame N to the reference frame Q located at the center of the heliogyro core, or

$$\begin{bmatrix} q_1 \\ q_2 \\ q_3 \end{bmatrix} = {}^N\vec{P}_{NQ} \tag{2.38}$$

Coordinates q_4 through q_7 constitute the Euler quaternion $\vec{p}$, which represents the orientation of the core with respect to N. The heliogyro model uses the Euler quaternion to avoid the singularity issues inherent with certain orientation methods such as Euler angles

or roll-pitch-yaw axes. The quaternion is expressed as

$$q_4 = \cos\frac{\theta}{2} \tag{2.39}$$

$$\begin{bmatrix} q_5 \\ q_6 \\ q_7 \end{bmatrix} = \vec{k}\sin\frac{\theta}{2} \tag{2.40}$$

where $\vec{k}$ represents the vector of rotation and θ the angle of rotation from the Q reference frame to the inertial reference frame, N. Of special note is the rotation matrix conversion from the Euler quaternion [16]

$${}^{N}R_{Q} = \begin{bmatrix} 1-2q_6^2-2q_7^2 & 2q_5q_6-2q_4q_7 & 2q_5q_7+2q_4q_6 \\ 2q_5q_6+2q_4q_7 & 1-2q_5^2-2q_7^2 & 2q_6q_7-2q_4q_5 \\ 2q_5q_7-2q_4q_6 & 2q_6q_7+2q_4q_5 & 1-2q_5^2-2q_6^2 \end{bmatrix} \tag{2.41}$$

Pitch angles $\theta_i, i = 1 \ldots n_b$ represent the remaining generalized coordinates $q_8 \ldots q_{8+n_b}$.

The corresponding generalized speeds are

$$\begin{bmatrix} u_{s1} \\ u_{s2} \\ u_{s3} \end{bmatrix} = {}^{Q}\dot{\vec{P}}_{NQ} = {}^{Q}R_{N} \begin{bmatrix} \dot{q}_1 \\ \dot{q}_2 \\ \dot{q}_3 \end{bmatrix} \tag{2.42}$$

$$\begin{bmatrix} u_{s4} \\ u_{s5} \\ u_{s6} \end{bmatrix} = {}^{Q}\omega_{NQ} = 2L\dot{\vec{p}} \tag{2.43}$$

$$u_{s6+i} = \dot{\theta}_i, \quad i = 1, \ldots n_b \tag{2.44}$$

[31] where ${}^{Q}\vec{\omega}_{NQ}$ is the angular velocity of Q with respect to N, θ_i is the pitch angle of blade i, and

$$L = \begin{bmatrix} -q_5 & q_4 & q_7 & -q_6 \\ -q_6 & -q_7 & q_4 & q_5 \\ -q_7 & q_6 & -q_5 & q_4 \end{bmatrix} \tag{2.45}$$

The quantity LL^T equals the 3×3 identity matrix, and $\vec{p}^T\vec{p} - 1 = 0$. Hence, the time derivative of the Euler quaternion can be given as

$$\dot{p} = \frac{1}{2}L^T \cdot {}^{Q}\vec{\omega}_{NQ} \tag{2.46}$$

The rotation matrix ${}^{Q}R_{A_i}$, defining the orientation of each blade with respect to the core, is a composite rotation of γ_i and θ_i:

$$
{}^{Q}R_{A_i} = R_z(\gamma_i)R_x(\theta_i) = \begin{bmatrix} \cos(\gamma_i) & -\sin(\gamma_i) & 0 \\ \sin(\gamma_i) & \cos(\gamma_i) & 0 \\ 0 & 0 & 1 \end{bmatrix} \begin{bmatrix} 1 & 0 & 0 \\ 0 & \cos(\theta_i) & -\sin(\theta_i) \\ 0 & \sin(\theta_i) & \cos(\theta_i) \end{bmatrix} \tag{2.47}
$$

$$
= \begin{bmatrix} \cos(\gamma_i) & -\sin(\gamma_i)\cos(\theta_i) & \sin(\gamma_i)\sin(\theta_i) \\ \sin(\gamma_i) & \cos(\gamma_i)\cos(\theta_i) & -\cos(\gamma_i)\sin(\theta_i) \\ 0 & \sin(\theta_i) & \cos(\theta_i) \end{bmatrix} \tag{2.48}
$$

Kane's equations call for the determination of generalized inertia forces (F_u^*) for each body and generalized active forces (F_u) for every active force location. Dynamic equations arise from setting the sum $F_u^* + F_u$ equal to zero. The expressions for F_u^* and F_u are given below.

$$
\begin{aligned} F_{u_i}^* = {} & \frac{\partial}{\partial u_i}\left({}^{Q}\dot{\vec{P}}_{NQ}\right) \cdot {}^{Q}F_{in_Q} + \frac{\partial}{\partial u_i}\left({}^{Q}\vec{\omega}_{NQ}\right) \cdot {}^{Q}T_{in_Q} + \frac{\partial}{\partial u_i}\left({}^{A_i}\dot{\vec{P}}_{NA_i}\right) \cdot {}^{A_i}F_{in_{A_i}} \\ & + \frac{\partial}{\partial u_i}\left({}^{A_i}\vec{\omega}_{NA_i}\right) \cdot {}^{A_i}T_{in_{A_i}} \end{aligned} \tag{2.49}
$$

$$
\begin{aligned} F_{u_i} = {} & \frac{\partial}{\partial u_i}\left({}^{Q}\dot{\vec{P}}_{NQ}\right) \cdot {}^{Q}\vec{G}_{Core} + \frac{\partial}{\partial u_i}\left({}^{A_i}\vec{\omega}_{QA_i}\right) \cdot {}^{A_i}\vec{T}_{QA_i} \\ & + \frac{\partial}{\partial u_i}\left({}^{A_i}\dot{\vec{P}}_{NA_i}\right) \cdot \left(-{}^{A_i}\vec{F}_{A_iBlade} + {}^{A_i}\vec{G}_{A_i}\right) \end{aligned} \tag{2.50}
$$

Inertial forces and torques for the rigid body core and blades in Equation 2.49 are:

$$
{}^{Q}\vec{F}_{in_Q} = -m_Q \cdot {}^{Q}\ddot{\vec{P}}_{NQ} \tag{2.51}
$$

$$
{}^{Q}\vec{T}_{in_Q} = -{}^{Q}\vec{\alpha}_{NQ} \cdot \underline{\mathbf{I}}_Q - {}^{Q}\vec{\omega}_{NQ} \times \left(\underline{\mathbf{I}}_Q \cdot {}^{Q}\vec{\omega}_{NQ}\right) \tag{2.52}
$$

$$
{}^{A_i}\vec{F}_{NA_i} = -m_{A_i} \cdot {}^{A_i}\ddot{\vec{P}}_{NA_i} \tag{2.53}
$$

$$
{}^{A_i}\vec{T}_{NA_i} = -{}^{A_i}\vec{\alpha}_{NA_i} \cdot \underline{\mathbf{I}}_i - {}^{A_i}\vec{\omega}_{NA_i} \times \left(\underline{\mathbf{I}}_i \cdot {}^{A_i}\vec{\omega}_{NA_i}\right) \tag{2.54}
$$

In Equations 2.51 through 2.54, m_Q and m_{A_i} are the mass of the core and blade i, respectively, while $\underline{\mathbf{I}}_Q$ and $\cdot\underline{\mathbf{I}}_i$ are inertia matrices for the core and blade i.

The derivation requires the determination of the velocities, accelerations, angular velocities, and angular accelerations of each body and active force location, as well as the applied

forces and torques on the blades. For the core, Equations 2.42 and 2.43 give the velocities; their derivatives are

$$^{Q}\ddot{\vec{P}}_{NQ} = \begin{bmatrix} \dot{u}_{s1} \\ \dot{u}_{s2} \\ \dot{u}_{s3} \end{bmatrix} \tag{2.55}$$

$$^{Q}\vec{\alpha}_{NQ} = \begin{bmatrix} \dot{u}_{s4} \\ \dot{u}_{s5} \\ \dot{u}_{s6} \end{bmatrix} \tag{2.56}$$

For each blade root holder, the velocities $^{A_i}\vec{\omega}_{NA_i}$ and $^{A_i}\dot{\vec{P}}_{NA_i}$ are

$$^{A_i}\vec{\omega}_{NA_i} = {}^{A_i}R_Q\,{}^{Q}\vec{\omega}_{NQ} + \begin{bmatrix} \dot{\theta}_i \\ 0 \\ 0 \end{bmatrix} \tag{2.57}$$

$$^{A_i}\dot{\vec{P}}_{NA_i} = {}^{A_i}R_Q\,{}^{Q}\dot{\vec{P}}_{NQ} + {}^{A_i}\vec{\omega}_{NA_i} \times {}^{A_i}\vec{P}_{QA_i} \tag{2.58}$$

where

$$^{A_i}\vec{P}_{QA_i} = \begin{bmatrix} arm_i \\ 0 \\ 0 \end{bmatrix} \tag{2.59}$$

Taking the derivative of the core and blade root holder velocities gives

$$\begin{aligned} ^{A_i}\ddot{\vec{P}}_{NA_i} = {}& {}^{A_i}\ddot{\vec{P}}_{NQ} + {}^{A_i}\vec{\alpha}_{NQ} \times {}^{A_i}\vec{P}_{QA_i} + {}^{A_i}\vec{\omega}_{NQ} \times \left({}^{A_i}\vec{\omega}_{NQ} \times {}^{A_i}\vec{P}_{QA_i} \right) \\ & + {}^{A_i}\vec{\alpha}_{QA_i} \times {}^{A_i}\vec{P}_{QA_i} + 2\,{}^{A_i}\vec{\omega}_{NQ} \times \left({}^{A_i}\vec{\omega}_{QA_i} \times {}^{A_i}\vec{P}_{QA_i} \right) \\ & + {}^{A_i}\vec{\omega}_{QA_i} \times \left({}^{A_i}\vec{\omega}_{QA_i} \times {}^{A_i}\vec{P}_{QA_i} \right) \end{aligned} \tag{2.60}$$

$$^{A_i}\vec{\alpha}_{NA_i} = {}^{A_i}\vec{\omega}_{A_iQ} \times {}^{A_i}R_Q\,{}^{Q}\vec{\omega}_{NQ} + {}^{A_i}R_Q\,{}^{Q}\vec{\alpha}_{NQ} + \begin{bmatrix} \ddot{\theta}_i \\ 0 \\ 0 \end{bmatrix} \tag{2.61}$$

With the velocities determined, the partial velocities can be found. Table 2.3 lists the partial velocities with respect to the generalized speeds. In the table, the entries are 3×3 matrices. The first row of each entry is the transpose of the partial derivative of the velocity vector listed in its column heading with respect to the first generalized speed listed in the

row heading. The second and third rows follow the pattern. The symbol [0] is the $3x3$ matrix consisting of 0 entries and I is the $3x3$ identity matrix. As a shorthand, $s\gamma_i$, $s\theta_i$, $c\gamma_i$ and $c\theta_i$ represent $\sin\gamma_i$, $\sin\theta_i$, $\cos\gamma_i$ and $\cos\theta_i$.

Table 2.3: Partial velocities for the stiff-blade model.

	$\frac{\partial}{\partial u_i}\left({}^{Q}\dot{\vec{P}}_{NQ}\right)$	$\frac{\partial}{\partial u_i}\left({}^{Q}\vec{\omega}_{NQ}\right)$	$\frac{\partial}{\partial u_i}\left({}^{A_i}\dot{\vec{P}}_{NA_i}\right)$	$\frac{\partial}{\partial u_i}\left({}^{A_i}\vec{\omega}_{NA_i}\right)$
u_{s1}				
u_{s2}	I	[0]	${}^{Q}R_{A_i}$	[0]
u_{s3}				
u_{s4}			$arm \cdot \begin{bmatrix} 0 & s\gamma_i\, s\theta_i & c\,\theta_i s\,\gamma_i \\ 0 & -c\,\gamma_i s\,\theta_i & c\,\gamma_i c\,\theta_i \\ 0 & c\,\theta_i & -s\,\theta_i \end{bmatrix}$	
u_{s5}	[0]	I		${}^{Q}R_{A_i}$
u_{s6}				
u_{s6+i}	$\begin{bmatrix} 0 & 0 & 0 \end{bmatrix}$	$\begin{bmatrix} 0 & 0 & 0 \end{bmatrix}$	$\begin{bmatrix} 0 & 0 & 0 \end{bmatrix}$	$\begin{bmatrix} 1 & 0 & 0 \end{bmatrix}$

For the full-up simulation, the heliogyro will move in a 4-body system: the Sun, the Earth, the moon, and the heliogyro. Gravitational forces for the core and blade root holder in this case are:

(2.62)
$${}^{Q}\vec{G}_{core} = \frac{Gm_{Sun}m_Q{}^{Q}\vec{P}_{SunQ}}{\|{}^{Q}\vec{P}_{SunQ}\|^3} + \frac{Gm_{Earth}m_Q{}^{Q}\vec{P}_{EarthQ}}{\|{}^{Q}\vec{P}_{EarthQ}\|^3} + \frac{Gm_{moon}m_Q{}^{Q}\vec{P}_{moonQ}}{\|{}^{Q}\vec{P}_{moonQ}\|^3}$$

(2.63)
$${}^{A_i}\vec{G}_{A_i} = \frac{Gm_{Sun}m_{A_i}{}^{Q}\vec{P}_{SunA_i}}{\|{}^{Q}\vec{P}_{SunA_i}\|^3} + \frac{Gm_{Earth}m_{A_i}{}^{Q}\vec{P}_{EarthA_i}}{\|{}^{Q}\vec{P}_{EarthA_i}\|^3} + \frac{Gm_{moon}m_{A_i}{}^{Q}\vec{P}_{moonA_i}}{\|{}^{Q}\vec{P}_{moonA_i}\|^3}$$

Solar forces on a blade are written

(2.64)
$$\vec{F}_{Sun} = \vec{F}_R + \vec{F}_A = 2\frac{SA}{c}\left(\frac{r_0}{r_s}\right)^2 f_r\cos^2\theta\vec{N} + \frac{SA}{c}\left(\frac{r_0}{r_s}\right)^2(1-f_r)\cos\theta\vec{Sun}$$

where

$F_R =$ force due to photon reflection

$F_A =$ force due to photon absorption

$S =$ Solar flux , $\approx 1367\ W/m^2$ at 1 AU

$r_0 =$ distance from the Earth to the center of the Sun

$r_s =$ distance from the heliogyro to the center of the Sun

$f_r =$ coefficient of reflectivity

$\theta =$ angle between the Sun vector and the blade surface normal

$\vec{N} =$ blade surface normal

$\vec{Sun} =$ Sun vector

$A =$ blade surface area

$c =$ speed of light.

Combining and rearranging Equations 2.42, 2.43, and 2.49 through 2.61, along with the entries in Table 2.3, results in the heliogyro stiff blade equations:

$$\vec{0} = {}^{Q}\vec{G}_{core} + {}^{Q}R_{A_i}\left(-{}^{A_i}\vec{F}_{blade} + {}^{A_i}\vec{G}_{A_i}\right) - m_{core}\cdot\begin{bmatrix}\dot{u}_{s1}\\ \dot{u}_{s2}\\ \dot{u}_{s3}\end{bmatrix} - \sum_{i=1}^{n_b} m_{blade}\,{}^{Q}R_{A_i}\,{}^{A_i}\ddot{\vec{P}}_{NA_i} \tag{2.65}$$

(2.66)

$$\begin{aligned}{}^{Q}\vec{\alpha}_{NQ} = {} & \left[\underline{\mathbf{I}}_Q + {}^{Q}R_{A_i}\underline{\mathbf{I}}_i\,{}^{A_i}R_Q\right]^{-1}\left(-{}^{Q}\vec{\omega}_{NQ}\times\left({}^{Q}\vec{\omega}_{NQ}\cdot\underline{\mathbf{I}}_Q\right)\right.\\ & -{}^{Q}R_{A_i}\underline{\mathbf{I}}_i\left({}^{A_i}\vec{\omega}_{A_iQ}\times{}^{A_i}R_Q\,{}^{Q}\vec{\omega}_{NQ} + {}^{A_i}\vec{\alpha}_{QA_i}\right)\Big) - {}^{Q}R_{A_i}\left({}^{A_i}\vec{\omega}_{NA_i}\times\left({}^{A_i}\vec{\omega}_{NA_i}\cdot\underline{\mathbf{I}}_i\right)\right)\\ & + {}^{Q}\vec{P}_{QA_i}\times\left({}^{Q}\vec{F}_{SunA_i} + {}^{Q}\vec{G}_{A_i} - m_{blade}\,{}^{A_i}\ddot{\vec{P}}_{NA_i}\right)\end{aligned}$$

$$\vec{0} = -{}^{A_i}\vec{\alpha}_{NA_i}\underline{\mathbf{I}}_{i_x} + {}^{A_i}\vec{\omega}_{NA_iy}\,{}^{A_i}\vec{\omega}_{NA_iz}\left(\underline{\mathbf{I}}_{i_y} - \underline{\mathbf{I}}_{i_z}\right) + {}^{A_i}\vec{T}_{QA_ix} \tag{2.67}$$

2.3 Particle Blade

The 1-D equation for wave propagation along a straight string is

$$k\nabla^2 x = \rho\frac{\partial^2 x}{\partial t^2} \tag{2.68}$$

where k is the longitudinal stiffness, x the distance along the string, and ρ the mass density. Finite discretization of this equation results in a series of masses connected by massless springs, and a set of differential equations numerically solvable for x. For surfaces and volumes, the governing equation is much the same. The equation for 2-D and 3-D cases is [8]

$$\rho \frac{\partial^2 \vec{x}}{\partial t^2} - \vec{\nabla} \cdot \sigma = f \tag{2.69}$$

where f is a body force term. The surface interpretation of Equation 2.69 represents the physical behavior of a heliogyro blade. Modeling solar sail material using the discretized equation entails creating a uniform Cartesian mesh of nodes, with a mass lumped at each node. The body and internodal forces act at the nodes. The system converges to the continuum model as the mesh spacing approaches zero.

Discretizing Equation 2.69 for numerical analysis begins with Green's nonlinear strain tensor:

$$G_{ij} = \frac{1}{2}\left(\delta_{\alpha\beta} \frac{\partial s_\alpha}{\partial a_i} \frac{\partial s_\beta}{\partial a_j} - \delta_{ij}\right) \tag{2.70}$$

which is written using double index notation. In the equation above, δ is the Kronecker delta, $s = (s_1, s_2, s_3)$ is a point in the deformed state, and $a = (a_1, a_2, a_3)$ is a point in the undeformed state. For the case of a 2-D manifold or surface, where u and v are the 1st and 2nd material coordinate directions of the undeformed state, Green's strain tensor is written in matrix form as

$$G = \frac{1}{2}\begin{bmatrix} \left(\frac{\partial s}{\partial u} \cdot \frac{\partial s}{\partial u}\right) - 1 & \frac{\partial s}{\partial u} \cdot \frac{\partial s}{\partial v} \\ \frac{\partial s}{\partial u} \cdot \frac{\partial s}{\partial v} & \left(\frac{\partial s}{\partial v} \cdot \frac{\partial s}{\partial v}\right) - 1 \end{bmatrix} \tag{2.71}$$

Linearized discretization of Equation 2.69 for a surface undergoing large deformations results in simple yet sufficiently accurate equations if a local reference frame is used at each discretized point. Without the use of a local reference frame inaccurate, numerically generated behavior arises when all or part of the object rotates, as the linearized tensor is no longer reference frame invariant. [8]

With the tangent of the deformed surface, $\left(\frac{\partial r}{\partial u}, \frac{\partial r}{\partial v}\right)$ as the local frame [13], the local rest state r is given as

$$r(a(u), b(v)) = s(u, v), \text{ with } \frac{\partial a}{\partial u} = \left\| \frac{\partial s}{\partial u} \right\| \text{ and } \frac{\partial b}{\partial v} = \left\| \frac{\partial s}{\partial v} \right\| \tag{2.72}$$

In using a local rest state based on the tangent of the deformed manifold, the local coordinates are usually not orthogonal. A discretizing grid that is as close to orthogonal in the original undeformed state as is possible reduces inaccuracy due to nonorthogonality. In the case of the rectangular heliogyro blades, the undeformed grid is orthogonal; hence, this source of error is excluded.

The local rest state r and the deformed state s are related by a deformation term, $d = s - r$. Utilizing d, linearization of the diagonal terms of Green's strain tensor proceeds as follows:

$$s(u, v) = r(u, v) + d(u, v) \tag{2.73}$$

$$\begin{aligned} G_{11} &= \frac{1}{2}\left(\left(\frac{\partial r}{\partial u} + \frac{\partial d}{\partial u}\right) \cdot \left(\frac{\partial r}{\partial u} + \frac{\partial d}{\partial u}\right) - 1\right) \\ &= \left(\frac{\partial r}{\partial u} \cdot \frac{\partial d}{\partial u}\right) + \frac{1}{2}\left(\frac{\partial d}{\partial u} \cdot \frac{\partial d}{\partial u}\right) \\ &= \frac{\partial r}{\partial u} \cdot \frac{\partial d}{\partial u} + O\left(\frac{\partial d}{\partial u}\right)^2 \\ &= \left(\frac{\partial s}{\partial u} - \frac{\partial r}{\partial u}\right) \cdot \frac{\partial r}{\partial u} + O\left(\frac{\partial d}{\partial u}\right)^2 \\ &= \left\| \frac{\partial s}{\partial u} \right\| - 1 + O\left(\frac{\partial d}{\partial u}\right)^2 \end{aligned} \tag{2.74}$$

The last equation of the derivation above is true because both $\frac{\partial s}{\partial u}$ and $\frac{\partial r}{\partial u}$ are in the same direction. Similarly,

$$G_{22} = \left\| \frac{\partial s}{\partial v} \right\| - 1 + O\left(\frac{\partial d}{\partial v}^2\right) \tag{2.75}$$

The off-diagonal shear terms of the Green's strain tensor stay the same.

Due to the nonorthogonality of the local reference frame, linearization of the off-diagonal terms with respect to the already sheared frame produces inaccurate results. These remain

quadratic. There is no significant computational penalty for retaining them. [8] Hence, the final form of the partially linearized Green's strain tensor is

$$\epsilon = \begin{bmatrix} \left\| \frac{\partial s}{\partial u} \right\| - 1 & \frac{1}{2}\left(\frac{\partial s}{\partial u} \cdot \frac{\partial s}{\partial v} \right) \\ \frac{1}{2}\left(\frac{\partial s}{\partial u} \cdot \frac{\partial s}{\partial v} \right) & \left\| \frac{\partial s}{\partial v} \right\| - 1 \end{bmatrix} \tag{2.76}$$

Assuming a linear relationship between stress and Green's strain tensor gives

$$\sigma_{ij} = C_{ijkl}\epsilon_{kl} \tag{2.77}$$

or

$$\begin{bmatrix} \sigma_{11} \\ \sigma_{22} \\ \sigma_{12} \end{bmatrix} = \begin{bmatrix} C_{1111} & C_{1122} & C_{1112} \\ C_{2211} & C_{2222} & C_{2212} \\ C_{1211} & C_{1222} & C_{1212} \end{bmatrix} \begin{bmatrix} \epsilon_{11} \\ \epsilon_{22} \\ \epsilon_{12} \end{bmatrix} \tag{2.78}$$

In this application, the diagonal terms are defined as $C_{1111} = K_1$, $C_{2222} = K_2$, and $C_{1212} = \frac{1}{2}\mu$, with μ being the shear modulus. As transverse contraction is a factor, the off-diagonal stress terms C_{1122} and C_{2211} are also included. The normal stress terms are therefore

$$\sigma_{11} = K_1\epsilon_{11} + C_{1122}\epsilon_{22} \tag{2.79}$$

$$\sigma_{22} = K_2\epsilon_{22} + C_{2211}\epsilon_{11} \tag{2.80}$$

Proceeding with discretization, the surface governing equation first becomes

$$\rho\frac{\partial^2 \vec{x}_{ij}}{\partial t^2} - \left[\frac{\partial \sigma_{11}}{\partial u}\vec{r}_u + \frac{\partial \sigma_{12}}{\partial u}\vec{r}_v + \frac{\partial \sigma_{21}}{\partial v}\vec{r}_u + \frac{\partial \sigma_{22}}{\partial v}\vec{r}_v \right]_{i,j} = \vec{f}_{ij} \tag{2.81}$$

where $\vec{r}_u \left(= \left. \frac{\partial \vec{r}}{\partial u} \right|_{i,j} \right)$ and $\vec{r}_v \left(= \left. \frac{\partial \vec{r}}{\partial v} \right|_{i,j} \right)$ comprise the local 2-D material coordinate system and the expression in brackets represents an approximation to the true divergence of the stress. Then, setting the nodal spacing equal to b, the discretized stress divergence is

(2.82)

$$\begin{aligned}\frac{\partial \sigma_{11}}{\partial u}\vec{r}_u &= K_1 \left.\frac{\partial \epsilon_{11}}{\partial u}\right|_{u_i,v_j} \vec{r}_u(u_i,v_j) + C_{1122} \left.\frac{\partial \epsilon_{22}}{\partial u}\right|_{u_i,v_j} \vec{r}_u(u_i,v_j) \\ &= K_1 \left(\frac{\|x_{i+1,j} - x_{i,j}\| - b}{b^2} \frac{(x_{i+1,j} - x_{i,j})}{\|x_{i+1,j} - x_{i,j}\|} - \frac{\|x_{i,j} - x_{i-1,j}\| - b}{b^2} \frac{(x_{i,j} - x_{i-1,j})}{\|x_{i,j} - x_{i-1,j}\|} \right) \\ &+ C_{1122} \left(\frac{\|x_{i+1,j+1} - x_{i+1,j-1}\| - \|x_{i-1,j+1} - x_{i-1,j-1}\|}{(2b)^2} \right) \frac{(x_{i+1,j} - x_{i-1,j})}{\|x_{i+1,j} - x_{i-1,j}\|} + O(b)\end{aligned}$$

The term $\frac{\partial \sigma_{22}}{\partial v}\vec{r}_v$ follows similarly. Discretizing $\sigma_{12} = \sigma_{21} \approx \frac{\mu}{2}\frac{\partial s}{\partial u} \cdot \frac{\partial s}{\partial v}$ results in

$$\sigma_{12} = \frac{\mu}{8b^2} (x_{i+1,j} - x_{i-1,j}) \cdot (x_{i,j+1} - x_{i,j-1}) + O(b^2) \tag{2.83}$$

and

$$\frac{\partial \sigma_{12}}{\partial v}\vec{r}_u = \frac{\sigma_{12_{i,j+1}} - \sigma_{12_{i,j-1}}}{2b} \frac{(x_{i+1,j} - x_{i-1,j})}{\|x_{i+1,j} - x_{i-1,j}\|} \tag{2.84}$$

$$\frac{\partial \sigma_{21}}{\partial u}\vec{r}_v = \frac{\sigma_{21_{i+1,j}} - \sigma_{21_{i-1,j}}}{2b} \frac{(x_{i,j+1} - x_{i,j-1})}{\|x_{i,j+1} - x_{i,j-1}\|} \tag{2.85}$$

An alternative to modeling shear and contraction separately is to combine them using diagonal springs in the square mesh [17]. For a square undergoing pure shear, the shearing angle is related to the change in the diagonal length (Figure 2.9):

$$\begin{aligned}(d + \Delta d)^2 &= 2b^2 \left(1 - \cos\left(\frac{\pi}{2} + \phi\right)\right) \\ &= d^2 (1 + \sin\phi)\end{aligned} \tag{2.86}$$

If ϕ, and therefore Δd, are small, then

$$\frac{2\Delta d}{d} \approx \phi \tag{2.87}$$

Since $\epsilon_{shear} = \frac{\phi}{2} = \frac{\Delta d}{d}$, the shear equation is written

$$\tau = 2G\epsilon_{shear} = \frac{E}{1+\nu}\epsilon_{shear} = \frac{E}{1+\nu}\frac{\Delta}{d} \tag{2.88}$$

The force along the edge of the square is the shear times the cross-sectional area of the material, or

$$F \approx \frac{EA}{1+\nu}\frac{\Delta d}{d} \tag{2.89}$$

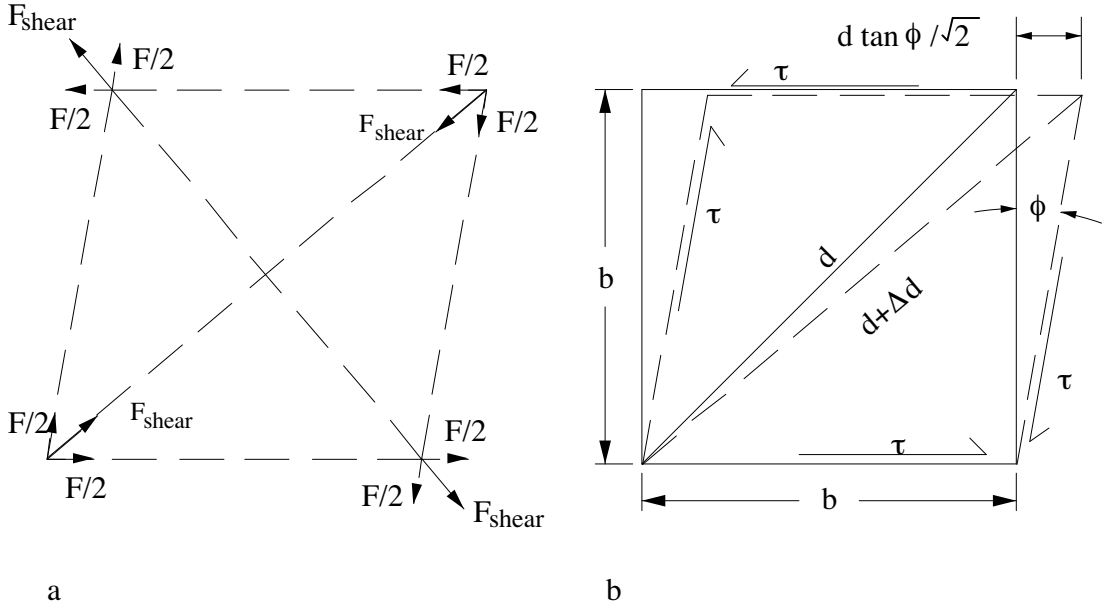


Figure 2.9: Shear force diagram for a square in a membrane mesh.

Distributing the shear force at the corners of a four-particle mesh as shown in Figure 2.9 gives

$$F_{shear} = \frac{\sqrt{2}}{2}F = \frac{EA}{2b(1+\nu)}\Delta d \tag{2.90}$$

For a square mesh, with point x_1 at one end of a diagonal and point x_2 at the other,

$$\Delta d = \left\|\vec{P}_{x_2} - \vec{P}_{x_1}\right\| - \sqrt{2}b \tag{2.91}$$

so that

$$\vec{F}_{shear} = \frac{EA}{2b(1+\nu)} \left(\left\| \vec{P}_{x_2} - \vec{P}_{x_1} \right\| - \sqrt{2}b \right) \frac{(\vec{P}_{x_2} - \vec{P}_{x_1})}{\left\| \vec{P}_{x_2} - \vec{P}_{x_1} \right\|} \tag{2.92}$$

$$= \frac{EA}{2(1+\nu)} \left(\frac{1}{b} - \frac{\sqrt{2}}{\left\| \vec{P}_{x_2} - \vec{P}_{x_1} \right\|} \right) (\vec{P}_{x_2} - \vec{P}_{x_1})$$

$$= \frac{EA}{\sqrt{2}(1+\nu)} \left(\frac{1}{\sqrt{2}b} - \frac{1}{\left\| \vec{P}_{x_2} - \vec{P}_{x_1} \right\|} \right) (\vec{P}_{x_2} - \vec{P}_{x_1})$$

As elongation occurs, the diagonal springs resist, pulling in both the elongated direction and the direction perpendicular to elongation.

Proper physical representation requires a material dissipative force. Incorporating damping in the equations entails interaction between two particles, P_{x_1} and P_{x_2}, based on the velocity difference along the lines connecting the two particles, as follows:

$$\left\| \vec{F}_{damp} \right\| = C \left(\dot{\vec{P}}_{x_2} - \dot{\vec{P}}_{x_1} \right) \cdot \vec{P}_d \tag{2.93}$$

where C is a damping constant and $\vec{P}_d$ is the unit vector from P_{x_1} to P_{x_2}. Damping exclusively along the adjoining vector eliminates spurious forces that otherwise would dampen legitimate rigid body motion. A damping force is placed between a discretized particle and each of its immediate neighbors.

The body force $\vec{f}_{ij}$ consists of gravity and solar pressure forces. Gravitational force is given by Equation 2.94,

$$\vec{F}_{grav} = -\frac{GM_A M_B}{\left\| \vec{P}_d \right\|^2} \vec{P}_d \tag{2.94}$$

and solar force is given by Equation 2.64.

To calculate the solar force, the blade mesh is divided into triangles, with the solar force divided among the three nodes comprising each triangle. For a triangle with nodes 1, 2, and 3, the vectors $\vec{A} = \vec{P}_2 - \vec{P}_1$ and $\vec{B} = \vec{P}_3 - \vec{P}_1$ are computed. The following calculations then follow.

$$C_1 = \frac{S\, f_r}{c}\left(\frac{r_0}{r_s}\right)^2 \tag{2.95}$$

$$C_2 = \frac{S\,(1-f_r)}{2c}\left(\frac{r_0}{r_s}\right)^2 \tag{2.96}$$

$$\vec{D} = \vec{A} \times \vec{B} \tag{2.97}$$

$$\cos\theta = \frac{\vec{D}}{\left\|\vec{D}\right\|} \cdot \vec{Sun} \tag{2.98}$$

$$\vec{N} = \frac{\vec{D}}{\left\|\vec{D}\right\|} \tag{2.99}$$

$$\vec{F}_{Solar} = C_1 \cos\theta^2 \vec{D} + C_2 \cos\theta \left\|\vec{D}\right\| \vec{Sun} \tag{2.100}$$

Incorporating all the various parts of the derivation, the finite difference discretization of the equation of motion for a point on a surface in 3-D space is

$$m_{ij}\ddot{\vec{P}}_{ij} = \sum_{l=1}^{4} \vec{F}_{stretch} + \sum_{l=1}^{4} \vec{F}_{shear} + \sum_{l=1}^{8} \vec{F}_{damp} + \vec{F}_{grav} + \vec{F}_{Solar} \tag{2.101}$$

or

$$\begin{aligned} m_{ij}\ddot{\vec{P}}_{ij} = {} & \sum_{l=1}^{4} \frac{EA}{b}\left[\frac{1}{b} - \frac{1}{\left\|\vec{P}_d\right\|}\right]\vec{P}_d + \sum_{l=1}^{4} \frac{EA}{\sqrt{2}\,(1+\nu)}\left[\frac{1}{\sqrt{2}b} - \frac{1}{\left\|\vec{P}_d\right\|}\right]\vec{P}_d + \sum_{l=1}^{8}\left[C\dot{\vec{P}}_d \cdot \frac{\vec{P}_d}{\left\|\vec{P}_d\right\|}\right] \\ & + \frac{GM_{Sun}m_{ij}}{\left\|\vec{P}_{Sun}\right\|^2}\vec{P}_{Sun} + \frac{GM_{Earth}m_{ij}}{\left\|\vec{P}_{Earth}\right\|^2}\vec{P}_{Earth} + \frac{GM_{moon}m_{ij}}{\left\|\vec{P}_{moon}\right\|^2}\vec{P}_{moon} + \vec{F}_{Solar} \end{aligned} \tag{2.102}$$

Alterations to the expressions for stretch and shear accommodate battens and nonlinear membrane behavior. Assume a batten, as shown in Figure 2.10, made of a square of blade material 10 times the thickness of the rest of the blade. One end of the material is fused to the blade and the other is temporarily held in place by an adhesive that rapidly sublimates in a vacuum environment. Differential residual stress causes the material to tightly wind up into a slender roll.The inclusion of battens along the length of each blade requires chord-wise bending stiffness in the material mesh at each batten location. Figure 2.11 illustrates a simple way to construct the battens by creating linear stiffness springs between each node

along the batten, as well as between the nodes at both ends of the batten. Stiffness for each batten spring is

$$K_{batten} = EA_{xs}/w \tag{2.103}$$

where

$$\begin{aligned} A_{xs} &= 10\,t\,l \\ t &= \text{thickness of blade material} \\ l &= \text{length of batten roll} \\ w &= \text{length of batten spring} \end{aligned}$$

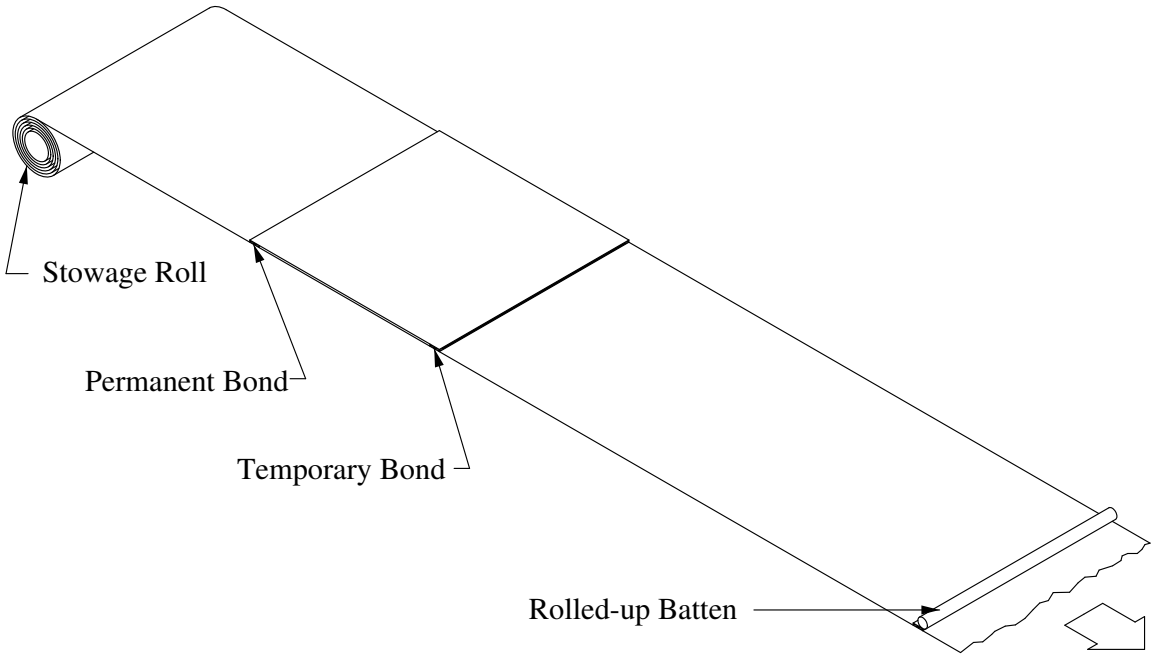


Figure 2.10: Batten implementation in heliogyro blade [22]

Solar sail material acts like a membrane. It supports tension loads, but immediately buckles or wrinkles under compressive loads. Approximating the behavior of the blade material thus requires a nonlinear spring. The expression for nonlinear stiffness must be continuous to allow smooth integration, but must also quickly rise to its full value under a small amount of stretch and quickly go to zero under a small amount of compression. To

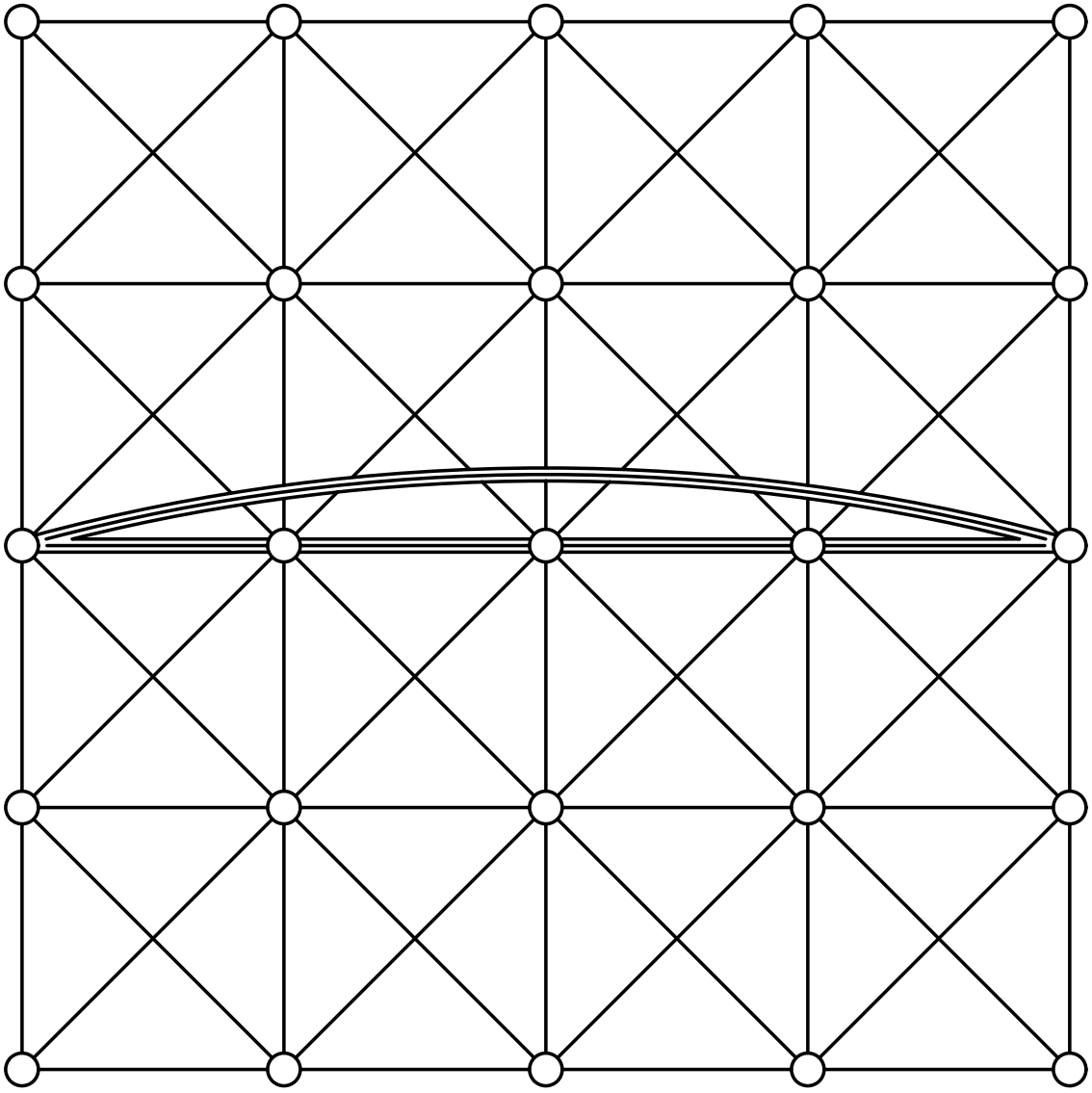


Figure 2.11: Spring configuration for a batten, incorporated into the mesh of tension and shear springs that comprise a section of blade. The linear batten springs appear as three lines together.

accomplish this, the nonlinear function in Equation 2.104 multiplies the stretch and shear expressions in Equation 2.102 for all nodes except those representing battens:

$$f_{nonlin} = \frac{\arctan\left[K\left[\frac{\|\vec{P}_d\|}{w} - 1\right]\right]}{\pi} + 0.5 \tag{2.104}$$

where w is the length of the spring.

The parameter K in Equation 2.104 is key to meeting the criteria for proper membrane stiffness. Figure 2.12 plots f_{nonlin} vs. stretch, or $\left[\frac{\|\vec{P}_d\|}{w} - 1\right]$, for a range of values of K. A value of 2 gives almost a straight line, but a value of $20,000$ adequately approximates the sought-after behavior of nearly zero compresive stiffness but full tensile stiffness.

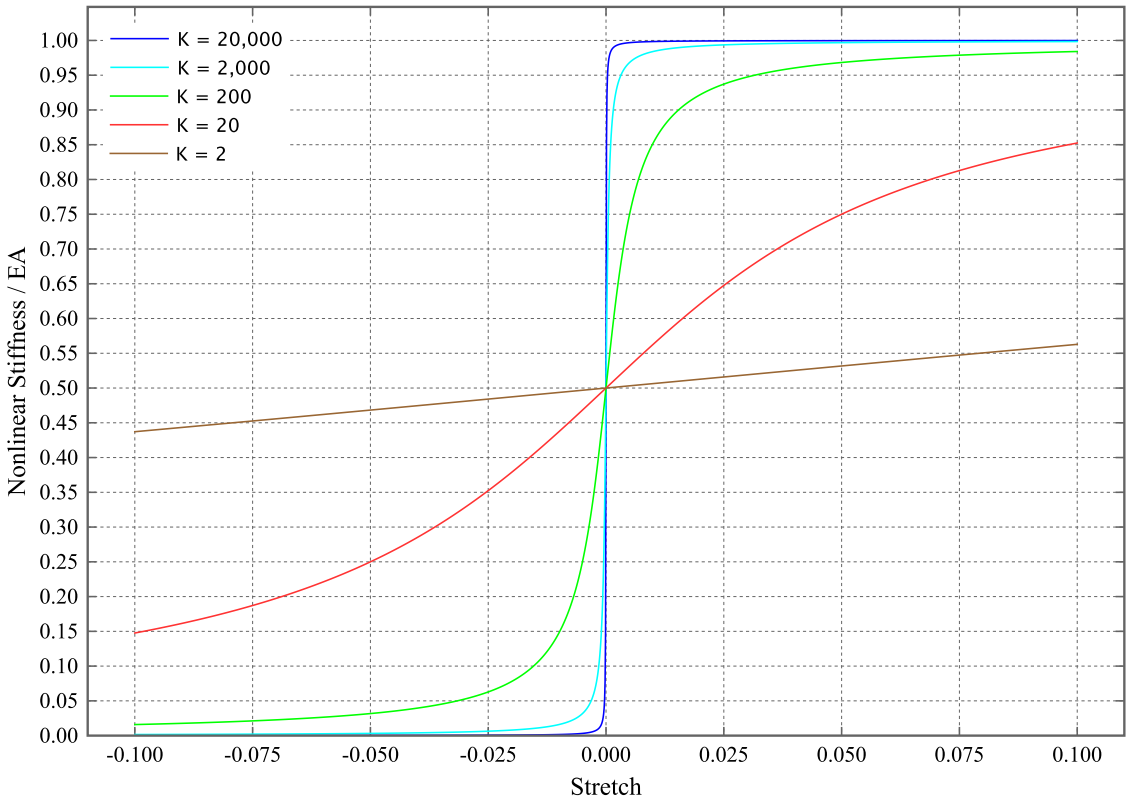


Figure 2.12: Nonlinear stiffness relation for various values of K.

The particle model equation is stiff – meaning that the natural frequencies of the lumped mass motions is high. Each mass is on the order of $0.1\,mg$ and the tensile stiffness is on the order of $1\,kN/m$. Explicit methods require very small time steps to solve this equation, while

first-order implicit methods, while typically fast and stable, can be inaccurate. Higher-order implicit formulas are more accurate and enable large time steps, but take longer to compute. The method chosen to solve the particle model equation, the second-order Backward finite Difference Formula, or BDF2, is a balance between speed and accuracy. The BDF2 allows time steps on the order of 0.01 seconds, $10,000$ times faster than explicit Euler or Runge-Kutta, but also is accurate and stable [14].

Due to the nonlinearity and large deformation possible in the blade, the Newton-Raphson root finding method iteratively solves the BDF2 equation. With this in mind, setup of the BDF2 equation proceeds as follows.

The Newton-Raphson formula for a function g is

$$\frac{\partial g}{\partial \vec{v}_i} \cdot \left(\vec{v}_{i_{k+1}} - \vec{v}_{i_k}\right) = -g \tag{2.105}$$

The function g arises from the second order backward finite difference formulation of Newton's second law for the velocity, $\vec{v}$ and position $\vec{x}$ of a particle at time step i, or

$$\frac{d\vec{v}_i}{dt} = \frac{3\vec{v}_i - 4\vec{v}_{i-1} + \vec{v}_{i-2}}{2h} = M^{-1}F_i\left(\vec{x}_i, \vec{v}_i\right) \tag{2.106}$$

$$\frac{d\vec{x}_i}{dt} = \frac{3\vec{x}_i - 4\vec{x}_{i-1} + \vec{x}_{i-2}}{2h} = \vec{v}_i \tag{2.107}$$

Equation 2.106 provides g:

$$M\vec{v}_i - \frac{4}{3}M\vec{v}_{i-1} + \frac{1}{3}M\vec{v}_{i-2} - \frac{2}{3}h\vec{F}_i = g\left(\vec{x}_i, \vec{v}_i\right) \tag{2.108}$$

Since $\vec{F}_i$ is a function of $\vec{x}_i$ and $\vec{v}_i$,

$$\frac{\partial \vec{F}\left(\vec{x}_i, \vec{v}_i\right)}{\partial \vec{v}_i} = \frac{\partial \vec{F}}{\partial \vec{x}_i}\frac{\partial \vec{x}_i}{\partial \vec{v}_i} + \frac{\partial \vec{F}}{\partial \vec{v}_i} = \frac{2}{3}h\frac{\partial \vec{F}}{\partial \vec{x}_i} + \frac{\partial \vec{F}}{\partial \vec{v}_i} \tag{2.109}$$

Hence,

$$\frac{\partial g}{\partial \vec{v}_i} = M - \frac{4}{9}h^2\frac{\partial \vec{F}}{\partial \vec{x}_i} - \frac{2}{3}h\frac{\partial \vec{F}}{\partial \vec{v}_i} \tag{2.110}$$

Inserting Equations 2.108 and 2.110 into Equation 2.105 results in the iterative equation for the update for $\Delta\vec{v}_{i_k}$:

$$\left(M - \frac{4}{9}h^2\frac{\partial \vec{F}_i}{\partial \vec{x}_i} - \frac{2}{3}h\frac{\partial \vec{F}}{\partial \vec{v}_i}\right)\Delta\vec{v}_{i_k} = -g\left(\vec{x}_{i_k}, \vec{v}_{i_k}\right) \tag{2.111}$$

or

$$A\Delta\vec{v}_{i_k} = b \tag{2.112}$$

Calculating the $\frac{\partial \vec{F}}{\partial \vec{v}}$ and $\frac{\partial \vec{F}}{\partial \vec{x}}$ terms is straightforward but requires careful bookkeeping. Derivations of these Jacobian-like terms for spring forces, damping, gravity, and force due to solar pressure appear in Appendix B.

The matrix A in Equation 2.112 is sparse and large. A 5×4001 mesh for a $1m \times 1000m$ blade has 20005 nodes, each with three degrees of freedom. The A matrix then has $60015 \times 60015 = 3.6018 \times 10^9$ entries, but only $1,224,072$ nonzero entries. The A matrix is only 0.034% filled.

The preconditioned biconjugate gradient algorithm, a preferred method for sparse matrix equations, efficiently solves Equation 2.112. The algorithm reduces convergence time by multiplying both sides of Equation 2.112 with a preconditioner matrix that roughly approximates A. In this case, the preconditioner is the inverse mass matrix. The choice of a biconjugate method allows asymmetry, which is present in A due to damping terms. A modified row-indexed sparse storage mode [32] compactly stores A.

Each time step begins with binomial extrapolation to estimate the new particle velocities and positions. Determination of the preconditioned A matrix and b vector occur at each Newton-Raphson iteration.

The motion of the root edge of the blade perfectly mimics the preimposed motion of the blade root holder. They therefore require no velocity and position update. To properly handle the constraint nodes, the A matrix is pre- and post-multiplied by a diagonal matrix with ones on the diagonal except for zeros on the rows corresponding to equations for the constraint particles. The b vector is also premultiplied by this matrix. In this way, the system of discretized equations reduces in size and $\Delta\vec{v}$ for the constraint modes is not computed. To maintain a nonsingular A matrix, a diagonal matrix with zeros on the diagonal except for ones on the constraint rows is added to A, thus formally setting $\Delta\vec{v}$ for the constraint nodes equal to zero. Equation 2.112 is then solved via the conjugate gradient

algorithm. If the results from the solver do not converge, a sufficiently large increase in the iterations for both the conjugate gradient solver and for the Newton Raphson equation will cause the solution to converge.

2.4 Kane Blade Heliogyro

Like the stiff blade model, the Kane heliogyro model consists of a rigid-body central core and evenly spaced rigid-body blade root holders. Instead of stiff blades, however, the Kane model incorporates flexible polyimide blades.

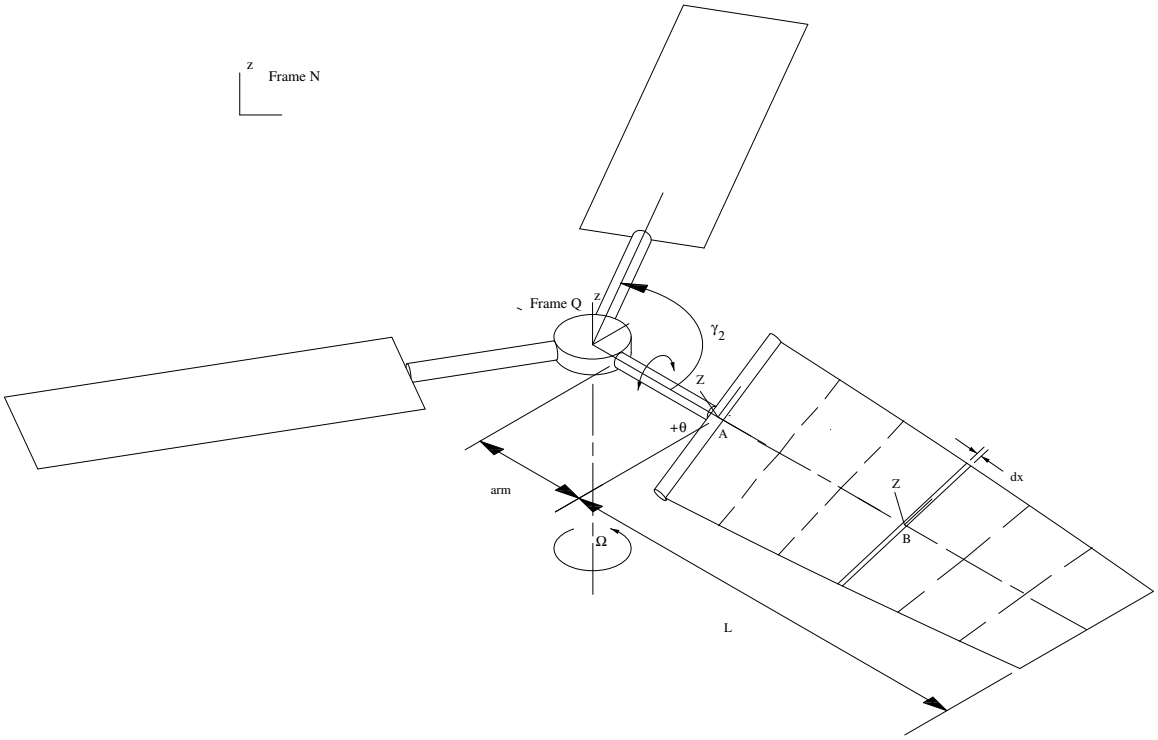


Figure 2.13: Heliogyro model corresponding to Kane derivation.

Blade deflection is represented using an assumed modes approach, and is derived from Kane's equation [19]. Each blade has ν degrees of freedom, corresponding to the number of assumed modes specified. Thus, the number of generalized speeds of the model are 6 for the core and ν for each blade. The motion of each blade root holder with respect to the core is specified through a control strategy; the blade holders, therefore, have no accompanying

generalized speed.

Generalized inertia forces (F_u^*) for each body and generalized active forces (F_u) for every active force location in the Kane model are given below.

(2.113)

$$\begin{aligned} F_{u_i}^* = & \frac{\partial}{\partial u_i}\left({}^{Q}\dot{\vec{P}}_{NQ}\right) \cdot {}^{Q}F_{in_Q} + \frac{\partial}{\partial u_i}\left({}^{Q}\vec{\omega}_{NQ}\right) \cdot {}^{Q}T_{in_Q} + \frac{\partial}{\partial u_i}\left({}^{A_i}\dot{\vec{P}}_{NA_i}\right) \cdot {}^{A_i}F_{in_{A_i}} \\ & + \frac{\partial}{\partial u_i}\left({}^{A_i}\vec{\omega}_{NA_i}\right) \cdot {}^{A_i}T_{in_{A_i}} - \int_0^L \rho \left[\frac{\partial}{\partial u_i}\left({}^{A_i}\dot{\vec{P}}_{Nc}\right)\right]_{lin} \cdot \left[{}^{A_i}\ddot{\vec{P}}_{Nc}\right]_{lin} dx \\ & - \int_0^L \left[\frac{\partial}{\partial u_i}\left({}^{B_i}\vec{\omega}_{NB_i}\right)\right]_{lin} \cdot \left(\left[{}^{B_i}\vec{\alpha}_{NB_i}\right]_{lin} \cdot \underline{\mathbf{I}}_{B_i} + \left[{}^{B_i}\vec{\omega}_{NB_i}\right]_{lin} \times \underline{\mathbf{I}}_{B_i} \cdot \left[{}^{B_i}\vec{\omega}_{NB_i}\right]_{lin}\right) dx \end{aligned}$$

(2.114)

$$\begin{aligned} F_{u_i} = & \frac{\partial}{\partial u_i}\left({}^{Q}\dot{\vec{P}}_{NQ}\right) \cdot {}^{Q}\vec{G}_{Core} + \frac{\partial}{\partial u_i}\left({}^{A_i}\vec{\omega}_{QA_i}\right) \cdot {}^{A_i}\vec{T}_{QA_i} \\ & + \frac{\partial}{\partial u_i}\left({}^{A_i}\dot{\vec{P}}_{NA_i}\right) \cdot \left(-{}^{A_i}\vec{F}_{A_iBlade} + {}^{A_i}\vec{G}_{A_i}\right) - \frac{\partial}{\partial u_i}\left({}^{A_i}\vec{\omega}_{NA_i}\right) \cdot {}^{A_i}\vec{T}_{A_iBlade} \\ & + \int_0^L \left[\frac{\partial}{\partial u_i}\left({}^{A_i}\dot{\vec{P}}_{Nc}\right)\right]_{lin} \cdot \left({}^{A_i}\vec{F}_{B_i} + {}^{A_i}\vec{G}_{B_i} + {}^{A_i}S\vec{u}n_{B_i}\right) dx \\ & + \int_0^L \left[\frac{\partial}{\partial u_i}\left({}^{B_i}\vec{\omega}_{NB_i}\right)\right]_{lin} \cdot {}^{B_i}\vec{T}_{B_i}\, dx \end{aligned}$$

The remainder of the section involves the derivation of first, the terms in $F_{u_i}^*$ and F_{u_i} directly related to the core; and then, the terms related to a blade. The governing dynamic equations appear at the end. Since the motion of the blade root holders with respect to the core is prescribed, the term $\frac{\partial}{\partial u_i}\left({}^{A_i}\vec{\omega}_{QA_i}\right) \cdot {}^{A_i}\vec{T}_{QA_i}$ in Equation 2.114 equals zero and is dropped from this point on.

2.4.1 Core

Terms from $F_{u_i}^*$ and F_{u_i} associated primarily with the core and the blade root holders are

(2.115)
$$\begin{aligned} F_{u_i}^* : \quad & \frac{\partial}{\partial u_i}\left({}^{Q}\dot{\vec{P}}_{NQ}\right) \cdot {}^{Q}F_{in_Q} + \frac{\partial}{\partial u_i}\left({}^{Q}\vec{\omega}_{NQ}\right) \cdot {}^{Q}T_{in_Q} + \frac{\partial}{\partial u_i}\left({}^{A_i}\dot{\vec{P}}_{NA_i}\right) \cdot {}^{A_i}F_{in_{A_i}} \\ & + \frac{\partial}{\partial u_i}\left({}^{A_i}\vec{\omega}_{NA_i}\right) \cdot {}^{A_i}T_{in_{A_i}} \end{aligned}$$

(2.116)
$$\begin{aligned} F_{u_i} : \quad & \frac{\partial}{\partial u_i}\left({}^{Q}\dot{\vec{P}}_{NQ}\right) \cdot {}^{Q}\vec{G}_{Core} + \frac{\partial}{\partial u_i}\left({}^{A_i}\dot{\vec{P}}_{NA_i}\right) \cdot \left(-{}^{A_i}\vec{F}_{A_iBlade} + {}^{A_i}\vec{G}_{A_i}\right) \\ & - \frac{\partial}{\partial u_i}\left({}^{A_i}\vec{\omega}_{NA_i}\right) \cdot {}^{A_i}\vec{T}_{A_iBlade} \end{aligned}$$

Generalized coordinates and speeds of the core are $[q_1, q_2, \ldots q_6, q_7]$ and $[u_{s1}, u_{s2}, \ldots u_{s5}, u_{s6}]$, respectively.

The terms in Equations 2.115 and 2.116 except for ${}^{A_i}\vec{F}_{A_i Blade}$ and ${}^{A_i}\vec{T}_{A_i Blade}$ are previously derived in Section 2.2 and are not repeated here. Development of the remaining terms, ${}^{A_i}\vec{F}_{A_i Blade}$ and ${}^{A_i}\vec{T}_{A_i Blade}$, occurs in the blade derivation section.

2.4.2 Blade

Using an assumed modes approach, the blade model incorporates extension, deflection, bending and twist into a subset of coupled equations. Terms from $F^*_{u_i}$ and F_{u_i} associated mainly with the blade are

(2.117)

$$\begin{aligned} F^*_{u_i}: \quad & -\int_0^L \rho \left[\frac{\partial}{\partial u_i}\left({}^{A_i}\dot{\vec{P}}_{Nc}\right)\right]_{lin} \cdot \left[{}^{A_i}\ddot{\vec{P}}_{Nc}\right]_{lin} dx \\ & -\int_0^L \left[\frac{\partial}{\partial u_i}\left({}^{B_i}\vec{\omega}_{NB_i}\right)\right]_{lin} \cdot \left(\left[{}^{B_i}\vec{\alpha}_{NB_i}\right]_{lin} \cdot \underline{\mathbf{I}}_{B_i} + \left[{}^{B_i}\vec{\omega}_{NB_i}\right]_{lin} \times \underline{\mathbf{I}}_{B_i} \cdot \left[{}^{B_i}\vec{\omega}_{NB_i}\right]_{lin}\right) dx \end{aligned}$$

(2.118)

$$\begin{aligned} F_{u_i}: \quad & \int_0^L \left[\frac{\partial}{\partial u_i}\left({}^{A_i}\dot{\vec{P}}_{Nc}\right)\right]_{lin} \cdot \left({}^{A_i}\vec{F}_{B_i} + {}^{A_i}\vec{G}_{B_i} + {}^{A_i}\vec{Sun}_{B_i}\right) dx \\ & + \int_0^L \left[\frac{\partial}{\partial u_i}\left({}^{B_i}\vec{\omega}_{NB_i}\right)\right]_{lin} \cdot {}^{B_i}\vec{T}_{B_i}\, dx \end{aligned}$$

Figure 2.14 illustrates the frames used in the blade derivation. In the undeformed case, the blade is flat and straight. The base of the blade attaches to the blade root holder at Frame A. Local reference frame B is located a distance x from the blade root at point E, the elastic center of the differential element, dx. Frame B has the same initial orientation as Frame A. The eccentricity vector $[0\ e_2\ e_3]^T$, represented in Frame B coordinates, connects the centroid of the differential element, C, with the elastic center.

In the deformed case, the vector $\vec{u}$ represents the displacement of the differential element with respect to its initial position, and the vector $[\theta_1\ \theta_2\ \theta_3]^T$ represents the twist and bending about the x, y, and z axes of Frame A. The rotation matrix ${}^{A_i}R_{B_i}$, is comprised of $[\theta_1\ \theta_2\ \theta_3]^T$ through the following convention [19]:

$$ {}^{A_i}R_{B_i} = R_z(\theta_3)R_y(\theta_2)R_x(\theta_1) \tag{2.119} $$

$$ = \begin{bmatrix} c_2c_3 & s_1s_2c_3 - s_3c_1 & c_1s_2c_3 + s_3s_1 \\ c_2s_3 & s_1s_2s_3 + c_3c_1 & c_1s_2s_3 - c_3s_1 \\ -s_2 & s_1c_2 & c_1c_2 \end{bmatrix} \tag{2.120} $$

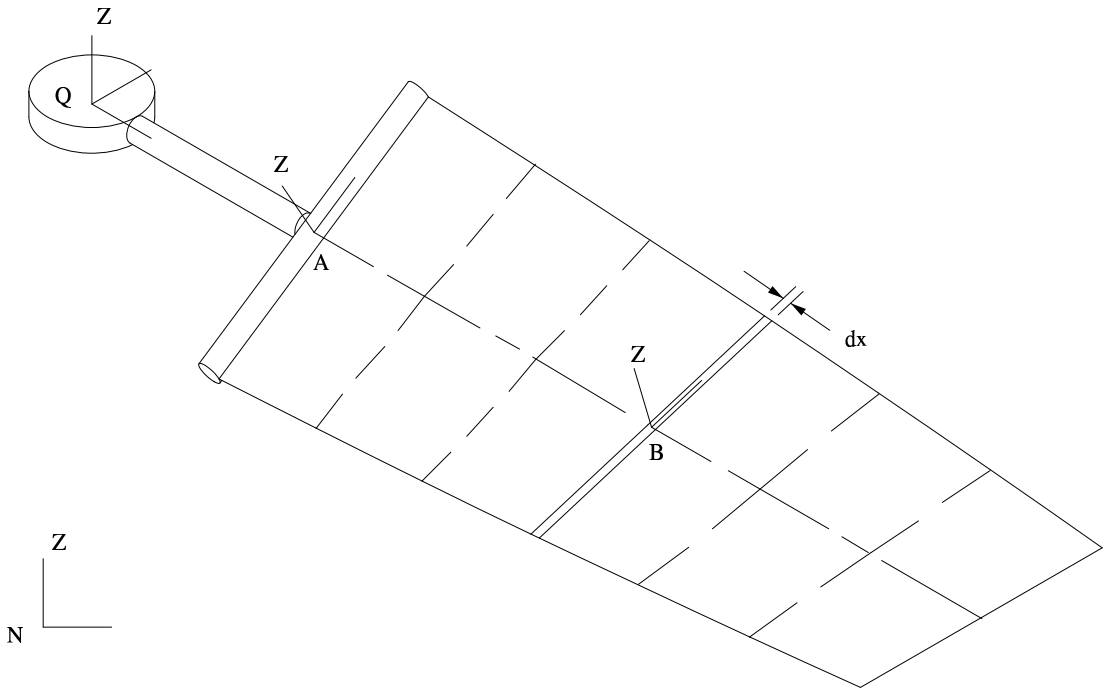


Figure 2.14: Frames for Single Blade Derivation.

The position vector from the origin N to the centroid, c, of the differential element along the length of the blade is given as follows:

$$ {}^N\vec{P}_{Nc} = {}^N\vec{P}_{NQ} + {}^NR_Q{}^QR_{A_i}{}^{A_i}\vec{P}_{QA_i} + {}^NR_Q{}^QR_{A_i}{}^{A_i}\vec{P}_{A_ic} \tag{2.121} $$

where

$$^{A_i}\vec{P}_{A_ic} = {}^{A_i}\vec{r} + {}^{A_i}\vec{u} + {}^{A_i}R_{B_i}\begin{bmatrix}0\\e_2\\e_3\end{bmatrix} \tag{2.122}$$

$$^{A_i}\vec{r} = \begin{bmatrix}x\\0\\0\end{bmatrix} \tag{2.123}$$

$$^{A_i}\vec{u} = \begin{bmatrix}u_1\\u_2\\u_3\end{bmatrix} \tag{2.124}$$

(2.125)

The velocity vector from N to c is:

$$\begin{aligned} {}^N\dot{\vec{P}}_{Nc} = {}^N\dot{\vec{P}}_{NQ} + {}^N\vec{\omega}_{NQ} \times {}^NR_Q{}^QR_{A_i}{}^{A_i}\vec{P}_{QA_i} + {}^NR_Q\left({}^Q\vec{\omega}_{QA_i} \times {}^QR_{A_i}{}^{A_i}\vec{P}_{QA_i}\right) \\ + {}^N\vec{\omega}_{NQ} \times {}^NR_Q{}^QR_{A_i}{}^{A_i}\vec{P}_{A_ic} + {}^NR_Q\left({}^Q\vec{\omega}_{QA_i} \times {}^QR_{A_i}{}^{A_i}\vec{P}_{A_ic}\right) \\ + {}^NR_Q{}^QR_{A_i}\left({}^{A_i}\dot{\vec{u}} + {}^{A_i}\vec{\omega}_{A_iB_i} \times {}^{A_i}R_{B_i}\begin{bmatrix}0\\e_2\\e_3\end{bmatrix}\right) \end{aligned} \tag{2.126}$$

Since the velocity vector from N to A_i is

$$^N\dot{\vec{P}}_{NA_i} = {}^N\dot{\vec{P}}_{NQ} + {}^N\vec{\omega}_{NQ} \times {}^NR_Q{}^QR_{A_i}{}^{A_i}\vec{P}_{QA_i} + {}^NR_Q\left({}^Q\vec{\omega}_{QA_i} \times {}^QR_{A_i}{}^{A_i}\vec{P}_{QA_i}\right) \tag{2.127}$$

$^N\dot{\vec{P}}_{Nc}$ can be written

(2.128)

$$\begin{aligned} {}^N\dot{\vec{P}}_{Nc} = {}^N\dot{\vec{P}}_{NA_i} + {}^N\vec{\omega}_{NQ} \times {}^NR_Q{}^QR_{A_i}{}^{A_i}\vec{P}_{A_ic} \\ + {}^NR_Q\left({}^Q\vec{\omega}_{QA_i} \times {}^QR_{A_i}{}^{A_i}\vec{P}_{A_ic}\right) + {}^NR_Q{}^QR_{A_i}\left({}^{A_i}\dot{\vec{u}} + {}^{A_i}\vec{\omega}_{A_iB_i} \times {}^{A_i}R_{B_i}\begin{bmatrix}0\\e_2\\e_3\end{bmatrix}\right) \end{aligned}$$

Multiplying Equation 2.128 by ${}^{A_i}R_N$ and consolidating terms gives

$$(2.129) \qquad {}^{A_i}\dot{\vec{P}}_{Nc} = {}^{A_i}\dot{\vec{P}}_{NA_i} + {}^{A_i}\vec{\omega}_{NA_i} \times {}^{A_i}\vec{P}_{A_ic} + {}^{A_i}\dot{\vec{u}} + {}^{A_i}\vec{\omega}_{A_iB_i} \times {}^{A_i}R_{B_i} \begin{bmatrix} 0 \\ e_2 \\ e_3 \end{bmatrix}$$

Following Kane's rotation matrix convention for ${}^{A_i}R_{B_i}$, the angular velocity of a beam differential element with respect to the root is obtained:

$$(2.130) \qquad {}^{A_i}\vec{\omega}_{A_iB_i} = \dot{\theta}_3 \begin{bmatrix} 0 \\ 0 \\ 1 \end{bmatrix} + \dot{\theta}_2 R_z(\theta_3) \begin{bmatrix} 0 \\ 1 \\ 0 \end{bmatrix} + \dot{\theta}_1 R_z(\theta_3) R_y(\theta_2) \begin{bmatrix} 1 \\ 0 \\ 0 \end{bmatrix}$$

$$= \begin{bmatrix} -s_3\dot{\theta}_2 & + & c_3c_2\dot{\theta}_1 \\ c_3\dot{\theta}_2 & + & c_2s_3\dot{\theta}_1 \\ \dot{\theta}_3 & - & s_2\dot{\theta}_1 \end{bmatrix}$$

All of the terms for ${}^{A_i}\dot{\vec{P}}_{Nc}$ are then defined.

Kane's equations also require the acceleration vector

(2.131)

$${}^{A_i}\ddot{\vec{P}}_{Nc} = {}^{A_i}\ddot{\vec{P}}_{NA_i} + {}^{A_i}\vec{\alpha}_{NA_i} \times {}^{A_i}\vec{P}_{A_ic} + {}^{A_i}\vec{\omega}_{NA_i} \times \left({}^{A_i}\vec{\omega}_{NA_i} \times {}^{A_i}\vec{P}_{A_ic} \right) + 2\, {}^{A_i}\vec{\omega}_{NA_i} \times {}^{A_i}\dot{\vec{P}}_{A_ic}$$
$$+ {}^{A_i}\ddot{\vec{P}}_{A_ic} + {}^{A_i}\vec{\omega}_{A_iB_i} \times \left({}^{A_i}\vec{\omega}_{A_iB_i} \times \left({}^{A_i}R_{B_i} \cdot \begin{bmatrix} 0 \\ e_2 \\ e_3 \end{bmatrix} \right) \right)$$

for which the terms ${}^{A_i}\dot{\vec{P}}_{A_ic}$, ${}^{A_i}\ddot{\vec{P}}_{A_ic}$ are determined to be

$$(2.132) \qquad {}^{A_i}\dot{\vec{P}}_{A_ic} = {}^{A_i}\dot{\vec{u}} + {}^{A_i}\vec{\omega}_{A_iB_i} \times {}^{A_i}R_{B_i} \begin{bmatrix} 0 \\ e_2 \\ e_3 \end{bmatrix}$$

$$(2.133) \qquad {}^{A_i}\ddot{\vec{P}}_{A_ic} = {}^{A_i}\ddot{\vec{u}} + {}^{A_i}\vec{\alpha}_{A_iB_i} \times {}^{A_i}R_{B_i} \begin{bmatrix} 0 \\ e_2 \\ e_3 \end{bmatrix} + {}^{A_i}\vec{\omega}_{A_iB_i} \times \left({}^{A_i}\vec{\omega}_{A_iB_i} \times {}^{A_i}R_{B_i} \begin{bmatrix} 0 \\ e_2 \\ e_3 \end{bmatrix} \right)$$

The vector ${}^{A_i}\vec{\alpha}_{A_iB_i}$ is then also needed:

$$(2.134) \qquad {}^{A_i}\vec{\alpha}_{A_iB_i} = \begin{bmatrix} -c_3\dot{\theta}_3\dot{\theta}_2 - s_3\ddot{\theta}_2 - s_3c_2\dot{\theta}_1\dot{\theta}_3 - c_3s_2\dot{\theta}_1\dot{\theta}_2 + c_3c_2\ddot{\theta}_1 \\ -s_3\dot{\theta}_3\dot{\theta}_2 + c_3\ddot{\theta}_2 - s_2s_3\dot{\theta}_2\dot{\theta}_1 + c_2c_3\dot{\theta}_1\dot{\theta}_3 + c_2s_3\ddot{\theta}_1 \\ \ddot{\theta}_3 - c_2\dot{\theta}_1\dot{\theta}_2 - s_2\dot{\theta}_1 \end{bmatrix}$$

To derive ${}^{B_i}\vec{\omega}_{NB_i}$, first calculate

(2.135)

$$\begin{aligned} {}^{B_i}\vec{\omega}_{A_iB_i} &= \dot{\theta}_3 {R_x}^T(\theta_1){R_y}^T(\theta_2){R_z}^T(\theta_3) \begin{bmatrix} 0 \\ 0 \\ 1 \end{bmatrix} + \dot{\theta}_2 {R_x}^T(\theta_1){R_y}^T(\theta_2) \begin{bmatrix} 0 \\ 1 \\ 0 \end{bmatrix} + \dot{\theta}_1 {R_x}^T(\theta_1) \begin{bmatrix} 1 \\ 0 \\ 0 \end{bmatrix} \\ &= \begin{bmatrix} \dot{\theta}_1 & - & \dot{\theta}_3 s_2 \\ \dot{\theta}_2 c_1 & + & \dot{\theta}_3 c_2 s_1 \\ -\dot{\theta}_2 s_1 & + & \dot{\theta}_3 c_1 c_2 \end{bmatrix} \end{aligned}$$

to get

$$(2.136) \qquad {}^{B_i}\vec{\omega}_{NB_i} = {}^{B_i}R_{A_i} \cdot {}^{A_i}\vec{\omega}_{NA_i} + {}^{B_i}\vec{\omega}_{A_iB_i}$$

Differentiating Equation 2.136 results in

(2.137)

$$
\begin{aligned}
{}^{B_i}\vec{\alpha}_{NB_i} &= -{}^{B_i}\vec{\omega}_{A_iB_i} \times \left({}^{B_i}R_{A_i} \cdot {}^{A_i}\vec{\omega}_{NA_i}\right) + {}^{B_i}R_{A_i} \cdot {}^{A_i}\vec{\alpha}_{NA_i} + {}^{B_i}\vec{\alpha}_{A_iB_i} \\
&= \begin{bmatrix}
c_2c_3\ddot{\theta}_1 - \ddot{\theta}_3 s_2 + c_2\ddot{\theta}_2 s_3 - c_1^2 c_2\dot{\theta}_3\dot{\theta}_2 - c_2\dot{\theta}_3 s_1^2\dot{\theta}_2 \\
-c_1^2 c_3\dot{\theta}_1 s_2\dot{\theta}_2 - c_3\dot{\theta}_1 s_1^2 s_2\dot{\theta}_2 - c_1^2\dot{\theta}_2 s_2 s_3\dot{\theta}_2 - \dot{\theta}_2 s_1^2 s_2 s_3\dot{\theta}_2 + c_1^2 c_2 c_3\dot{\theta}_2\dot{\theta}_3 \\
+c_2c_3\dot{\theta}_2 s_1^2\dot{\theta}_3 - c_1^2 c_2\dot{\theta}_1 s_3\dot{\theta}_3 - c_2\dot{\theta}_1 s_1^2 s_3\dot{\theta}_3 + \ddot{\theta}_1 - \ddot{\theta}_3 s_2 - \dot{\theta}_3\dot{\theta}_2 c_2 \\
\\
c_2\ddot{\theta}_3 s_1 + \ddot{\theta}_1(c_3 s_1 s_2 - c_1 s_3) + \ddot{\theta}_2(c_1 c_3 + s_1 s_2 s_3) + c_1 c_2\dot{\theta}_3\dot{\theta}_1 - c_3\dot{\theta}_2 s_1\dot{\theta}_1 \\
+c_1c_3\dot{\theta}_1 s_2\dot{\theta}_1 + \dot{\theta}_1 s_1 s_3\dot{\theta}_1 + c_1\dot{\theta}_2 s_2 s_3\dot{\theta}_1 + c_2c_3\dot{\theta}_1 s_1\dot{\theta}_2 - \dot{\theta}_3 s_1 s_2\dot{\theta}_2 + c_2\dot{\theta}_2 s_1 s_3\dot{\theta}_2 \\
-c_1c_2^2c_3\dot{\theta}_1\dot{\theta}_3 + c_3\dot{\theta}_2 s_1 s_2\dot{\theta}_3 - c_1c_3\dot{\theta}_1 s_2^2\dot{\theta}_3 - c_1c_2^2\dot{\theta}_2 s_3\dot{\theta}_3 - \dot{\theta}_1 s_1 s_2 s_3\dot{\theta}_3 - c_1\dot{\theta}_2 s_2^2 s_3\dot{\theta}_3 \\
+\ddot{\theta}_2 c_1 - \dot{\theta}_2\dot{\theta}_1 s_1 + \ddot{\theta}_3 c_2 s_1 - \dot{\theta}_3\dot{\theta}_2 s_2 s_1 + \dot{\theta}_3\dot{\theta}_1 c_2 c_1 \\
\\
c_1c_2\ddot{\theta}_3 + \ddot{\theta}_1(c_1 c_3 s_2 + s_1 s_3) + \ddot{\theta}_2(-c_3 s_1 + c_1 s_2 s_3) - c_1 c_3\dot{\theta}_2\dot{\theta}_1 - c_2\dot{\theta}_3 s_1\dot{\theta}_1 \\
-c_3\dot{\theta}_1 s_1 s_2\dot{\theta}_1 + c_1\dot{\theta}_1 s_3\dot{\theta}_1 - \dot{\theta}_2 s_1 s_2 s_3\dot{\theta}_1 + c_1c_2c_3\dot{\theta}_1\dot{\theta}_2 - c_1\dot{\theta}_3 s_2\dot{\theta}_2 + c_1c_2\dot{\theta}_2 s_3\dot{\theta}_2 \\
+c_2^2 c_3\dot{\theta}_1 s_1\dot{\theta}_3 + c_1c_3\dot{\theta}_2 s_2\dot{\theta}_3 + c_3\dot{\theta}_1 s_1 s_2^2\dot{\theta}_3 + c_2^2\dot{\theta}_2 s_1 s_3\dot{\theta}_3 - c_1\dot{\theta}_1 s_2 s_3\dot{\theta}_3 \\
+\dot{\theta}_2 s_1 s_2^2 s_3\dot{\theta}_3 - \ddot{\theta}_2 s_1 - \dot{\theta}_2\dot{\theta}_1 c_1 + \ddot{\theta}_3 c_1 c_2 - \dot{\theta}_3\dot{\theta}_1 s_1 c_2 - \dot{\theta}_3\dot{\theta}_2 c_1 s_2
\end{bmatrix}
\end{aligned}
$$

The quantities $\dot{u}_1$, $\dot{u}_2$, $\dot{u}_3$, $\dot{\theta}_1$, $\dot{\theta}_2$, and $\dot{\theta}_3$ in the equations above require representation in terms of the blade generalized speeds. To accomplish this for $\dot{u}_1$, introduce two terms: the first, ζ, is given as

(2.138)
$$
\zeta \triangleq {}^{A_i}\vec{P}_{A_iE} \cdot \begin{bmatrix} 1 \\ 0 \\ 0 \end{bmatrix}
$$

The second is $s(x,t)$, the stretch of the blade along the longitudinal axis. Figure 2.15 illustrates ζ and s.

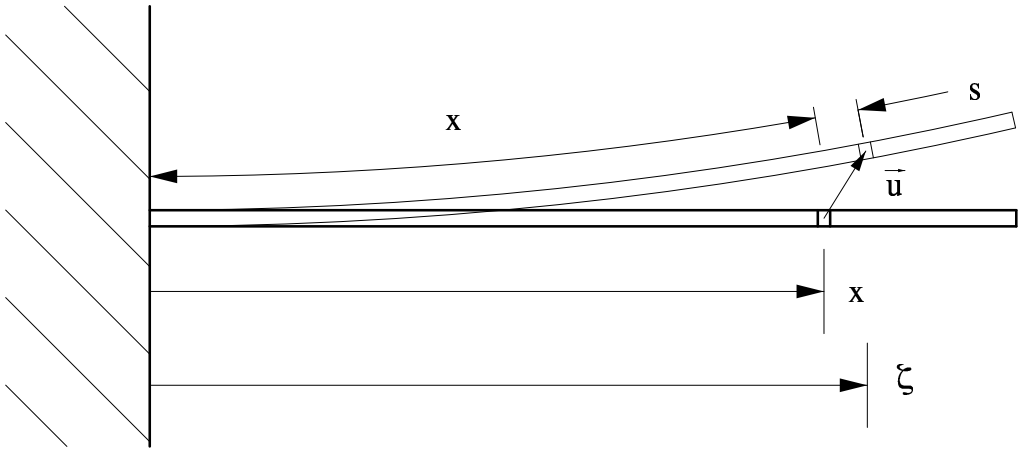


Figure 2.15: The use of ζ and s to describe stretch of a blade.

In Figure 2.15 it is shown that x and s are taken along the deformed beam [19]:

$$x + s(x,t) = \int_0^{\zeta} \left(1 + \left[\frac{\partial u_2(\sigma,t)}{\partial \sigma}\right]^2 + \left[\frac{\partial u_3(\sigma,t)}{\partial \sigma}\right]^2\right)^{1/2} d\sigma \tag{2.139}$$

To aid the remainder of the derivation, the integrand of Equation 2.139 is set to a variable:

$$J(\sigma,t) = 1 + \left[\frac{\partial u_2(\sigma,t)}{\partial \sigma}\right]^2 + \left[\frac{\partial u_3(\sigma,t)}{\partial \sigma}\right]^2$$

Using this substitution, it follows that [33]

$$\begin{aligned} \dot{s}(x,t) &= \frac{d}{dt}\int_0^{\zeta} J(\sigma,t)^{1/2} d\sigma \\ &= \int_0^{\zeta} \frac{\partial}{\partial t}\left[J(\sigma,t)^{1/2}\right] d\sigma + J(\zeta,t)^{1/2}\,\frac{d\zeta}{dt} - J(0,t)^{1/2}\,\frac{d0}{dt} \\ &= \frac{1}{2}\int_0^{\zeta} J(\sigma,t)^{-1/2}\,\frac{\partial J(\sigma,t)}{\partial t}\,d\sigma + \dot{\zeta} J(\zeta,t)^{1/2} \end{aligned} \tag{2.140}$$

Solving for $\dot{\zeta}$ and noting that $\zeta = x + u_1$,

$$\dot{u}_1 = \dot{\zeta} = \frac{\dot{s}(x,t) - \frac{1}{2}\int_0^{\zeta} J(\sigma,t)^{-1/2}\,\frac{\partial J(\sigma,t)}{\partial t}\,d\sigma}{J(\zeta,t)^{1/2}} \tag{2.141}$$

Using the assumed modes method, displacements are separated into spatial and temporal functions, with the temporal functions acting as generalized coordinates; for the case of axial displacement, lateral displacement, and twist,

$$s(x,t) = \sum_{i=1}^{\nu} \phi_{1i}(x)\, q_{1i}(t) \tag{2.142}$$

$$u_j(x,t) = \sum_{i=1}^{\nu} \phi_{ji}(x)\, q_{ji}(t), \quad j = 2,3 \tag{2.143}$$

$$\theta_1(x,t) = \sum_{i=1}^{\nu} \phi_{4i}(x)\, q_{4i}(t) \tag{2.144}$$

Due to the thinness of the material and the high blade aspect ratio, shear and rotary inertia effects are negligible; therefore, assumed modes representations for θ_2 and θ_3 bending are unnecessary. Instead, the following relations apply:

$$\theta_2(x,t) = -\frac{\partial u_3(x,t)}{\partial x} = -\sum_{i=1}^{\nu} \phi'_{3i}\, q_{3i} \tag{2.145}$$

$$\theta_3(x,t) = \frac{\partial u_2(x,t)}{\partial x} = \sum_{i=1}^{\nu} \phi'_{2i}\, q_{2i} \tag{2.146}$$

The assumed modes relations above allow an expression for $\dot{u}_1$ in generalized speeds. First,

$$\begin{aligned} \frac{\partial J(\sigma,t)}{\partial t} &= \frac{\partial}{\partial t}\left(1 + \left[\frac{\partial u_2(\sigma,t)}{\partial \sigma}\right]^2 + \left[\frac{\partial u_3(\sigma,t)}{\partial \sigma}\right]^2\right) \\ &= \frac{\partial}{\partial t}\left(1 + \left[\sum_{i=1}^{\nu} \phi'_{2i}\, q_{2i}\right]^2 + \left[\sum_{i=1}^{\nu} \phi'_{3i}\, q_{3i}\right]^2\right) \\ &= 2\sum_{i=1}^{\nu}\sum_{j=1}^{\nu}\left[\phi'_{2i}\phi'_{2j}\dot{q}_{2i}q_{2j} + \phi'_{3i}\phi'_{3j}\dot{q}_{3i}q_{3j}\right] \end{aligned} \tag{2.147}$$

Then, with Equations 2.147 and 2.142 through 2.144,

$$\dot{u}_1 = \left[J(\zeta,t)\right]^{-1/2} \sum_{i=1}^{\nu} \left\{ \phi_{1i}(x)\, \dot{q}_{1i}(t) - \sum_{j=1}^{\nu} \int_0^{\zeta} \left[J(\sigma,t)\right]^{-1/2} \left[\phi'_{2i}\phi'_{2j}\dot{q}_{2i}q_{2j} + \phi'_{3i}\phi'_{3j}\dot{q}_{3i}q_{3j}\right]\, d\sigma \right\} \tag{2.148}$$

Expressing $\dot{u}_2$, $\dot{u}_3$, $\dot{\theta}_1$, $\dot{\theta}_2$ and $\dot{\theta}_3$ in generalized coordinates follows directly from Equations 2.143 through 2.146 :

$$\dot{u}_j(x,t) = \sum_{i=1}^{\nu} \phi_{ji}(x)\,\dot{q}_{ji}(t), \quad j = 2,3 \tag{2.149}$$

$$\dot{\theta}_1(x,t) = \sum_{i=1}^{\nu} \phi_{4i}(x)\,\dot{q}_{4i}(t) \tag{2.150}$$

$$\dot{\theta}_2(x,t) = -\sum_{i=1}^{\nu} \phi'_{3i}\,\dot{q}_{3i} \tag{2.151}$$

$$\dot{\theta}_3(x,t) = \sum_{i=1}^{\nu} \phi'_{2i}\,\dot{q}_{2i} \tag{2.152}$$

At this point, the partial velocities in Equations 2.117 and 2.118 are computed and the velocities, accelerations and partial velocities are linearized in the general speeds of the core ($u_{s_1} \dots u_{s_6}$) and the blade (q_{1i}, q_{2i}, q_{3i}, q_{4i}, $i = 1, \nu$). Linearizing before reaching this stage results in the loss of some dynamic stiffness terms [19], but doing so now provides the same result as if linearization occurs at the end [18]. The linearized velocities, accelerations, and partial velocities in Equations 2.117 and 2.118 appear below.

$$\left[{}^{B_i}\vec{\omega}_{NB_i}\right]_{lin} = \begin{bmatrix} \omega_1 - \omega_3\theta_2 + \omega_2\theta_3 + \sum_{j=1}^{\nu} \phi_{4j}\dot{q}_{4j} \\ \omega_3\theta_1 - \omega_1\theta_3 + \omega_2 - \sum_{j=1}^{\nu} \phi'_{3j}\dot{q}_{3j} \\ \omega_3 + \omega_1\theta_2 - \omega_2\theta_1 + \sum_{j=1}^{\nu} \phi'_{2j}\dot{q}_{2j} \end{bmatrix} \tag{2.153}$$

$$\left[{}^{B_i}\vec{\alpha}_{NB_i}\right]_{lin} = \begin{bmatrix} \dot{\omega}_1 + \dot{\omega}_2 \sum_{j=1}^{\nu} \phi'_{2x}q_{2j} + \dot{\omega}_3 \sum_{j=1}^{\nu} \phi'_{3x}q_{3j} + \omega_2 \sum_{j=1}^{\nu} \phi'_{2j}\dot{q}_{2j} \\ +\omega_3 \sum_{j=1}^{\nu} \phi'_{3j}\dot{q}_{3j} + \sum_{j=1}^{\nu} \phi_{4j}\ddot{q}_{4j} \\ \\ \dot{\omega}_3 \sum_{j=1}^{\nu} \phi_{4j}q_{4j} - \dot{\omega}_1 \sum_{j=1}^{\nu} \phi'_{2x}q_{2j} + \dot{\omega}_2 + \omega_3 \sum_{j=1}^{\nu} \phi_{4j}\dot{q}_{4j} \\ -\omega_1 \sum_{j=1}^{\nu} \phi'_{2j}\dot{q}_{2j} - \sum_{j=1}^{\nu} \phi'_{3j}\ddot{q}_{3j} \\ \\ \dot{\omega}_3 - \dot{\omega}_1 \sum_{j=1}^{\nu} \phi'_{3x}q_{3j} - \dot{\omega}_2 \sum_{j=1}^{\nu} \phi_{4j}q_{4j} - \omega_1 \sum_{j=1}^{\nu} \phi'_{3j}\dot{q}_{3j} \\ -\omega_2 \sum_{j=1}^{\nu} \phi_{4j}\dot{q}_{4j} + \sum_{j=1}^{\nu} \phi'_{2j}\ddot{q}_{2j} \end{bmatrix} \tag{2.154}$$

$$
\begin{aligned}
(2.155)\quad \left[{}^{A_i}\ddot{\vec{P}}_{Nc}\right]_{lin} = \Bigg[& e_2\omega_1\omega_2 + e_3\dot{\omega}_2 + e_3\omega_1\omega_3 - e_2\dot{\omega}_3 - e_3\omega_1\omega_2\theta_1 + e_2\dot{\omega}_2\theta_1 + e_2\omega_1\omega_3\theta_1 \\
& + e_3\dot{\omega}_3\theta_1 - e_3\omega_2^2\theta_2 - e_3\omega_3^2\theta_2 + e_2\omega_2^2\theta_3 + e_2\omega_3^2\theta_3 + \ddot{u}_1 + \dot{v}_1 - \omega_2^2 x \\
& - \omega_3^2 x - \omega_2^2 \sum_{j=1}^{\nu} \phi_{1j} q_{1j} - \omega_3^2 \sum_{j=1}^{\nu} \phi_{1j} q_{1j} + \omega_1\omega_2 \sum_{j=1}^{\nu} \phi_{2j} q_{2j} \\
& - \dot{\omega}_3 \sum_{j=1}^{\nu} \phi_{2j} q_{2j} + \dot{\omega}_2 \sum_{j=1}^{\nu} \phi_{3j} q_{3j} + \omega_1\omega_3 \sum_{j=1}^{\nu} \phi_{3j} q_{3j} \\
& + 2\Big(-\omega_3 \sum_{j=1}^{\nu} \phi_{2j} \dot{q}_{2j} + \omega_2 \sum_{j=1}^{\nu} \phi_{3j} \dot{q}_{3j} + e_2\omega_2 \sum_{j=1}^{\nu} \phi_{4j} \dot{q}_{4j} \\
& + e_3\omega_3 \sum_{j=1}^{\nu} \phi_{4j} \dot{q}_{4j} \Big) - e_2 \sum_{j=1}^{\nu} \phi'_{2j} \ddot{q}_{2j} - e_3 \sum_{j=1}^{\nu} \phi'_{3j} \ddot{q}_{3j} \\
& \\
& - e_2\omega_1^2 - e_3\dot{\omega}_1 + e_3\omega_2\omega_3 - e_2\omega_3^2 + e_3\omega_1^2\theta_1 - e_2\dot{\omega}_1\theta_1 + e_2\omega_2\omega_3\theta_1 \\
& + e_3\omega_3^2\theta_1 + e_3\omega_1\omega_2\theta_2 + e_3\dot{\omega}_3\theta_2 - e_2\omega_1\omega_2\theta_3 - e_2\dot{\omega}_3\theta_3 + \ddot{u}_2 + \dot{v}_2 \\
& + \omega_1\omega_2 x + \dot{\omega}_3 x + \omega_1\omega_2 \sum_{j=1}^{\nu} \phi_{1j} q_{1j} + \dot{\omega}_3 \sum_{j=1}^{\nu} \phi_{1j} q_{1j} \\
& - \omega_1^2 \sum_{j=1}^{\nu} \phi_{2j} q_{2j} - \omega_3^2 \sum_{j=1}^{\nu} \phi_{2j} q_{2j} - \dot{\omega}_1 \sum_{j=1}^{\nu} \phi_{3j} q_{3j} \\
& + \omega_2\omega_3 \sum_{j=1}^{\nu} \phi_{3j} q_{3j} - e_3 \sum_{j=1}^{\nu} \phi_{4j} \ddot{q}_{4j} + 2\Big(\omega_3 \sum_{j=1}^{\nu} \phi_{1j} \dot{q}_{1j} \\
& - e_2\omega_3 \sum_{j=1}^{\nu} \phi'_{2j} \dot{q}_{2j} - \omega_1 \sum_{j=1}^{\nu} \phi_{3j} \dot{q}_{3j} - e_3\omega_3 \sum_{j=1}^{\nu} \phi'_{3j} \dot{q}_{3j} \\
& - e_2\omega_1 \sum_{j=1}^{\nu} \phi_{4j} \dot{q}_{4j} \Big) \\
& \\
& - e_3\omega_1^2 + e_2\dot{\omega}_1 - e_3\omega_2^2 + e_2\omega_2\omega_3 - e_2\omega_1^2\theta_1 - e_3\dot{\omega}_1\theta_1 - e_2\omega_2^2\theta_1 \\
& - e_3\omega_2\omega_3\theta_1 - e_3\dot{\omega}_2\theta_2 + e_3\omega_1\omega_3\theta_2 + e_2\dot{\omega}_2\theta_3 - e_2\omega_1\omega_3\theta_3 + \ddot{u}_3 + \dot{v}_3 \\
& - \dot{\omega}_2 x + \omega_1\omega_3 x - \dot{\omega}_2 \sum_{j=1}^{\nu} \phi_{1j} q_{1j} + \omega_1\omega_3 \sum_{j=1}^{\nu} \phi_{1j} q_{1j} \\
& + \dot{\omega}_1 \sum_{j=1}^{\nu} \phi_{2j} q_{2j} + \omega_2\omega_3 \sum_{j=1}^{\nu} \phi_{2j} q_{2j} - \omega_1^2 \sum_{j=1}^{\nu} \phi_{3j} q_{3j} \\
& - \omega_2^2 \sum_{j=1}^{\nu} \phi_{3j} q_{3j} + e_2 \sum_{j=1}^{\nu} \phi_{4j} \ddot{q}_{4j} + 2\Big(-\omega_2 \sum_{j=1}^{\nu} \phi_{1j} \dot{q}_{1j} \\
& + \omega_1 \sum_{j=1}^{\nu} \phi_{2j} \dot{q}_{2j} + e_2\omega_2 \sum_{j=1}^{\nu} \phi'_{2j} \dot{q}_{2j} + e_3\omega_2 \sum_{j=1}^{\nu} \phi'_{3j} \dot{q}_{3j} \\
& - e_3\omega_1 \sum_{j=1}^{\nu} \phi_{4j} \dot{q}_{4j} \Big) \Bigg]
\end{aligned}
$$

$$
(2.156)\qquad \left[\frac{\partial}{\partial u_{s1}}\left({}^{A_i}\dot{\vec{P}}_{Nc}\right) \quad \frac{\partial}{\partial u_{s2}}\left({}^{A_i}\dot{\vec{P}}_{Nc}\right) \quad \frac{\partial}{\partial u_{s3}}\left({}^{A_i}\dot{\vec{P}}_{Nc}\right)\right]_{lin}^{T} = {}^{Q}R_{A_i}
$$

$$(2.157)\quad \left[\frac{\partial}{\partial u_{s4}}\left({}^{A_i}\dot{\vec{P}}_{Nc}\right)\right]_{lin} = \begin{bmatrix} -c\theta e_3 s\gamma - c\theta e_2\theta_1 s\gamma - e_2 s\gamma s\theta + e_3\theta_1 s\gamma s\theta \\ -s\gamma s\theta \sum_{j=1}^{\nu}\phi_{2j}q_{2j} - c\theta s\gamma \sum_{j=1}^{\nu}\phi_{3j}q_{3j} \\ \\ -c\gamma e_3 - c\gamma e_2\theta_1 + \mathrm{arm}s\gamma s\theta + e_3\theta_2 s\gamma s\theta \\ -e_2\theta_3 s\gamma s\theta + s\gamma s\theta x + s\gamma s\theta \sum_{j=1}^{\nu}\phi_{1j}q_{1j} - c\gamma \sum_{j=1}^{\nu}\phi_{3j}q_{3j} \\ \\ c\gamma e_2 - c\gamma e_3\theta_1 + \mathrm{arm}c\theta s\gamma + c\theta e_3\theta_2 s\gamma \\ -c\theta e_2\theta_3 s\gamma + c\theta s\gamma x + c\theta s\gamma \sum_{j=1}^{\nu}\phi_{1j}q_{1j} + c\gamma \sum_{j=1}^{\nu}\phi_{2j}q_{2j} \end{bmatrix}$$

$$(2.158)\quad \left[\frac{\partial}{\partial u_{s5}}\left({}^{A_i}\dot{\vec{P}}_{Nc}\right)\right]_{lin} = \begin{bmatrix} c\gamma c\theta e_3 + c\gamma c\theta e_2\theta_1 + c\gamma e_2 s\theta - c\gamma e_3\theta_1 s\theta \\ +c\gamma s\theta \sum_{j=1}^{\nu}\phi_{2j}q_{2j} + c\gamma c\theta \sum_{j=1}^{\nu}\phi_{3j}q_{3j} \\ \\ -e_3 s\gamma - e_2\theta_1 s\gamma - \mathrm{arm}c\gamma s\theta - c\gamma e_3\theta_2 s\theta \\ +c\gamma e_2\theta_3 s\theta - c\gamma s\theta x - c\gamma s\theta \sum_{j=1}^{\nu}\phi_{1j}q_{1j} - s\gamma \sum_{j=1}^{\nu}\phi_{3j}q_{3j} \\ \\ -\mathrm{arm}c\gamma c\theta - c\gamma c\theta e_3\theta_2 + c\gamma c\theta e_2\theta_3 + e_2 s\gamma \\ -e_3\theta_1 s\gamma - c\gamma c\theta x - c\gamma c\theta \sum_{j=1}^{\nu}\phi_{1j}q_{1j} + s\gamma \sum_{j=1}^{\nu}\phi_{2j}q_{2j} \end{bmatrix}$$

(2.159)

$$\left[\frac{\partial}{\partial u_{s6}}\left({}^{A_i}\dot{\vec{P}}_{Nc}\right)\right]_{lin} = \begin{bmatrix} -c\theta e_2 + c\theta e_3\theta_1 + e_3 s\theta + e_2\theta_1 s\theta - c\theta \sum_{j=1}^{\nu}\phi_{2j}q_{2j} + s\theta \sum_{j=1}^{\nu}\phi_{3j}q_{3j} \\ \mathrm{arm}c\theta + c\theta e_3\theta_2 - c\theta e_2\theta_3 + c\theta x + c\theta \sum_{j=1}^{\nu}\phi_{1j}q_{1j} \\ -\mathrm{arm}s\theta - e_3\theta_2 s\theta + e_2\theta_3 s\theta - s\theta x - s\theta \sum_{j=1}^{\nu}\phi_{1j}q_{1j} \end{bmatrix}$$

$$(2.160)\qquad \left[\frac{\partial}{\partial \dot{q}_{1i}}\left({}^{A_i}\dot{\vec{P}}_{Nc}\right)\right]_{lin} = \begin{bmatrix} \phi_{1i} \\ 0 \\ 0 \end{bmatrix}$$

$$(2.161)\qquad \left[\frac{\partial}{\partial \dot{q}_{2i}}\left({}^{A_i}\dot{\vec{P}}_{Nc}\right)\right]_{lin} = \begin{bmatrix} -\sum_{j=1}^{\nu}\beta_{i,j}q_{2j} - e_2\phi'_{2i} + e_3\left(\sum_{j=1}^{\nu}\phi_{4j}q_{4j}\right)\phi'_{2i} \\ \phi_{2i} - e_2\left(\sum_{j=1}^{\nu}q_{2j}\phi_{2j}\right)\phi'_{2i} - e_3\left(\sum_{j=1}^{\nu}\phi_{3j}q_{3j}\right)\phi'_{2i} \\ 0 \end{bmatrix}$$

$$\left[\frac{\partial}{\partial \dot{q}_{3i}}\left({}^{A_i}\dot{\vec{P}}_{Nc}\right)\right]_{lin} = \begin{bmatrix} -\sum_{j=1}^{\nu}\gamma_{i,j}q_{3j} - e_3\phi'_{3i} - e_2\left(\sum_{j=1}^{\nu}\phi_{4j}q_{4j}\right)\phi'_{3i} \\ -e_3\left(\sum_{j=1}^{\nu}\phi'_{2j}q_{2j}\right)\phi'_{3i} \\ \phi_{3i} - e_3\left(\sum_{j=1}^{\nu}\phi'_{3j}q_{3j}\right)\phi'_{3i} \end{bmatrix} \tag{2.162}$$

$$\left[\frac{\partial}{\partial \dot{q}_{4i}}\left({}^{A_i}\dot{\vec{P}}_{Nc}\right)\right]_{lin} = \begin{bmatrix} e_3\phi_{4i}\sum_{j=1}^{\nu}\phi'_{2j}q_{2j} - e_2\phi_{4i}\sum_{j=1}^{\nu}\phi'_{3j}q_{3j} \\ -e_3\phi_{4i} - e_2\phi_{4i}\sum_{j=1}^{\nu}\phi_{4j}q_{4j} \\ e_2\phi_{4i} - e_3\phi_{4i}\sum_{j=1}^{\nu}\phi_{4j}q_{4j} \end{bmatrix} \tag{2.163}$$

$$\left[\frac{\partial}{\partial u_{s1}}\left({}^{B_i}\vec{\omega}_{NB_i}\right) \quad \frac{\partial}{\partial u_{s2}}\left({}^{B_i}\vec{\omega}_{NB_i}\right) \quad \frac{\partial}{\partial u_{s3}}\left({}^{B_i}\vec{\omega}_{NB_i}\right)\right]^T_{lin} = [0] \tag{2.164}$$

$$\left[\frac{\partial}{\partial u_{s4}}\left({}^{B_i}\vec{\omega}_{NB_i}\right)\right]_{lin} = \begin{bmatrix} c\gamma - c\theta s\gamma\sum_{j=1}^{\nu}\phi'_{2j}q_{2j} + s\gamma s\theta\sum_{j=1}^{\nu}\phi'_{3j}q_{3j} \\ -c\theta s\gamma + s\gamma s\theta\sum_{j=1}^{\nu}\phi_{4j}q_{4j} - c\gamma\sum_{j=1}^{\nu}\phi'_{2j}q_{2j} \\ s\gamma s\theta + c\theta s\gamma\sum_{j=1}^{\nu}\phi_{4j}q_{4j} - c\gamma\sum_{j=1}^{\nu}\phi'_{3j}q_{3j} \end{bmatrix} \tag{2.165}$$

$$\left[\frac{\partial}{\partial u_{s5}}\left({}^{B_i}\vec{\omega}_{NB_i}\right)\right]_{lin} = \begin{bmatrix} s\gamma + c\gamma c\theta\sum_{j=1}^{\nu}\phi'_{2j}q_{2j} - c\gamma s\theta\sum_{j=1}^{\nu}\phi'_{3j}q_{3j} \\ c\gamma c\theta - c\gamma s\theta\sum_{j=1}^{\nu}\phi_{4j}q_{4j} - s\gamma\sum_{j=1}^{\nu}\phi'_{2j}q_{2j} \\ -c\gamma s\theta - c\gamma c\theta\sum_{j=1}^{\nu}\phi_{4j}q_{4j} - s\gamma\sum_{j=1}^{\nu}\phi'_{3j}q_{3j} \end{bmatrix} \tag{2.166}$$

$$\left[\frac{\partial}{\partial u_{s6}}\left({}^{B_i}\vec{\omega}_{NB_i}\right)\right]_{lin} = \begin{bmatrix} s\theta\sum_{j=1}^{\nu}\phi'_{2j}q_{2j} + c\theta\sum_{j=1}^{\nu}\phi'_{3j}q_{3j} \\ s\theta + c\theta\sum_{j=1}^{\nu}\phi_{4j}q_{4j} \\ c\theta - s\theta\sum_{j=1}^{\nu}\phi_{4j}q_{4j} \end{bmatrix} \tag{2.167}$$

$$\left[\frac{\partial}{\partial \dot{q}_{1i}}\left({}^{B_i}\vec{\omega}_{NB_i}\right)\right]_{lin} = \begin{bmatrix} 0 \\ 0 \\ 0 \end{bmatrix} \tag{2.168}$$

$$\left[\frac{\partial}{\partial \dot{q}_{2i}}\left({}^{B_i}\vec{\omega}_{NB_i}\right)\right]_{lin} = \begin{bmatrix} \left(\sum_{j=1}^{\nu}\phi'_{3j}q_{3j}\right)\phi'_{2j} \\ \left(\sum_{j=1}^{\nu}\phi_{4j}q_{4j}\right)\phi'_{2j} \\ \phi'_{2j} \end{bmatrix} \tag{2.169}$$

$$\left[\frac{\partial}{\partial \dot{q}_{3i}}\left({}^{B_i}\vec{\omega}_{NB_i}\right)\right]_{lin} = \begin{bmatrix} 0 \\ -\phi'_{3j} \\ \left(\sum_{j=1}^{\nu} \phi_{4j} q_{4j}\right) \phi'_{3j} \end{bmatrix} \tag{2.170}$$

$$\left[\frac{\partial}{\partial \dot{q}_{4i}}\left({}^{B_i}\vec{\omega}_{NB_i}\right)\right]_{lin} = \begin{bmatrix} \phi_{4i} \\ 0 \\ 0 \end{bmatrix} \tag{2.171}$$

Chapter 3

Blade Behavior

The heliogyro requires that the blades pitch in a uniform fashion: in other words, as the blades pitch sinusoidally, the tip of each blade must follow the root in frequency, amplitude, and phase; the blades must be sufficiently chord-wise flat to limit twist and force vector irregularities; and blade pitch behavior must not include flap-lag-pitch or divergence instabilities. Analysis presented in this chapter depicts the degree to which this is true.

Within this chapter, the steady-state blade twist curve illustrates the effect of solar pressure, blade stress, and battens on steady-state blade twist. Data from cyclic pitch simulations correlate frequency, amplitude, and phase of twist at the blade tip with the root pitch profile. Results of a step displacement applied to collective blade root pitch reveal the amount of damping present in the particle model, as well as provide blade tip rise time, settling time, overshoot, and a transfer function between blade root pitch and tip twist if sufficient damping is present.

Simulations incorporating battens in the particle blade model illuminate a method to eliminate chord-wise curl while maintaining uniform twist. Repeat analyses of steady-state twist, tip twist vs. root pitch and step response for a blade with battens indicate their benefit.

3.1 Twist

Consider two blades pitched at a given collective pitch angle, rotating about a fixed axis. One blade rotates twice as fast as the other. As the blades twist under centripetal force, the edges stretch farther in the longitudinal direction than the centers. The stiffness of the

blade material dictates that the edge stress, and therefore, the blade twist, will be less for the slowly rotating blade. However, the analytical twist equation, 2.13, incorrectly assumes a blade of no lateral differential strain, and does not capture this phenomenon – the two blades twist the same amount.

The twist study described below utilizes the particle model, which takes into account all pertinent effects, including lateral differential strain. Blades 10 meters, 100 meters and 1000 meters long, their blade roots collectively pitched at 30 degrees, converge to equilibrium. The simulations are done twice, with solar pressure applied the second time. The blades are initially undeformed and at rest with respect to a local reference frame attached to the blade root. With each blade spinning at 2 revolutions per minute about a vertical axis, the particle blade simulator repeatedly calculates a new position of each particle and then resets velocities to zero. Periodically, the program calculates blade twist to show if equilibrium is reached.

Results in Figure 3.1 indicate that, as blade length, and therefore, blade stress, increases, twist also increases; however, none of the blades reach the same magnitude of twist as suggested by Equation 2.19. The reason is the material stiffness present in the particle model. Figure 3.1 also shows that solar pressure negligibly affects blade twist.

An anomaly appears in the results. The 1000 meter blade appears stiffer than the 100 meter blade. The problem is due to the nonlinear springs in the particle model. Figure 3.2 indicates the nonlinear stiffness factors at the blade root for the 100 m blade and the 1000 m blade spinning at 2 rpm, superimposed on the nonlinear stiffness equation for $K = 20,000$. At this operating point, the root of the 1000 m blade is stiffer than the root of the 100 m blade.

To demonstrate that blade stress is the reason behind the anomaly, the 100 meter blade is run once again to equilibrium; this time, the 100 meter blade is spun 10 times faster to make blade root stress equal to that for the 1000 meter blade. Figure 3.3 shows that the blade twist curves for the 100 meter blade spinning at 3 seconds per revolution and the 1000 meter blade spinning at 30 seconds per revolution are nearly identical. Hence, the nonlinear blade stiffness is the cause for the anomaly. For a comparison, the 100m blade twist curve for 30 seconds per revolution is included.

An added benefit from the result shown in Figure 3.3 is mesh scalability. The mesh for the 100 meter blade is more coarse with respect to the blade length than the mesh for the

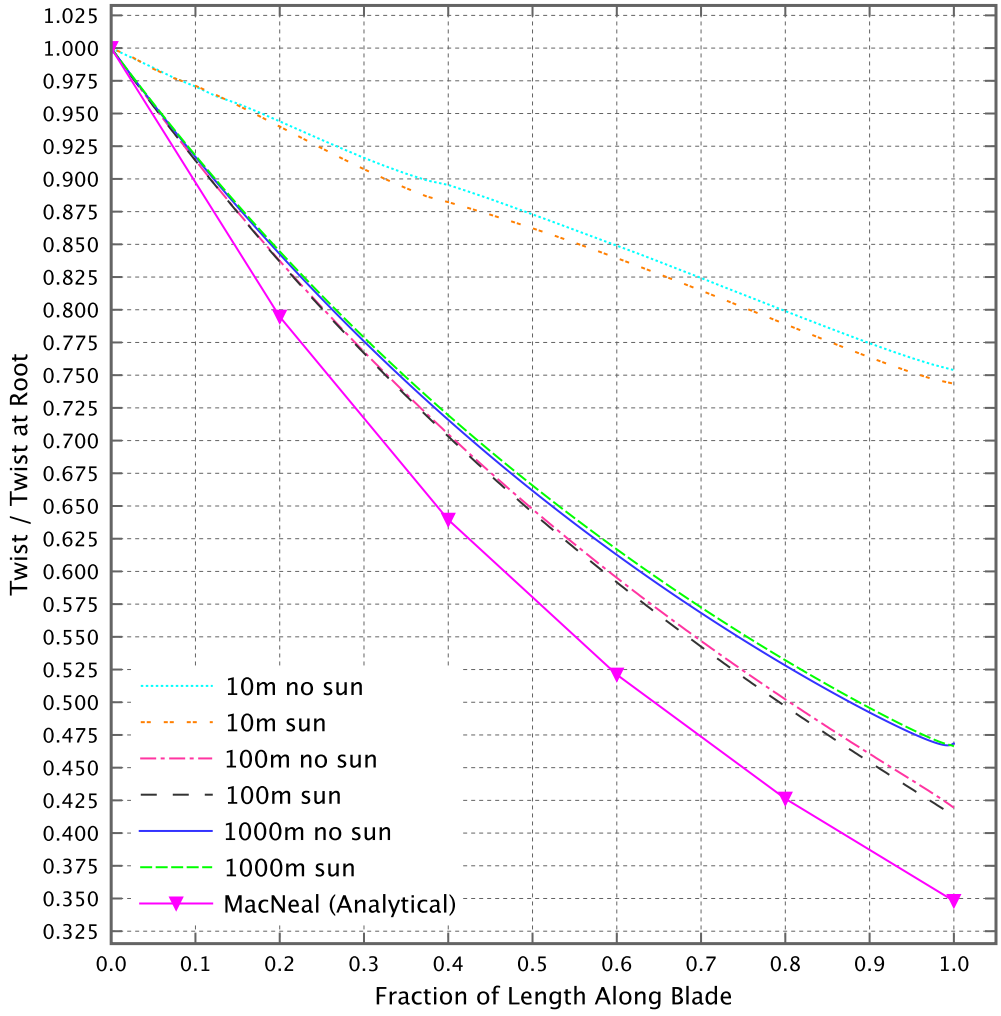


Figure 3.1: Ratio of twist to twist at root for different blade lengths, and for solar pressure present and not present. Solar pressure makes negligible difference.

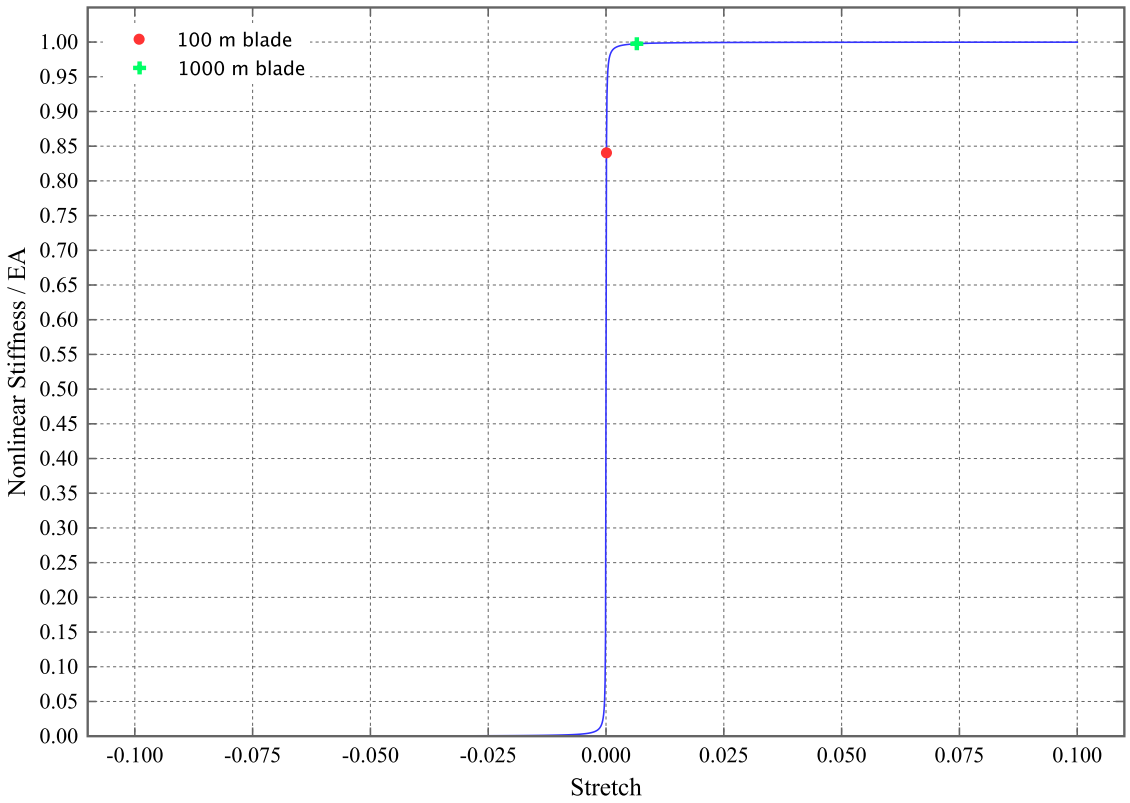


Figure 3.2: Nonlinear stiffness factors at the blade root for the 100 m and 1000 m blades spinning at 2 rpm.

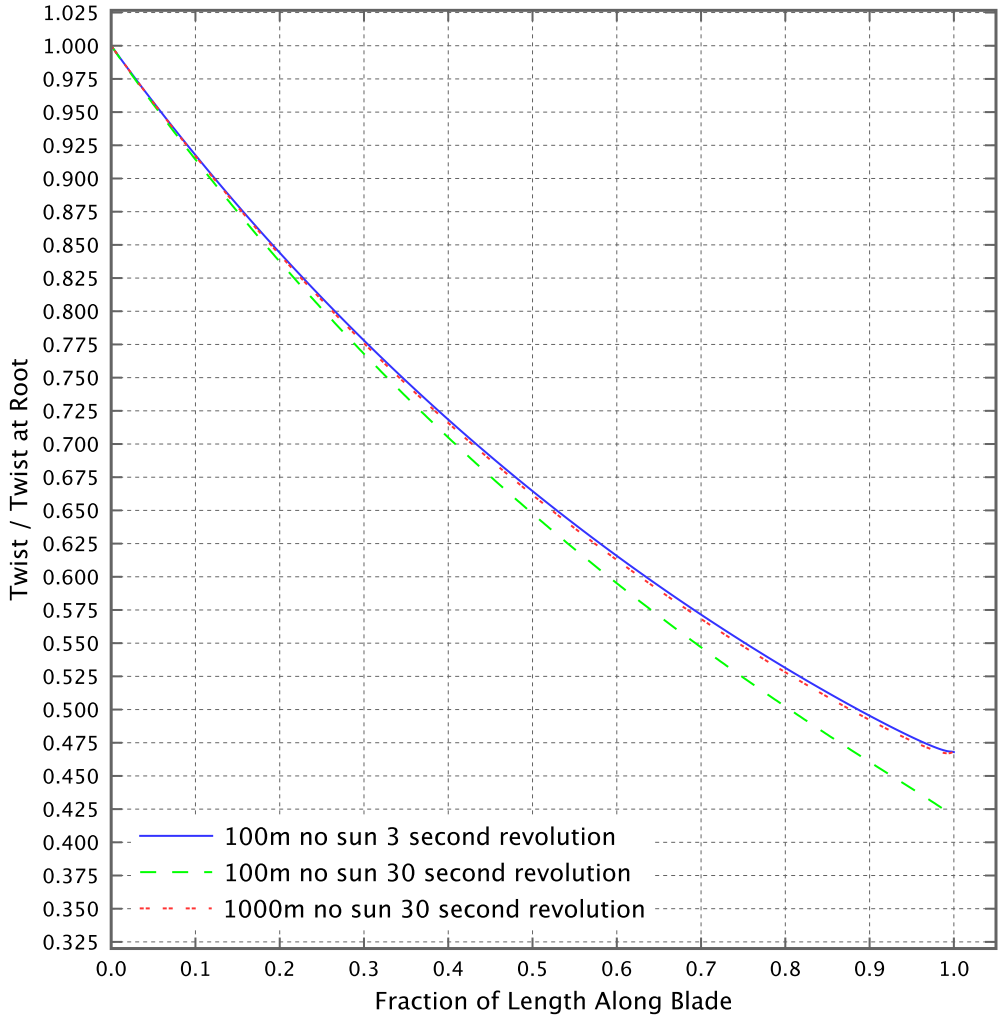


Figure 3.3: Twist curves for 100 meter and 1000 meter blades with same blade root stress. Twist curve for 100 meter blade with same spin rate as 1000 meter blade appears as a reference.

1000 meter blade, but the same twist curve occurs when the same blade stress is applied.

The blade twist study shows that the early analytical results for heliogyro blade twist failed to properly take into consideration lateral differential strain. The particle model includes this effect, which predicts twist to be less than previously considered.

3.2 Tip Pitch vs. Root Pitch

To investigate blade pitch uniformity, the same set of 10 meter, 100 meter, and 1000 meter blades are studied using the particle model. In the tests, the root of each blade transitions from a steady-state collective pitch to a constant cyclic pitch rate that is a certain fraction of the rotation rate. The pitch rate set points range from 0.2 to 1.2 times the rotation frequency. In this way, the sensitivity of blade pitch uniformity to relative pitch rate becomes evident. Due to the half-p pitch maneuver pitching the root at one half the rate of rotation, understanding tip motion at this operating point, as well as at other points other than the nominal case, is essential.

The transition profile from collective pitch to cyclic pitch consists of a pair of half-sine wave scale factors that phase in the new profile and phase out the old. An explanation and a derivation of the transition appear in Appendix A. Over two revolutions, the blade undergoes the transition, after which the blade completes 48 more revolutions, to allow transients to die out and any instabilities to manifest themselves. Allowing fifty total revolutions for instabilities to present seems reasonable, based on the only previously published stability study for heliogyro blades [31].

Another 5 revolutions provides at least one pitch cycle to compare twist at the tip with twist at the root. Due to out-of-plane flapping at the tip, twist at 90% is also compared. If the twist at 90% is similar to that at the tip, then flapping is not a concern at the given operating point.

The methodology for capturing the twist parameters entails applying sine curve fits to the twist data. To accomplish the curve fits, the Gauss-Newton method is utilized, which applies a series of linear least squares curve fits to the nonlinear curve. The sine implementation begins with the 4-parameter equation

$$\theta_{twist} = \phi_1 \cos(\phi_4 t) + \phi_2 \sin(\phi_4 t) + \phi_3 \tag{3.1}$$

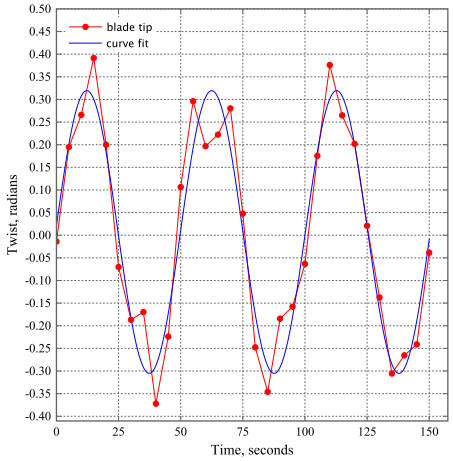
where $\phi = [\phi_1, \phi_2, \phi_3, \phi_4]$ is the parameter set, θ_{twist} is the vector of numerically generated twist angles over time t; and ϕ_0 is an initial estimate that is close enough to ϕ to ensure proper convergence. When necessary a spectral density analysis provides an initial guess for ϕ_4. Code for the sine curve fit is in Appendix C.

Often, the data indicates the presence of a secondary sinusoid superimposed over the primary. As a matter of course, each analyzed case includes the sinusoidal curve fit of the remnant, the vector of values obtained when the twist values given by the 4-parameter equation are subtracted from the simulated values. The combination of primary and secondary curve fits provides sufficient information to evaluate the uniformity of pitch.

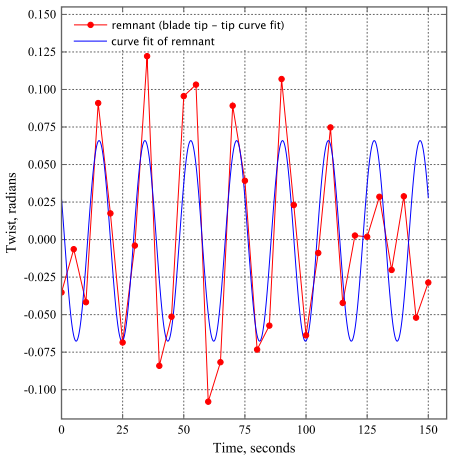
An example of curve fits calculated for this analysis appears in Figure 3.4. In it, the primary and secondary curve fits for the 1000 m blade pitching at 0.6 times the rotation rate, with solar pressure present, show the efficacy of the approach.

Figures 3.5a through 3.5f plot the comparison between the numerical results and the analytical curve presented in Figure 2.6 for tip twist vs. pitch. From the graphs, the increased stiffness in the particle model compared to the analytical model is evident for the 10m, 100m, and 1000m cases. Also, when relative pitch is equal to 1.0, all cases show a tip to root ratio greater than 1, with the primary data predicting 1.08 for the 10 m case and a range between 1.25 and 1.5 for the 100 m and 1000 m cases. The primary and secondary data combined show a range from 1.1 to 2.0. Furthermore, In all cases except for the 10m runs, the twist amplitude diverges from the expected trend for relative pitch equal to 1.2. Flutter appears to be a main cause, as the amount of divergence is markedly different at the tip compared to the point at 90% of the span. Aside from these differences, the numerical and analytical results qualitatively agree, and show no effect on twist from solar pressure.

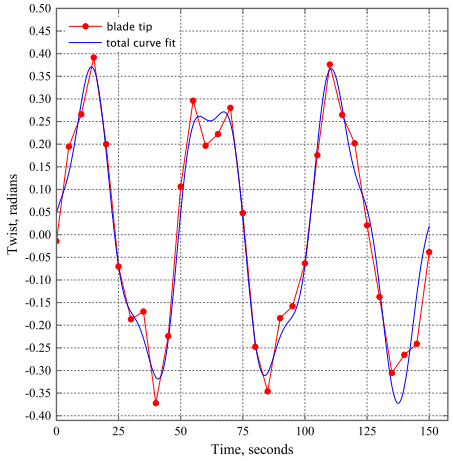
Tables 3.1 through 3.6 list pitch frequency, phase, and amplitude data for the 10 m, 100 m and 1000 m runs. The agreement in pitch frequency and phase between the root, the 90% point and the tip for the primary curve fit generally show uniformity of motion. The exceptions include phase data for the 100 m and 1000 m runs when relative pitch is equal to 1.2 and phase at the tip for the 1000 m cases when relative pitch is equal to 1.0. In correlation with the divergent amplitude, the phase differs dramatically in these cases.



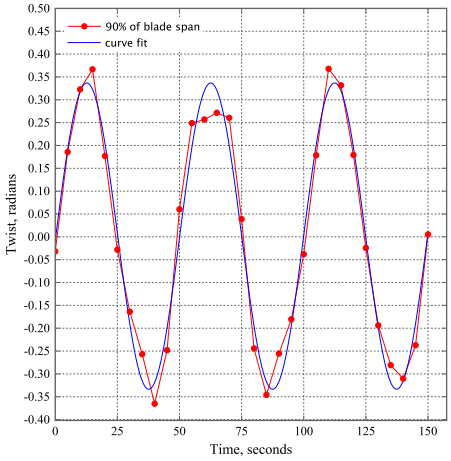
(a) fit at tip



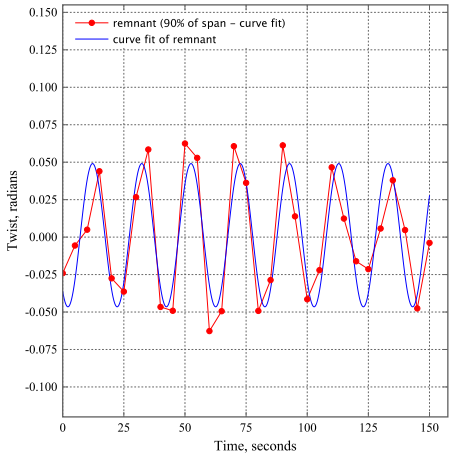
(b) fit of remnant at tip



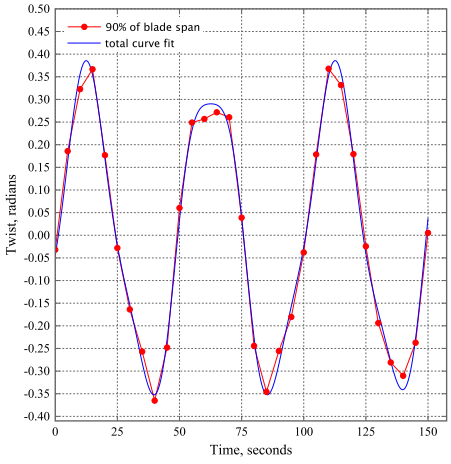
(c) combined fit at tip



(d) fit at 90% of span

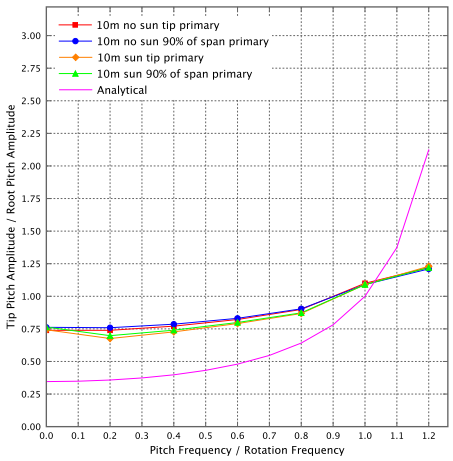


(e) fit of remnant at 90% of span

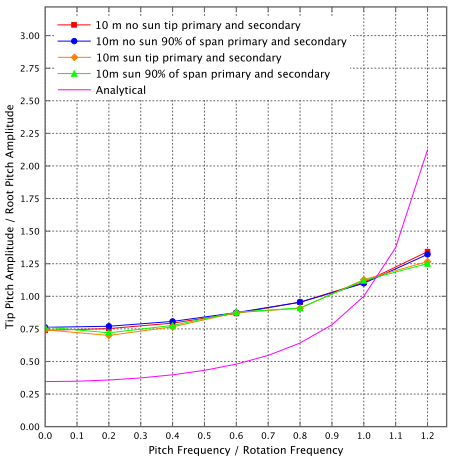


(f) combined fit at 90% of span

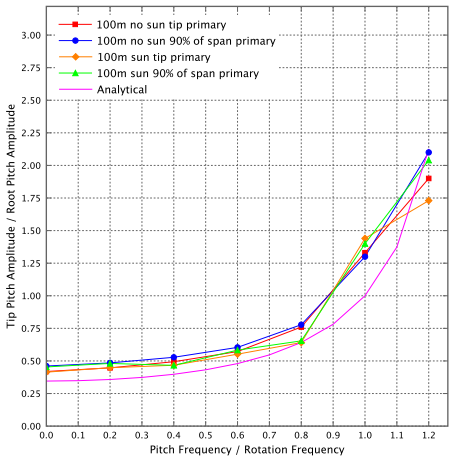
Figure 3.4: Nonlinear curve fit of twist at tip and at 90% of span for a 1000m blade, pitch rate = 0.6*rotation rate, solar pressure present. Plots a, b, and c are for the tip and d,e, and f are for the 90% point.



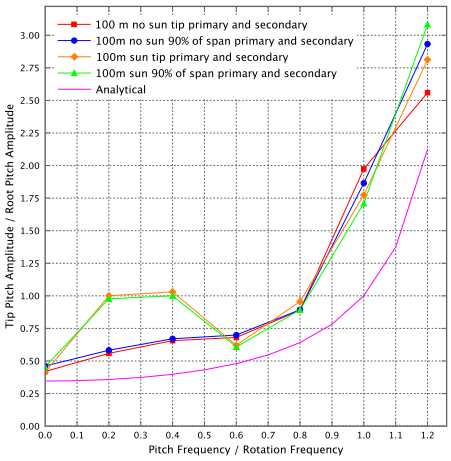
(a) 10 m blade, primary curve fit



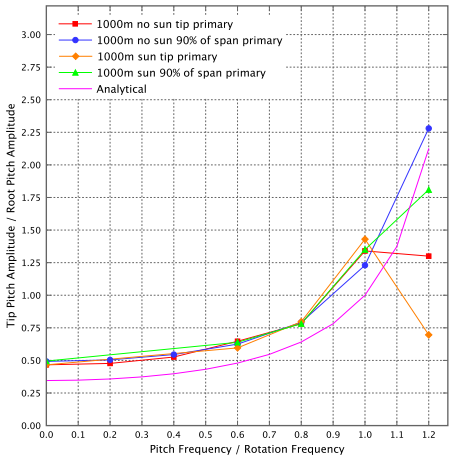
(b) 10 m blade, primary & secondary fits



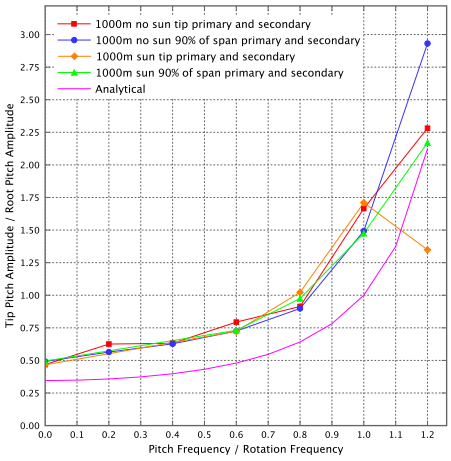
(c) 100 m blade, primary curve fit



(d) 100 m blade, primary & secondary fits



(e) 1000 m blade, primary curve fit



(f) 1000 m blade, primary & secondary fits

Figure 3.5: Ratio of tip twist amplitude to root pitch amplitude vs. ratio of root pitch frequency to heliogyro rotation frequency.

Table 3.1: Correlation of parameters ϕ between blade root, blade tip, and 90% of span for a 10 meter blade undergoing cyclic pitch and with no solar pressure present. Primary and Secondary curve fits are included.

		PRIMARY CURVE FIT			SECONDARY CURVE FIT		
Pitch Freq. Ratio		Pitch Freq. (rad/s)	Phase (rad)	Amp. Ratio w/Root	Pitch Freq. (rad/s)	Phase (rad)	Primary + Secondary Ratio
0.0	root	0.00E+00					
	tip	0.00E+00		7.39E-01			
	90%	0.00E+00		7.62E-01			
0.2	root	4.19E-02	1.57				
	tip	4.23E-02	1.59	0.739	5.35E-01	0.94	0.752
	90%	4.23E-02	1.59	0.759	5.34E-01	0.90	0.770
0.4	root	8.38E-02	1.57				
	tip	8.40E-02	1.58	0.771	4.18E-01	-1.53	0.794
	90%	8.40E-02	1.58	0.786	4.19E-01	-1.49	0.807
0.6	root	1.26E-01	1.57				
	tip	1.26E-01	1.57	0.822	3.78E-01	-1.50	0.869
	90%	1.26E-01	1.58	0.831	3.78E-01	-1.48	0.875
0.8	root	1.68E-01	1.57				
	tip	1.67E-01	1.56	0.899	5.03E-01	1.53	0.955
	90%	1.67E-01	1.56	0.904	5.03E-01	1.54	0.954
1.0	root	2.09E-01	1.57				
	tip	2.09E-01	1.57	1.097	6.30E-01	1.74	1.107
	90%	2.09E-01	1.57	1.091	6.30E-01	1.70	1.100
1.2	root	2.51E-01	1.57				
	tip	2.51E-01	1.56	1.222	5.02E-01	1.00	1.343
	90%	2.51E-01	1.56	1.209	5.01E-01	0.98	1.322

Table 3.2: Correlation of parameters ϕ between blade root, blade tip, and 90% of span for a 10 meter blade undergoing cyclic pitch and with solar pressure present. Primary and Secondary curve fits are included.

		PRIMARY CURVE FIT			SECONDARY CURVE FIT		
Pitch Freq. Ratio		Pitch Freq. (rad/s)	Phase (rad)	Amp. Ratio w/Root	Pitch Freq. (rad/s)	Phase (rad)	Primary + Secondary Ratio
0.0	root	0.00E+00					
	tip	0.00E+00		0.743			
	90%	0.00E+00		0.764			
0.2	root	4.19E-02	1.57				
	tip	4.25E-02	1.61	0.676	3.89E-01	-0.57	0.700
	90%	4.25E-02	1.61	0.698	3.89E-01	-0.56	0.720
0.4	root	8.38E-02	1.57				
	tip	8.39E-02	1.56	0.727	4.19E-01	0.52	0.766
	90%	8.39E-02	1.56	0.740	4.19E-01	0.48	0.776
0.6	root	1.26E-01	1.57				
	tip	1.26E-01	1.56	0.791	3.73E-01	-1.07	0.874
	90%	1.26E-01	1.56	0.799	3.73E-01	-1.07	0.878
0.8	root	1.68E-01	1.57				
	tip	1.67E-01	1.55	0.868	5.04E-01	1.44	0.908
	90%	1.67E-01	1.56	0.873	5.03E-01	1.41	0.910
1.0	root	2.09E-01	1.57				
	tip	2.09E-01	1.56	1.089	4.17E-01	1.84	1.128
	90%	2.09E-01	1.56	1.085	4.17E-01	1.83	1.121
1.2	root	2.51E-01	1.57				
	tip	2.51E-01	1.58	1.231	5.11E-01	1.41	1.266
	90%	2.51E-01	1.58	1.219	5.11E-01	1.41	1.251

Table 3.3: Correlation of parameters ϕ between blade root, blade tip, and 90% of span for a 100 meter blade undergoing cyclic pitch and with no solar pressure present. Primary and Secondary curve fits are included.

		PRIMARY CURVE FIT			SECONDARY CURVE FIT		
Pitch Freq. Ratio		Pitch Freq. (rad/s)	Phase (rad)	Amp. Ratio w/Root	Pitch Freq. (rad/s)	Phase (rad)	Primary + Secondary Ratio
0.0	root	0.00E+00					
	tip	0.00E+00		0.419			
	90%	0.00E+00		0.461			
0.2	root	4.19E-02	1.57				
	tip	4.21E-02	1.58	0.447	3.10E-01	2.38	0.559
	90%	4.21E-02	1.58	0.485	3.10E-01	2.37	0.582
0.4	root	8.38E-02	1.57				
	tip	8.40E-02	1.61	0.494	3.09E-01	-2.49	0.656
	90%	8.40E-02	1.61	0.528	3.09E-01	-2.50	0.670
0.6	root	1.26E-01	1.57				
	tip	1.26E-01	1.56	0.572	3.09E-01	-0.61	0.681
	90%	1.26E-01	1.57	0.604	3.09E-01	-0.63	0.699
0.8	root	1.68E-01	1.57				
	tip	1.68E-01	1.55	0.760	3.02E-01	0.37	0.889
	90%	1.68E-01	1.55	0.778	3.03E-01	0.42	0.893
1.0	root	2.09E-01	1.57				
	tip	2.08E-01	1.48	1.334	2.86E-01	-0.19	1.974
	90%	2.08E-01	1.49	1.297	2.86E-01	-0.19	1.865
1.2	root	2.51E-01	1.57				
	tip	2.51E-01	-2.53	1.901	3.00E-01	2.16	2.559
	90%	2.51E-01	-2.60	2.102	2.99E-01	2.17	2.933

Table 3.4: Correlation of parameters ϕ between blade root, blade tip, and 90% of span for a 100 meter blade undergoing cyclic pitch and with solar pressure present. Primary and Secondary curve fits are included.

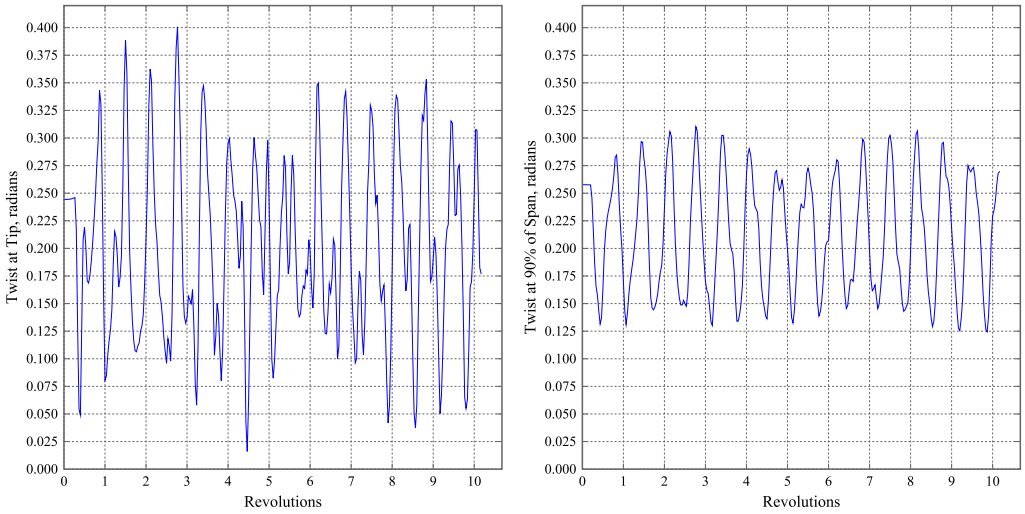
		PRIMARY CURVE FIT			SECONDARY CURVE FIT		
Pitch Freq. Ratio		Pitch Freq. (rad/s)	Phase (rad)	Amp. Ratio w/Root	Pitch Freq. (rad/s)	Phase (rad)	Primary + Secondary Ratio
0.0	root	0.00E+00					
	tip	0.00E+00		0.414			
	90%	0.00E+00		0.454			
0.2	root	4.19E-02	1.57				
	tip	4.12E-02	1.57	0.448	3.08E-01	-1.25	1.000
	90%	4.15E-02	1.60	0.481	3.08E-01	-1.25	0.978
0.4	root	8.38E-02	1.57				
	tip	8.78E-02	1.75	0.467	2.79E-01	1.61	1.031
	90%	8.75E-02	1.75	0.466	2.78E-01	1.51	1.000
0.6	root	1.26E-01	1.57				
	tip	1.26E-01	1.57	0.552	6.26E-01	2.56	0.621
	90%	1.26E-01	1.57	0.583	6.28E-01	2.71	0.608
0.8	root	1.68E-01	1.57				
	tip	1.70E-01	1.33	0.641	5.02E-01	2.99	0.956
	90%	1.70E-01	1.32	0.654	5.01E-01	2.83	0.892
1.0	root	2.09E-01	1.57				
	tip	2.09E-01	1.54	1.443	2.83E-01	2.02	1.774
	90%	2.09E-01	1.54	1.404	2.82E-01	2.00	1.710
1.2	root	2.51E-01	1.57				
	tip	2.52E-01	-2.69	1.730	7.43E-01	0.24	2.812
	90%	2.54E-01	-2.67	2.040	7.45E-01	0.34	3.084

Table 3.5: Correlation of parameters ϕ between blade root, blade tip, and 90% of span for a 1000 meter blade undergoing cyclic pitch and with no solar pressure present. Primary and Secondary curve fits are included.

		PRIMARY CURVE FIT			SECONDARY CURVE FIT		
Pitch Freq. Ratio		Pitch Freq. (rad/s)	Phase (rad)	Amp. Ratio w/Root	Pitch Freq. (rad/s)	Phase (rad)	Primary + Secondary Ratio
0.0	root	0.00E+00					
	tip	0.00E+00		0.468			
	90%	0.00E+00		0.492			
0.2	root	4.19E-02	1.57				
	tip	4.13E-02	1.52	0.477	3.69E-01	1.33	0.626
	90%	4.16E-02	1.55	0.504	3.67E-01	1.21	0.564
0.4	root	8.38E-02	1.57				
	tip	8.35E-02	1.56	0.526	3.08E-01	0.24	0.631
	90%	8.34E-02	1.54	0.545	3.10E-01	0.45	0.627
0.6	root	1.26E-01	1.57				
	tip	1.27E-01	1.59	0.647	3.62E-01	-1.65	0.794
	90%	1.26E-01	1.57	0.625	3.10E-01	2.13	0.725
0.8	root	1.68E-01	1.57				
	tip	1.67E-01	1.51	0.782	3.05E-01	-2.60	0.913
	90%	1.68E-01	1.59	0.792	3.06E-01	-2.60	0.898
1.0	root	2.09E-01	1.57				
	tip	2.11E-01	1.71	1.336	2.93E-01	0.11	1.665
	90%	2.09E-01	1.52	1.228	2.91E-01	-0.02	1.493
1.2	root	2.51E-01	1.57				
	tip	2.56E-01	2.78	1.300	3.06E-01	-1.03	2.282
	90%	2.52E-01	2.78	2.285	3.10E-01	-2.51	2.932

Table 3.6: Correlation of parameters ϕ between blade root, blade tip, and 90% of span for a 1000 meter blade undergoing cyclic pitch and with solar pressure present. Primary and Secondary curve fits are included.

		PRIMARY CURVE FIT			SECONDARY CURVE FIT		
Pitch Freq. Ratio		Pitch Freq. (rad/s)	Phase (rad)	Amp. Ratio w/Root	Pitch Freq. (rad/s)	Phase (rad)	Primary + Secondary Ratio
0.0	root	0.00E+00					
	tip	0.00E+00		0.466			
	90%	0.00E+00		0.495			
0.6	root	1.26E-01	1.57				
	tip	1.25E-01	1.53	0.596	3.35E-01	-1.14	0.724
	90%	1.26E-01	1.60	0.639	3.12E-01	-2.48	0.731
0.8	root	1.68E-01	1.57				
	tip	1.69E-01	1.61	0.797	3.04E-01	0.42	1.022
	90%	1.68E-01	1.55	0.782	3.04E-01	0.41	0.975
1.0	root	2.09E-01	1.57				
	tip	2.11E-01	1.69	1.426	3.72E-01	2.96	1.710
	90%	2.10E-01	1.55	1.351	3.72E-01	2.95	1.475
1.2	root	2.51E-01	1.58				
	tip	2.19E-01	-1.25	0.696	2.63E-01	-2.57	1.349
	90%	2.55E-01	3.01	1.813	2.16E-01	-2.39	2.171



(a) Step Response at Tip

(b) Step Response at 90% of Span

Figure 3.6: Twist response at tip and 90% along the span due to a step decrease at the root from 0.52 radians (30 degrees) to 0.44 radians (25 degrees) over one radian of rotation.

3.3 Step Response

Imparting a step input into the root of a blade in equilibrium provides an indication of damping and a check on whether energy is being lost from the model due to numerical roundoff or some other artificial source. Since a small damping coefficient is used in the particle model, the blade should continue to oscillate with little attenuation.

A blade 1000 m long and in equilibrium changes root collective pitch from 0.52 radians to 0.44 radians in 1/6th revolution. In Figures 3.6a and 3.6b, graphs of the response over the next 10 revolutions indicate damping is not evident. The results do show, however, that the twist frequency near the end of the blade is about 1.4 times the rotation frequency, which is the same frequency of the secondary twist mode for a 1000 m blade pitching at the rotation rate in Table 3.5; it is also the same frequency predicted analytically.

Twist amplitude at the tip is about twice as much as the amplitude at 90% of the span. Damping in the model will ameliorate flutter at the tip. When damping is introduced through a pitch damping mechanism the rise time, peak time, settling time, and effective damping also become tunable.

3.4 Chord-wise Blade Curl

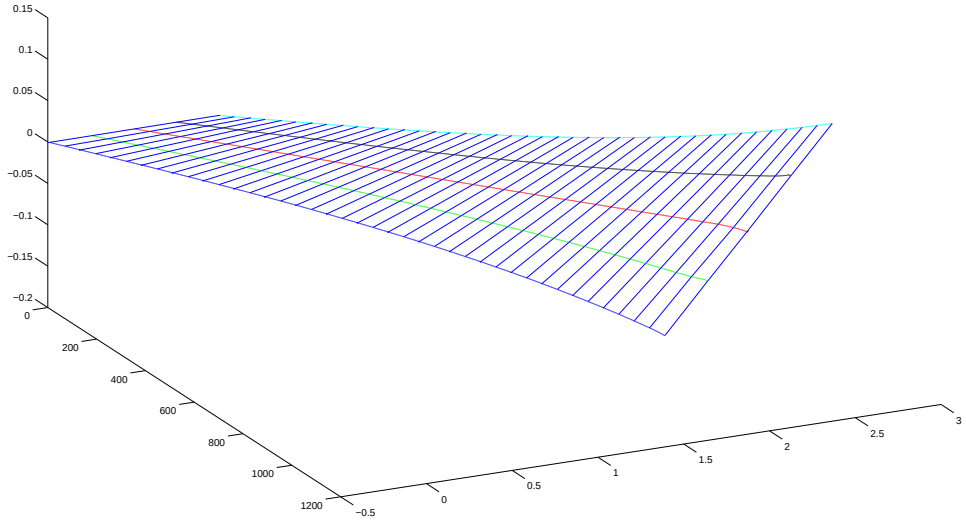
Incorporated into the particle blade model are battens that promise to reduce chord-wise curl. Spaced every 50 meters, they are the only stiffening member in the blade. Their effectiveness in creating a smooth, uniform surface becomes evident upon examination of the following simulation results.

A blade with battens transitions from a steady-state collective pitch to a constant cyclic pitch rate as described in Section 3.2. The pitch rate is equal to the rotation rate. After completing 50 revolutions, the tip-to-root relationship and a snapshot of blade shape indicate batten effectiveness.

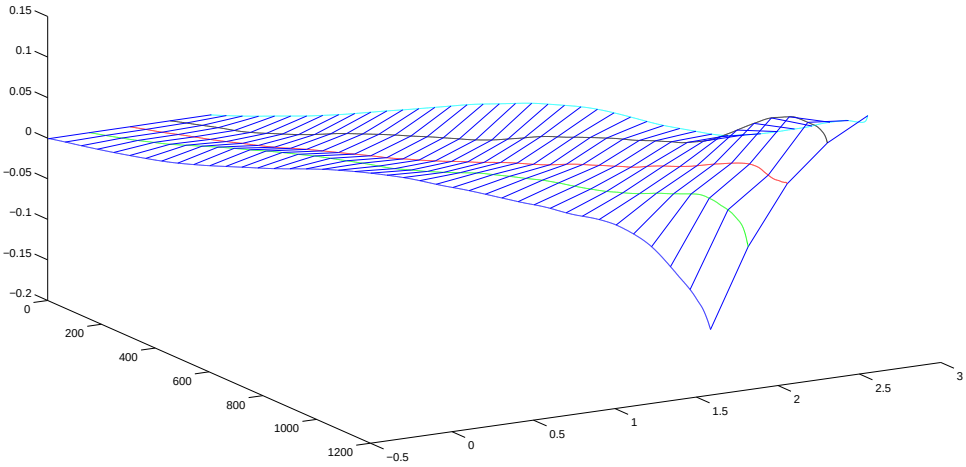
Figure 3.7 and Table 3.7 illustrate. Battens ameliorate curl and tip flutter. They straighten the shape throughout the blade. Compared to a blade without battens, the tip and 90% point along the span are uniform in pitch and phase.

Negative effects also exist. The increased weight of the blade increases root stress about 10%. The blade tip lags behind the root twice as much. The amplitude determined from primary and secondary curve fits suggest a 14% increase at the tip.

The positive effects outweigh the negative. Battens are effective at providing a uniform surface for improved heliogyro control.



(a) 1000 m blade, battens



(b) 1000 m blade, no battens

Figure 3.7: Comparison of 1000 m blades, one with battens and one without. These are snapshots of the blades after 55 rotations around a vertical axis.

Table 3.7: Comparison of parameters ϕ between blade root, blade tip, and 90% of span for a 1000 meter blade with battens spaced every 50 m and a 1000 m blade without battens. The blades are undergoing cyclic pitch; no solar pressure is present.

BATTENS

		PRIMARY CURVE FIT			SECONDARY CURVE FIT		
Pitch Freq. Ratio		Pitch Freq. (rad/s)	Phase (rad)	Amp. Ratio w/Root	Pitch Freq. (rad/s)	Phase (rad)	Primary + Secondary Ratio
0.0	root	0.00E+00					
	tip	0.00E+00		0.448			
	90%	0.00E+00		0.482			
1.0	root	2.09E-01	1.57				
	tip	2.08E-01	1.46	1.31	2.89E-01	0.18	1.900
	90%	2.08E-01	1.47	1.28	2.89E-01	0.18	1.804

NO BATTENS

		PRIMARY CURVE FIT			SECONDARY CURVE FIT		
Pitch Freq. Ratio		Pitch Freq. (rad/s)	Phase (rad)	Amp. Ratio w/Root	Pitch Freq. (rad/s)	Phase (rad)	Primary + Secondary Ratio
0.0	root	0.00E+00					
	tip	0.00E+00		0.468			
	90%	0.00E+00		0.492			
1.0	root	2.09E-01	1.57				
	tip	2.11E-01	1.71	1.336	2.93E-01	0.11	1.665
	90%	2.09E-01	1.52	1.228	2.91E-01	-0.02	1.493

Chapter 4

Pitch Control

4.1 Requirements

The four maneuvers that require blade pitch control are cyclic pitch, collective-cyclic pitch, collective pitch, and half-p pitch. Each maneuver results in a net force and/or torque being applied to the spacecraft. Using these maneuvers, the controller accepts desired force and torque values and determines the appropriate parameter settings to execute the maneuvers.

The equation for the pitch angle of a blade with conventional helicopter controls is given as

(4.1)
$$\theta_{pitch} = \theta_{cyc} \sin\left(\omega\left(t - t_0\right) + \psi_{shift} - \psi\right) + \theta_{1/2} \sin\left(\frac{1}{2}\left(\omega\left(t - t_0\right) - \frac{\pi}{2} + \psi_{shift} - \psi\right)\right) + \theta_{coll}$$

Parameters in Equation 4.1 include

$\omega =$ pitch angular velocity

$\psi =$ phase angle

$\psi_{shift} =$ phase shift for relative location of blade i, $= \frac{2\pi}{n_b}\left(i - 1\right)$

$\theta_{cyc} =$ cyclic pitch amplitude

$\theta_{coll} =$ collective pitch amplitude

$\theta_{1/2} =$ half-p pitch amplitude

$t_0 =$ initial time

Periodically, the parameters change to meet the control requirements.

The heliogyro is assumed to rotate counterclockwise along the z axis of the core, which nominally faces the Sun. The presence of a different ψ_{shift} for each blade causes all blades to act in concert on the same maneuver.

The cyclic pitch maneuver, shown in Figure 4.1, produces a steady force in the plane of the heliogyro while spin rate is maintained. The maneuver is typically used to crab perpendicular to the direction of travel. Each blade follows a sine curve centered at the origin.

The collective-cyclic pitch maneuver produces a steady rolling moment and spin torque, as illustrated in Figure 4.2. Collective-cyclic pitch precesses the spin vector to maintain a lock on the Sun and to maximize thrust. The pitch profile for this maneuver consists of a sine curve offset from the origin. The vertical components of pressure at the start of and half-way through the profile are equal, whereas the vertical component at the 3/4 point is greater than that at the 1/4 point. Hence, a precessional moment is created. Due to the presence of collective pitch, the spin rate changes with this maneuver. Periodically reversing both the collective and cyclic pitch angles regulates spin rate and maintains the same rolling moment.

The collective pitch maneuver, shown in Figure 4.3, produces spin torque and regulates the component of force normal to the heliogyro plane by diverting part of the solar pressure force into changing the spin rate. This maneuver is particularly useful in controlling the distance of the heliogyro from the sun while hovering at an artificial Lagrange point.

The half-p pitch maneuver, shown in Figure 4.4, is similar to the collective-cyclic pitch, but has a zero net collective pitch component, and maintains a constant spin rate. The blades pitch sinusoidally over a period of two revolutions. The half-p is the preferred maneuver for controlling heliogyro orientation.

Every two revolutions, the blade pitch controller receives the settings for a collective, cyclic, or half-p pitch maneuver and transitions from the old settings to the new. The transition profile from one maneuver to the next consists of a pair of half-sine wave scale factors that phase in the new profile and phase out the old. Appendix A shows how this is done.

Results from the blade behavior section show that the primary, dominant mode of blade tip twist reasonably follows blade root pitch, as is required for proper heliogyro operation.

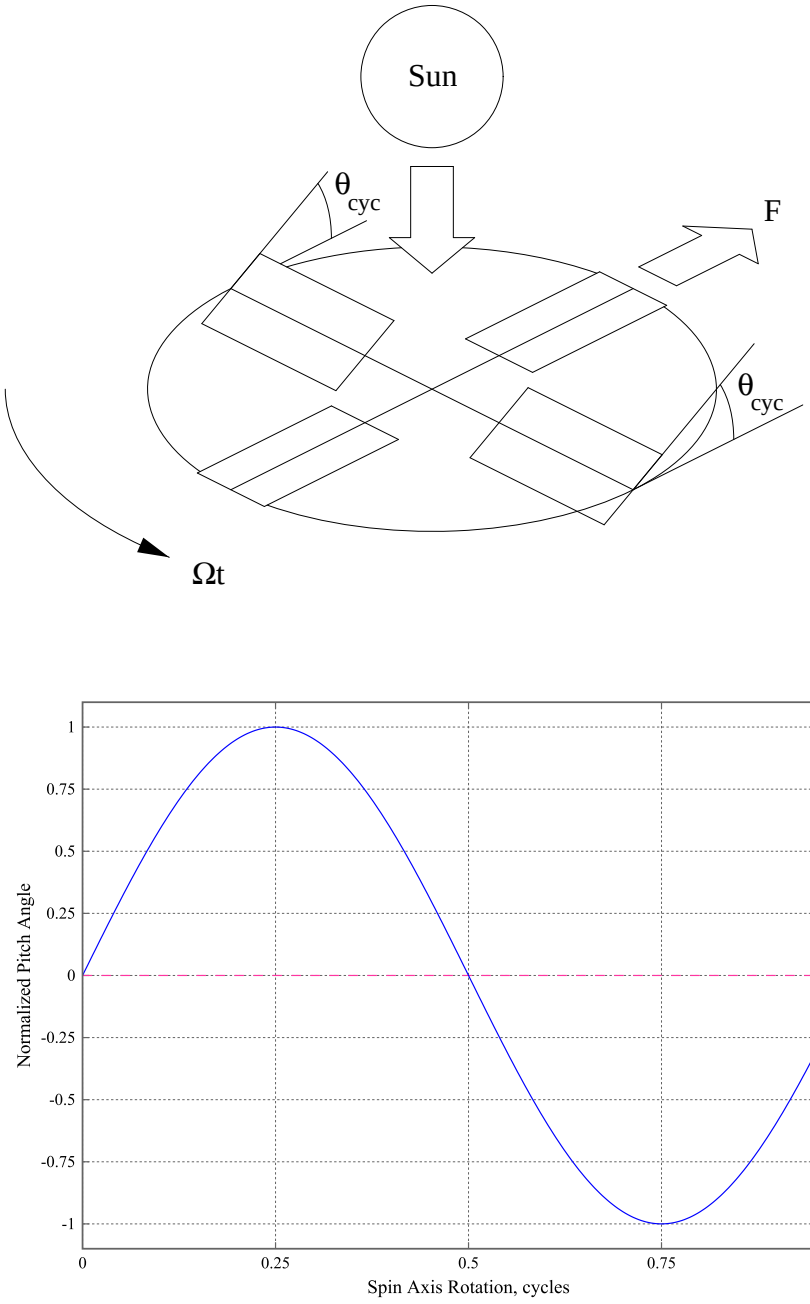


Figure 4.1: Cyclic Pitch Maneuver. [21]

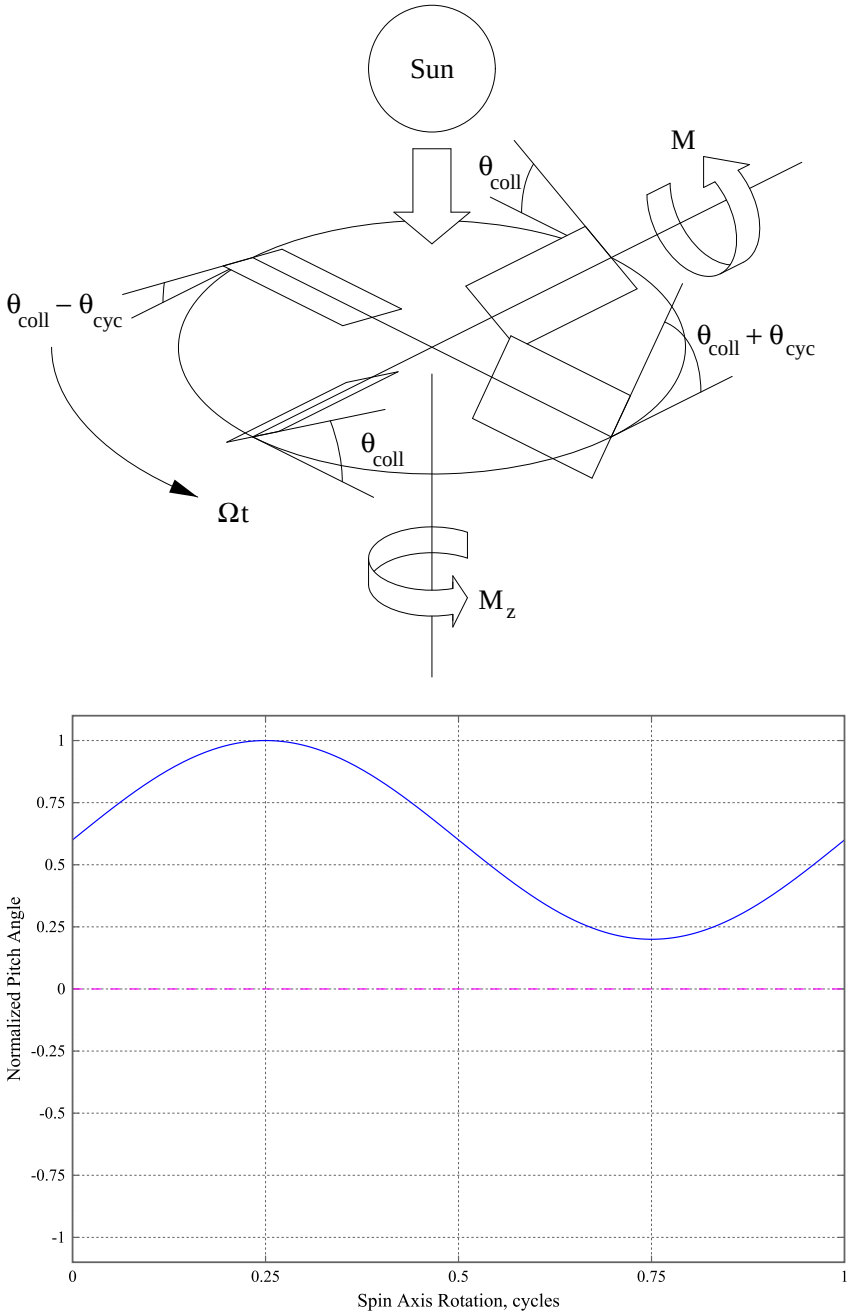


Figure 4.2: Collective-cyclic Pitch Maneuver. [21]

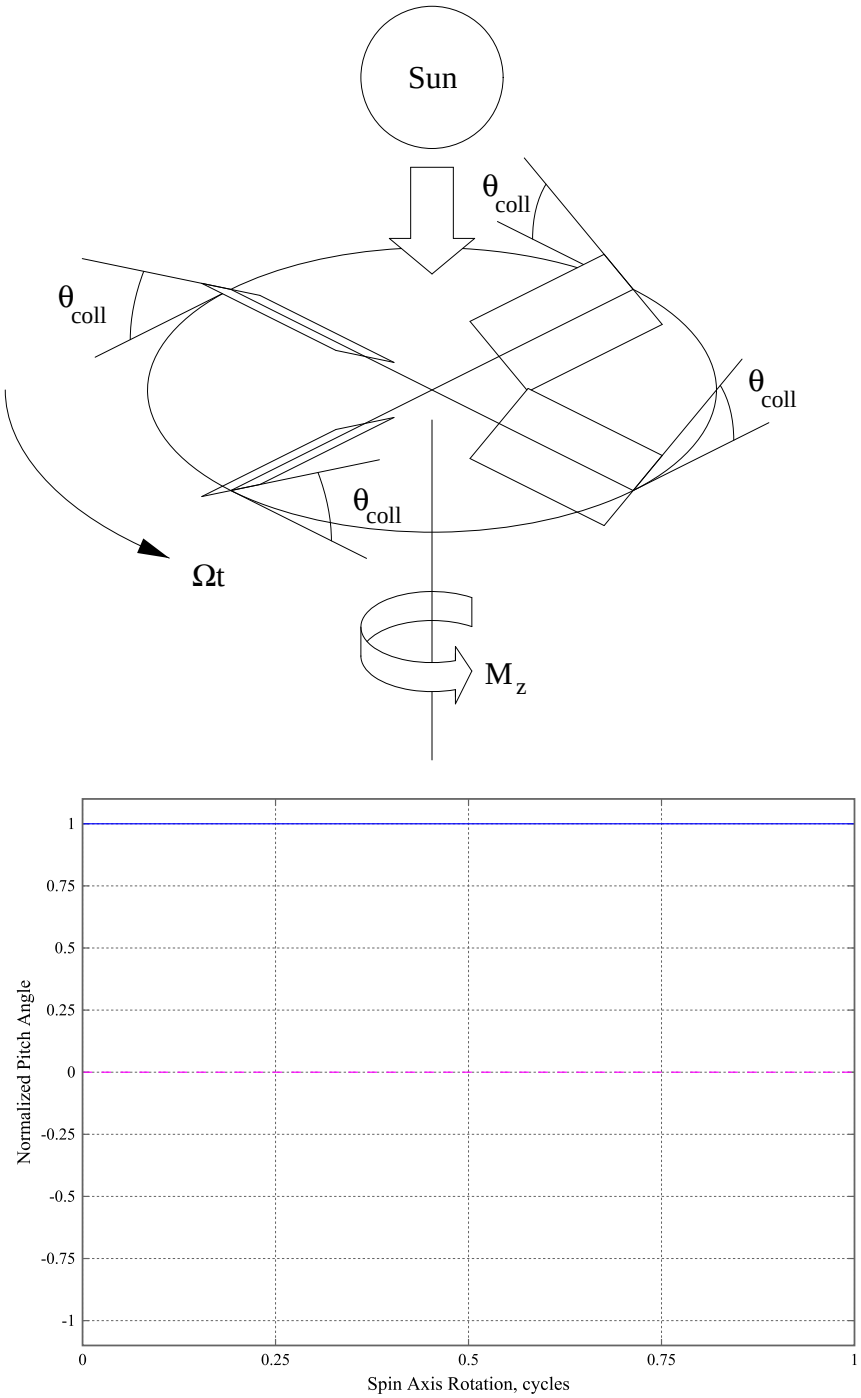


Figure 4.3: Collective Pitch Maneuver. [21]

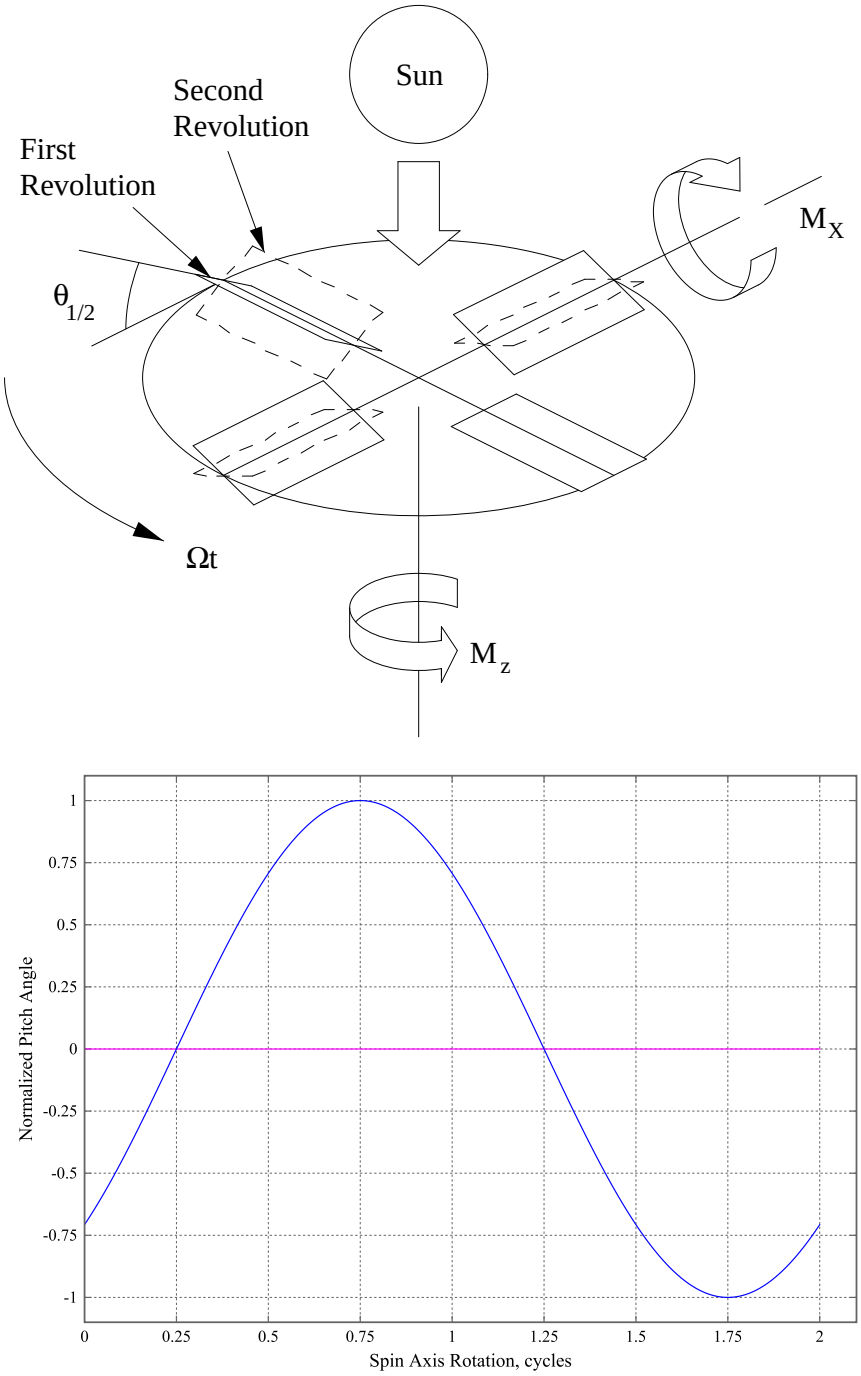


Figure 4.4: Half-P Pitch maneuver. [21]

However, when the ratio of pitch frequency to heliogyro spin rate is greater than 1.0, effects of secondary and tertiary modes significantly degrade tip behavior. Even at a ratio of 1.0, the nominal operating point, the amplitude is larger than expected and unwanted vibrations are noticeable. The need arises for a controller that dampens the unwanted modes and keeps the amplitude of dominant modes in check.

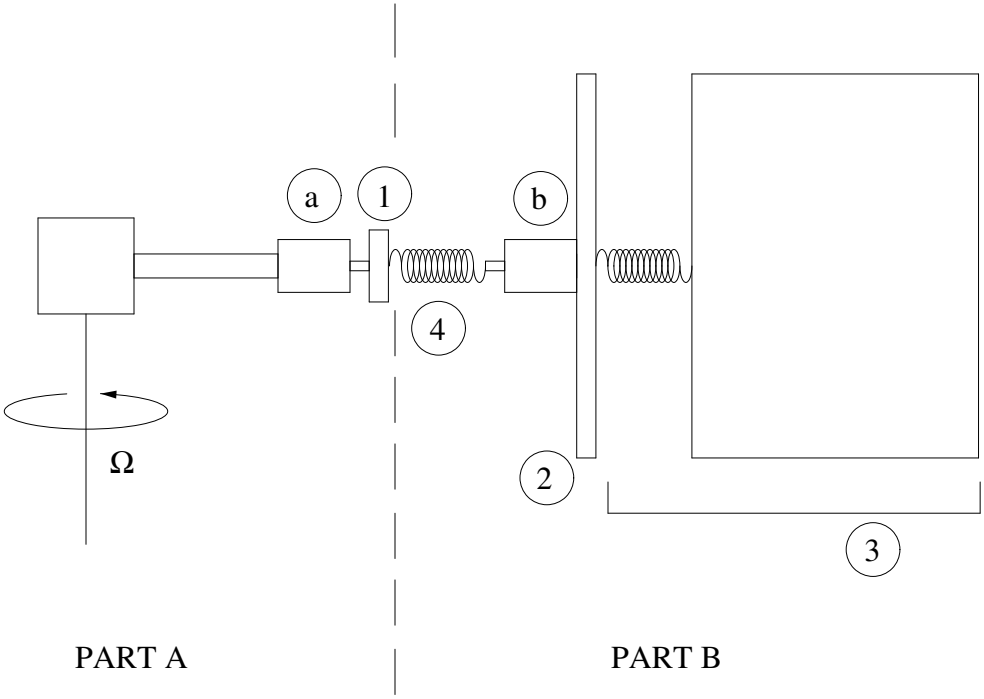
4.2 Design and Analysis

In devising a blade pitch controller, the goal is to minimize the difference between blade tip twist and blade root pitch while the blade root holder tracks the reference pitch profile. The main barriers to meeting this goal are due to the gossamer characteristics of the sail. The force required to pitch is on the order of 1 mN-m, which is less than friction forces in the pitch actuators. Detecting harmonic disturbances this small calls for delicate electromechanics. Sensors placed at the blade tip to measure blade twist are too heavy and remote to allow reliable indication, and are therefore not an option. Sensing collocated with the blade pitch actuator is the best choice.

Blade damping concerns can be addressed by a dual actuator arrangement as depicted in Figure 4.5. The main actuator follows the blade pitch profile; the secondary actuator works as an active eddy current damper, in series with a spiral clock spring, to attenuate unwanted blade twist frequencies. In the steady state, the secondary actuator follows the output of the main actuator, bringing the blade into phase with the blade root pitch profile.

The main actuator consists of a gear motor attached at its base to the core/arm assembly, as illustrated in the top half of Figure 4.6. The gear ratio is sufficient to prevent backdriving, but low enough to enable rapid response to changing position commands. The gear motor drives a coupler to which the remainder of the controller mechanism attaches.

Connected in series with the actuator is a torsional watch spring, the secondary actuator and the blade root holder. The torsional frequency of the spring and blade root holder is tuned to match the frequency of the second torsional mode of the blade. The secondary motor drives the blade root holder to follow the output of the main actuator. Impedance matching maximizes the disturbance to the spring from the blade secondary twist mode. As the disturbance is canceled, the secondary mode is dampened. A schematic in the bottom half of Figure 4.6 shows the secondary actuator.



1. Coupler.
2. Blade Root Holder.
3. Blade
4. Spiral Spring.

a. Main Actuator (gear motor).
b. Secondary Actuator.

Figure 4.5: Diagram of pitch controller.

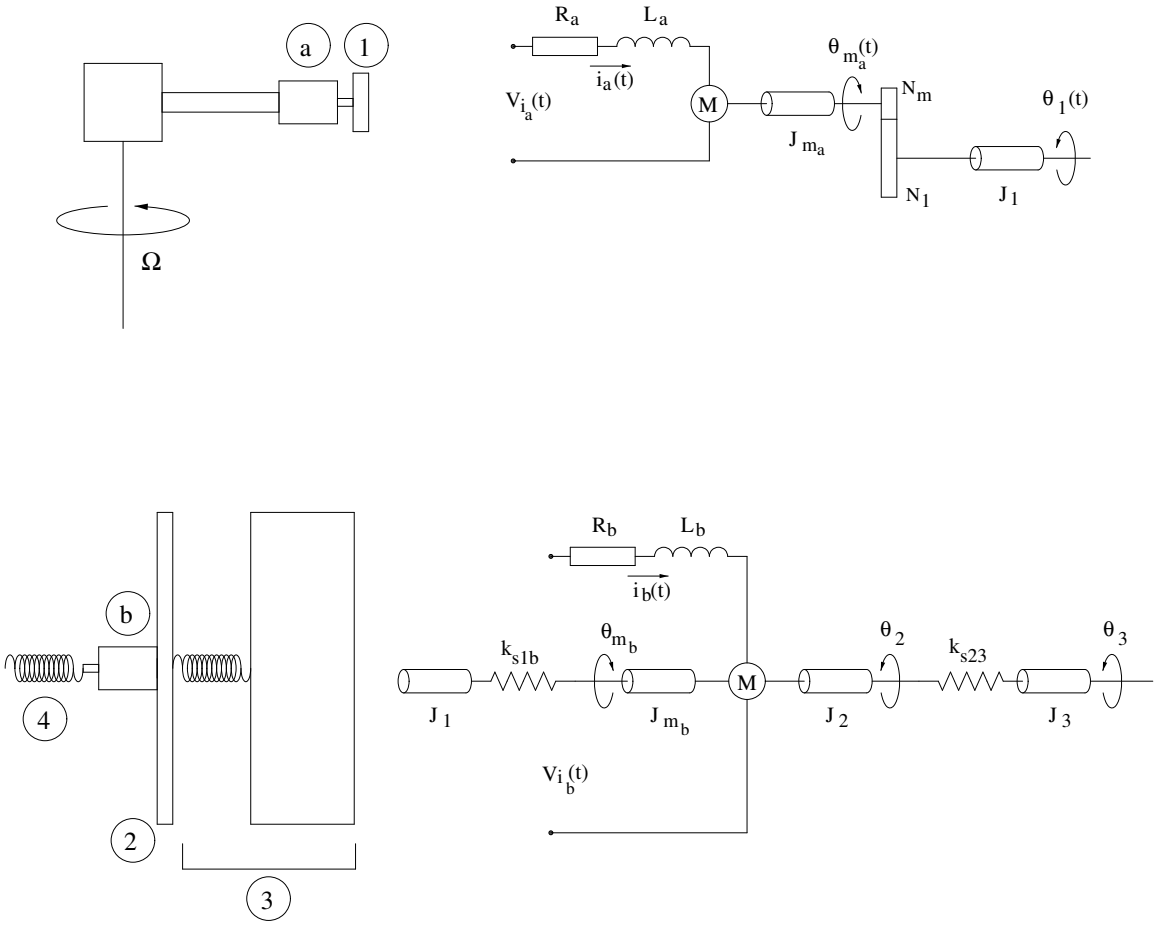


Figure 4.6: Model diagram of pitch controller. Main actuator is above, secondary is below.

Given the proper spring stiffness and motor parameters, the dual actuator system is sufficiently sensitive to secondary frequencies. The design provides redundancy, damping, and a physical indication of blade tip motion with respect to the root. Another benefit of the two actuator arrangement is that pole placement flexibility for the control system is increased. Implementation of feedback control proceeds as follows.

Referring to Figure 4.6, the governing equations for parts A and B of the pitch controller are

$$\begin{bmatrix} \dot{\theta}_1 \\ \ddot{\theta}_1 \\ \dot{i}_a \end{bmatrix} = \begin{bmatrix} 0 & 1 & 0 \\ \frac{-k_{s1b}}{J_{1eq}} & \frac{-B_{aeq}}{J_{1eq}} & \frac{n_a \eta_a k_a}{J_{1eq}} \\ 0 & -\frac{k_a}{L_a} & \frac{-R_a}{L_a} \end{bmatrix} \begin{bmatrix} \theta_1 \\ \dot{\theta}_1 \\ i_a \end{bmatrix} + \begin{bmatrix} 0 \\ 0 \\ \frac{1}{L_a} \end{bmatrix} V_{i_a} + \begin{bmatrix} 0 \\ \frac{k_{s1b}}{J_{eq}} \\ 0 \end{bmatrix} \theta_b \tag{4.2}$$

$$y = \begin{bmatrix} 1 & 0 & 0 \end{bmatrix} \begin{bmatrix} \theta_1 \\ \dot{\theta}_1 \\ i_a \end{bmatrix}$$

$$\begin{bmatrix} \dot{\theta}_b \\ \ddot{\theta}_b \\ \dot{i}_b \\ \dot{\theta}_2 \\ \ddot{\theta}_2 \\ \dot{\theta}_3 \\ \ddot{\theta}_3 \end{bmatrix} = \begin{bmatrix} 0 & 1 & 0 & 0 & 0 & 0 & 0 \\ \frac{-k_{s1b}}{J_{beq}} & \frac{-B_{beq}}{J_{beq}} & \frac{n_b \eta_b k_b}{J_{beq}} & 0 & 0 & 0 & 0 \\ 0 & -\frac{k_b}{L_b} & \frac{-R_b}{L_b} & 0 & \frac{-k_b}{L_b} & 0 & 0 \\ 0 & 0 & 0 & 0 & 1 & 0 & 0 \\ 0 & 0 & \frac{\eta_b k_b}{J_2} & -J_2\Omega^2 - \frac{k_{s23}}{J_2} & \frac{-B_2}{J_{2x}} & \frac{k_{s23}}{J_2} & 0 \\ 0 & 0 & 0 & 0 & 0 & 0 & 1 \\ 0 & 0 & 0 & \frac{k_{s23}}{J_3} & 0 & -J_3\Omega^2 - \frac{k_{s23}}{J_3} & 0 \end{bmatrix} \begin{bmatrix} \theta_b \\ \dot{\theta}_b \\ i_b \\ \theta_2 \\ \dot{\theta}_2 \\ \theta_3 \\ \dot{\theta}_3 \end{bmatrix} + \begin{bmatrix} 0 \\ 0 \\ \frac{1}{L_b} \\ 0 \\ 0 \\ 0 \\ 0 \end{bmatrix} V_{i_b} + \begin{bmatrix} 0 \\ \frac{k_{s1b}}{J_{beq}} \\ 0 \\ 0 \\ 0 \\ 0 \\ 0 \end{bmatrix} \theta_b \tag{4.3}$$

$$y = \begin{bmatrix} 0 & 0 & 0 & 1 & 0 & 0 & 0 \end{bmatrix} \begin{bmatrix} \theta_b \\ \dot{\theta}_b \\ i_b \\ \theta_2 \\ \dot{\theta}_2 \\ \theta_3 \\ \dot{\theta}_3 \end{bmatrix}$$

In the common nomenclature of feedback control theory, Equations 4.2 and 4.3 are in the state-space form $\dot{x} = Ax + bu, y = Cx$.

Integral control provides tracking of the pitch profile. Except in collective pitch, the reference is sinusoidal. For robustness, an internal model in the form

$$\ddot{r} = -\omega^2 r \tag{4.4}$$

is incorporated. Introducing tracking error, $e = y - r$, Equation 4.4 becomes

$$\begin{aligned} \ddot{e} + \omega^2 e &= \ddot{y} + \omega^2 y \\ &= C\ddot{x} + \omega C x \end{aligned} \tag{4.5}$$

Defining $\xi = \ddot{x} + \omega^2 x$ and $\mu = \ddot{u} + \omega^2 u$, e is folded into the state space equations:

$$\begin{bmatrix} \dot{e} \\ \ddot{e} \\ \dot{\xi} \end{bmatrix} = \begin{bmatrix} 0 & 1 & 0 \\ -\omega^2 & 0 & C \\ 0 & 0 & A \end{bmatrix} \begin{bmatrix} e \\ \dot{e} \\ \xi \end{bmatrix} + \begin{bmatrix} 0 \\ 0 \\ B \end{bmatrix} \mu \tag{4.6}$$

Equation 4.10 is in the state-space form $\dot{z} = Fz + G\mu$. Pole placement techniques provide the row vector $K = \left[K_2, K_1, \vec{K_0}\right]$ for the control law

$$\mu = -K_2 e - K_1 \dot{e} - K_0 \xi \tag{4.7}$$

that give the closed loop equation

$$\dot{z} = (F - GK)\, z \tag{4.8}$$

An alternate form extracts the reference input. Introducing two variables x_2 and x_1 and substituting the A matrix from Equation 4.2, Equation 4.7 can be written in the augmented form

$$\begin{aligned} \dot{x}_a &= A_a x_a + B_r r \\ y &= C_a x_a \end{aligned} \tag{4.9}$$

or

$$
\begin{bmatrix} \dot{x}_2 \\ \dot{x}_1 \\ \dot{\theta}_1 \\ \ddot{\theta}_1 \\ \dot{i}_a \end{bmatrix} = \begin{bmatrix} 0 & 1 & -K_1 & 0 & 0 \\ -\omega_a^2 & 0 & -K_2 & 0 & 0 \\ 0 & 0 & 0 & 1 & 0 \\ 0 & 0 & 0 & \frac{-B_{aeq}}{J_{1eq}} & \frac{n_a \eta_a k_a}{J_{1eq}} \\ 0 & 0 & 0 & -\frac{k_a}{L_a} & \frac{-R_a}{L_a} \end{bmatrix} \begin{bmatrix} x_2 \\ x_1 \\ \theta_1 \\ \dot{\theta}_1 \\ i_a \end{bmatrix} + \begin{bmatrix} K_1 \\ K_2 \\ 0 \\ 0 \\ 0 \end{bmatrix} r \tag{4.10}
$$

$$
y = \begin{bmatrix} 0 & 0 & 1 & 0 & 0 \end{bmatrix} \begin{bmatrix} x_2 \\ x_1 \\ \theta_1 \\ \dot{\theta}_1 \\ i_a \end{bmatrix}
$$

For closed loop response,

$$
K_c = \begin{bmatrix} -1 & 0 & \vec{K}_0 \end{bmatrix} \tag{4.11}
$$

$$
\dot{x}_a = (A_a - B_a K_c)\, x_a + B_r r \tag{4.12}
$$

$$
\theta_1 = C_a x_a \tag{4.13}
$$

where

$$
B_a = \begin{bmatrix} 0 \\ 0 \\ 0 \\ 0 \\ \frac{1}{L_a} \end{bmatrix} \tag{4.14}
$$

Obtaining the closed-loop system for part B of the pitch controller is similar.

Analysis of the two subsystems results in the responses shown in Figure 4.7 to a sine input. For purposes of illustration, certain motor characteristics from a particular motor are used in the development of the pitch controller. The relevant motor characteristics and the spring constant for the spiral spring appear in Table 4.1.

The K row vector for the entire pitch controller is a combination of the vectors K_A and K_B obtained from the separate analyses of parts A and B. It is applied to the entire system of equations similar to Equations 4.9 through 4.14.

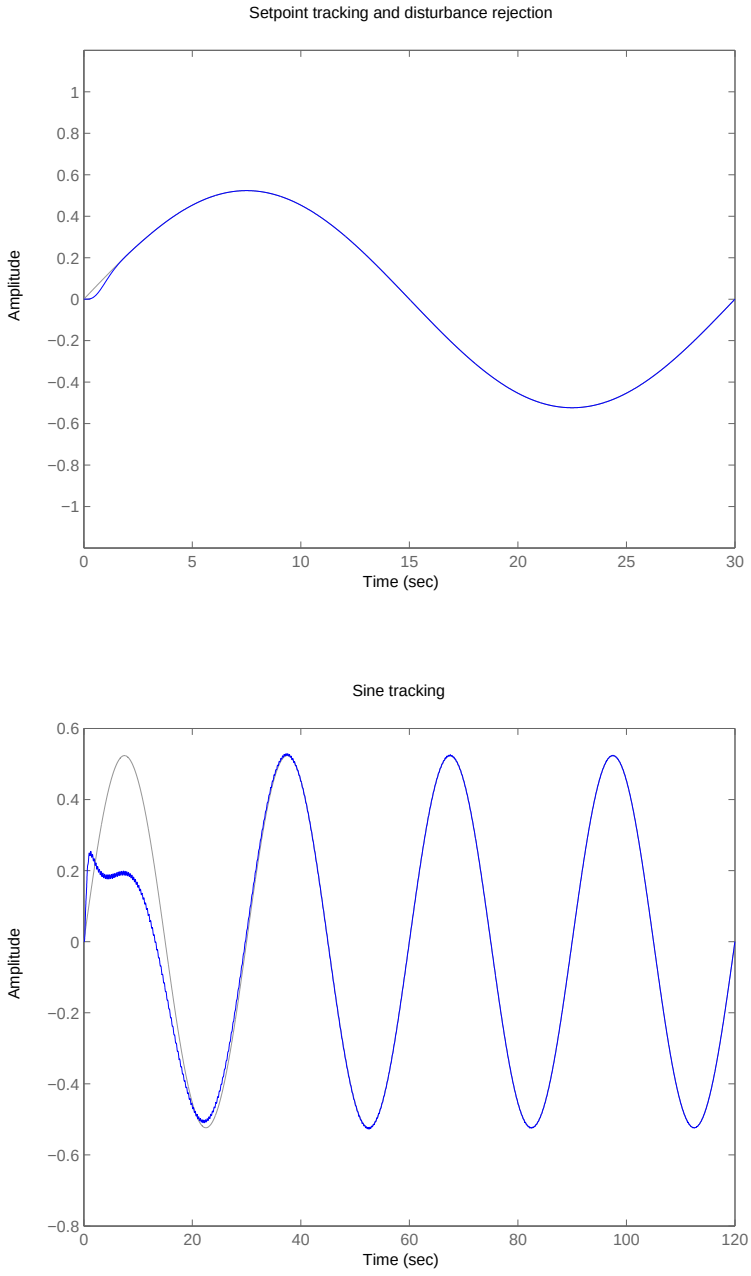


Figure 4.7: Tracking of the main actuator (top) and the secondary actuator (bottom) to a sinusoidal reference.

Table 4.1: Viable motor characteristics.

Parameter	Symbol	Value
Motor Voltage Constant, V-s/rad	k	0.04377
Armature Resistance, Ω	R	7.55
Armature Inductance, mH	L	0.83
Motor Efficiency		0.84
Actuator Efficiency,		0.75
Gearbox Ratio,part A		10
Gearbox Ratio,part b		1
Armature Frictional Coefficient, N-m s/rad	B	0.00025
Armature Inertia, kgm^2	J	$0.103e-05$
Spiral Spring Constant, N m/rad	k_s, k_s	0.0307

(Maxon RE025-055-38EAA200A)

The block diagram in Figure 4.8 shows the control strategy for the main actuator. The two subsystems have separate reference inputs. Since the goal of the controller is to have the blade track the input, the reference inputs are chosen to be equal. Furthermore, the internal model constant ω requires monitoring. In collective pitch mode, the blades do not pitch. The presence of ω causes a constant steady-state offset. In this case, ω_A and ω_B are set to 0. In all other cases, when new pitch parameters are chosen, ω takes on the new z axis component of heliogyro angular velocity.

4.3 Implementation

To the pitch controller in heliogyro simulations, the governing controller equations are incorporated into the stiff-blade model. Included also are a triple rotary joint configuration equivalent to a spherical joint. The first rotary joint aligns with the z axis of the heliogyro core and enables in-plane rotation. The second rotary joint lies along the y axis and provides vertical blade rotation. The third coincides with the longitudinal axis of the blade and allows blade twist. The first two rotary joints have accompanying spring dampers. Between the

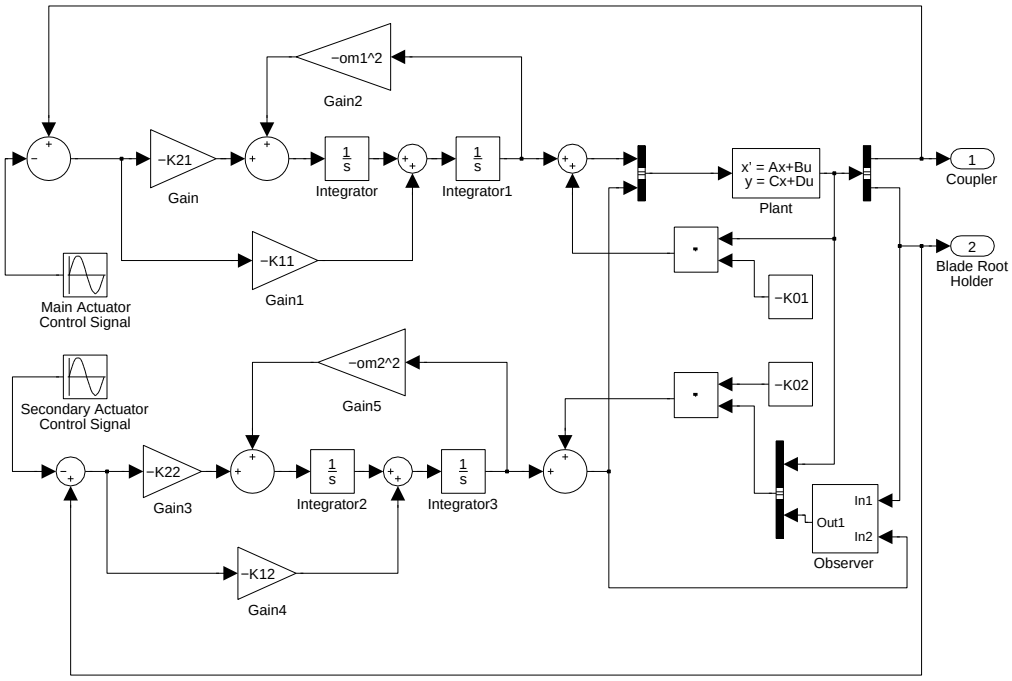


Figure 4.8: Schematic diagram of pitch controller.

blade root holder (body 2) and the rotary joint combination is a translational joint with its own spring damper. Illustrated in Figure 4.9, these additions are a step in establishing a realistic verification model.

With the upgraded stiff-blade model spinning at $2\pi/30$ radians/second, the blade pitch controller performs as shown in Figure 4.10. Noticeable ringing occurs at the beginning of each run. After that, the main actuator tracks the reference closely. Settling time for the base of the secondary actuator is longer. As designed, however, both actuators track with zero error in steady-state. The blade lags slightly, and has a higher amplitude than the reference.

In the step run from one collective pitch setting to another, the internal model ω^2 is set to 0; the main and secondary actuators have zero steady-state error. The output shaft of the secondary actuator and the blade have an equivalent offset.

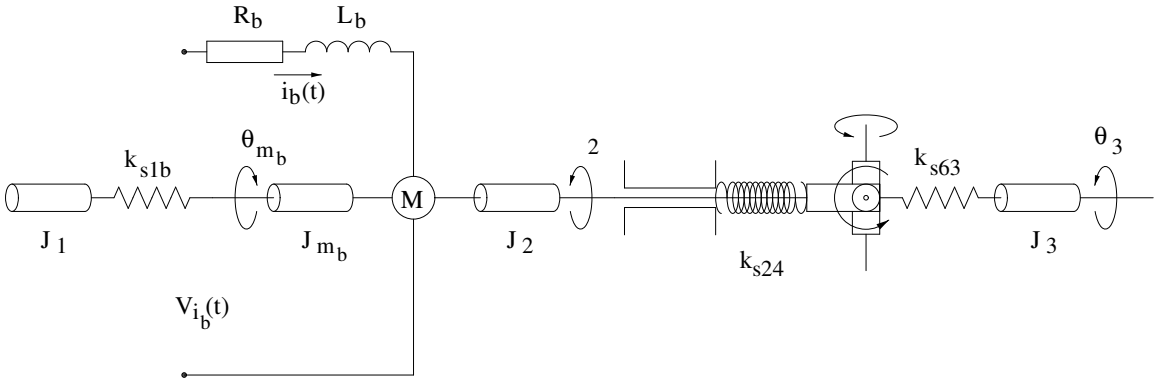


Figure 4.9: Arrangement of axial, in-plane and vertical spring-dampers, attached to pitch controller.

Maneuverability of the heliogyro depends on the behavior of the blades and the accuracy of the pitch controller. If the sail material is flat and straight the thrust vector can be pointed in any direction within 45 degrees of the Sun vector using an open-loop tracking strategy. Consider the case of a 3-blade heliogyro tracking a spiral trajectory with regard to its z axis using the half-p pitch maneuver. The blades are 1 meter wide and 100 meters long and spin at 1 rpm. The precession control law consists of the following procedure: at the end of a pitch cycle, determine the current spacecraft y and z axis and the desired z axis; take the cross product of the two z axes to establish a y axis set point; determine the change in

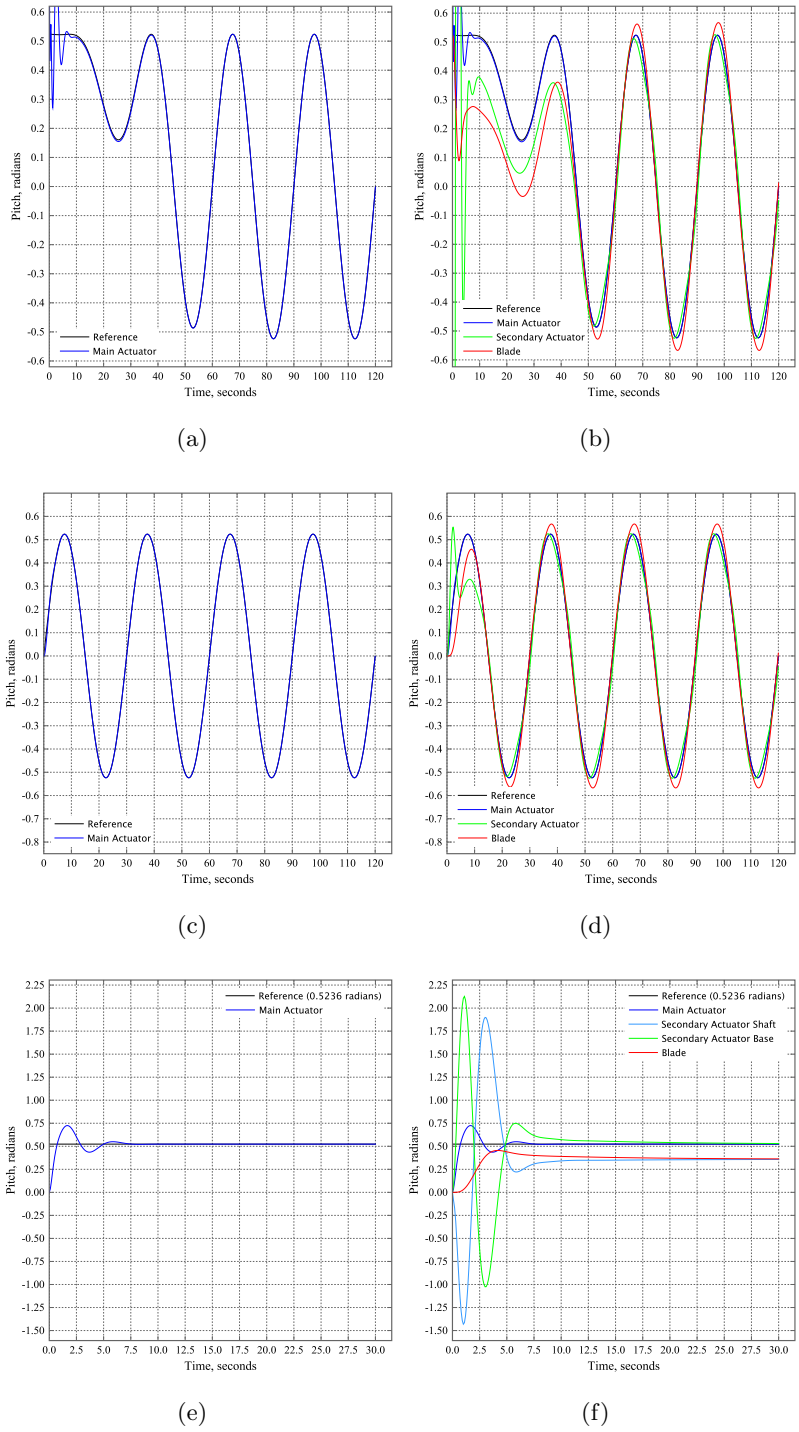


Figure 4.10: Pitch controller tracking a reference input. On the left are the reference and the main actuator responses only. On the right are the reference, the main and secondary actuators, and blade responses. Top to bottom: collective to cyclic transition (a, b);cyclic (c, d); and step (e, f).

phase necessary to align the precession; and set the desired phase for the end of the next pitch cycle. The y axis periodically updates to provide the correct precession axis.

Figure 4.11 shows the effectiveness of this strategy. Over a span of 25 hours, the stiff-blade heliogyro successfully arrives at 19 z-axis waypoints as far away as 45 degrees from the Sun vector. A dashed line in the plot connects waypoints to show the variance of the heliogyro from a direct path. With more waypoints, the accuracy would increase. Therefore, getting the blades straight and flat promises to provide pointing control over a wide operating region.

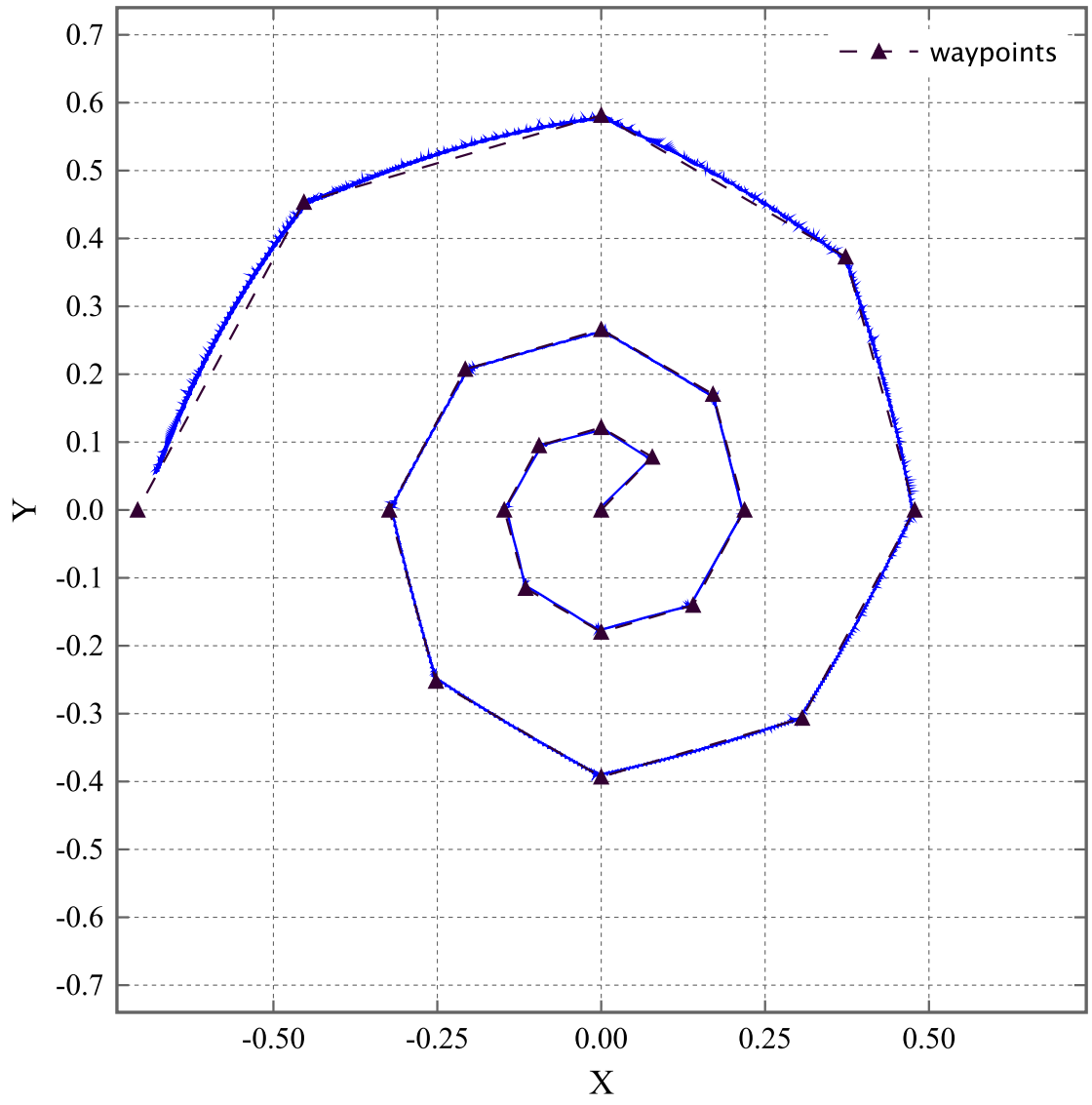


Figure 4.11: Z axis tracking path for 3-blade heliogyro with stiff 100 m blades spinning at 1 rpm. The entire trajectory takes approximately 25 hours.

Chapter 5

Conclusions

5.1 Impact/Significance

The modeling and control of solar sails developed in this research support the assertion that heliogyros could investigate the poles of the Sun, dwell at artificial LaGrange points, and cross the interstellar divide. With battens incorporated, heliogyro blades are sufficiently straight to provide the correct thrust to the heliogyro core. When blades are flat, it is shown that heliogyros can be pointed in any direction within 45 degrees of the Sun vector. Furthermore, heliogyro blades with aspect ratios up to 1000:1 can be pitched up to 30 degrees and not go unstable. In the steady state, the blade tip pitches in synchronization with the root. The pitch controller with dual actuation accurately pitches blades while attenuating secondary frequencies. The evidence indicates that heliogyros with blade aspect ratios up to 1000:1 can successfully operate in space.

5.2 Future Work

Autonomous, persistent solar sail guidance, navigation and control are crucial for aggressively sized heliogyros. The enormous solar sails for these missions must accurately navigate for years and must be robust to compensate for possible behavior changes due to sail damage and erosion, upsetting solar torque, and changes in solar radiation. A future system will include thrust vector control, a path following algorithm, and a path planner.

Automatic thrust vector control can receive attitude, position, and velocity information, as well as desired trajectory, to determine the pattern of maneuver parameters sent to the

blade pitch controller. Thrust control would utilize a mapping of maneuver parameters and spacecraft orientation to thrust and moment.

A trajectory planner that utilizes attitude, position, and velocity information as well as desired destination information to autonomously plan maneuvers, and a path planner comprise the other parts of the autonomous controller. A revised Model Predictive Control (MPC) strategy might be implemented to find the updated trajectory to be performed. This method uses the Newton root-finding method to iteratively modify an initial path to its final state using a best-state Newton update. The iteration is coupled to time, and uses future desired trajectories to update the path-planning process

Floquet theory and other techniques can provide an envelope of stable operating regions for the autonomous controller. The method relies on a state transition matrix, called the Floquet matrix, to determine if positive eigenvalues are present, given a certain subset of operational parameters.

Integration of out of plane blade damping must also be considered. When a heliogyro emerges from an eclipse, a step increase in solar force causes the blades to flap, which in turn prohibits control of the thrust vector. As indicated in the body of this research, flapping is also caused by regular operation. Proper damping is possible through a flexible beam/damper connecting the core and blade pitch mechanism that provides a blade flap offset for rotary damping.

With analysis complete, the next step is to prove that heliogyros can fly.

BIBLIOGRAPHY

Bibliography

[1] Beer, Ferdinand P., and E. Russell Johnston, Jr. *Mechanics of Materials*. New York: McGraw-Hill Book Company, 1981.

[2] Beer, Ferdinand P., and E. Russell Johnston, Jr. *Vector Mechanics for Engineers Dynamics*. Fourth ed. New York: McGraw-Hill Book Company, 1984.

[3] Blomquist, Richard Stuart. "Design Study of a Solid-State Heliogyro Solar Sail." Thesis. MIT, 1990.

[4] Craig, Jr., Roy R. *Structural Dynamics An Introduction to Computer Methods*. New York: John Wiley & Sons, 1981.

[5] Dachwald, Bernd, Ohndorf, Andreas, and Wie, Bong, "Solar Sail Trajectory Optimization for the Solar Polar Imager (SPI) Mission", *AIAA/AAS Astrodynamics Specialist Conference and Exhibit*, Keystone, Colorado, 21-24 August 2006.

[6] D'Azzo, John J., and Contantine H. Houpis. *Linear Control System Analysis & Design Conventional and Modern*. Third ed. United States of America: McGraw-Hill, Inc., 1988.

[7] Dorf, Richard C., and Robert H. Bishop. *Modern Control Systems*. Seventh ed. Reading: Addison-Wesley Company, 1995.

[8] Etzmuss, Olaf, Joachim Gross, and Wolfgang Strasser. "Deriving a Particle System from Continuum Mechanics for the Animation of Deformable Objects." *IEEE Transactions on Visualization and Computer Graphics* 9 (2003): 538-49.

[9] Franklin, Gene F., J. David Powell, and Abbas Emami-Naeini. *Feedback Control of Dynamic Systems*. 3rd ed. Reading: Addison-Wesley Company, 1995.

[10] Friedland, Bernard. *Control System Design An Introduction to State-Space Methods*. New York: McGraw-Hill, Inc., 1986.

[11] Friedman, L., et. al., "Solar Sailing-The Concept Made Realistic", AIAA paper 78-82, *16th Aerospace Sciences meeting*, Jan. 16-18, 1978.

[12] Friedman, Louis, *Starsailing: Solar Sails and Interstellar Travel*, John Wiley & Sons, Inc., New York, 1988.

[13] Greenspan, H. P., D. J. Benney, and J. E. Turner. *Calculus an introduction to applied mathematics*. Second ed. Toronto: McGraw-Hill Ryerson Limited, 1986.

[14] Hauth, Michael, and Olaf Etzmuss. "A High Performance Solver for the Animation of Deformable Objects using Advanced Numerical Methods." Computer Graphics Forum 20 (2001).

[15] Hedgepath, J., personal communication, 1990.

[16] Hollerbach, John M. "Class Notes." Introduction to Robotics. University of Utah, Salt Lake City. Fall 1997.

[17] House, Donald H., and David E. Breen, eds. *Cloth Modeling and Animation*. Natick: A K Peters Ltd., 2000.

[18] Kane, T.R., Likins, P.W., and Levinson, D.A., *Spacecraft Dynamics*, McGraw-Hill, New York, 1983.

[19] Kane, T. R., R. R. Ryan, and A. K. Banerjee. "Dynamics of a Cantilever Beam Attached to a Moving Base." *Journal of Guidance* 10 (1987): 139-51.

[20] Kane, Thomas R., and David A. Levinson. *Dynamics: Theory and Applications*. New York: McGraw-Hill Company, 1985.

[21] MacNeal, R. H., "The Heliogyro, An Interplanetary Flying Machine", NASA Contractor's Report CR 84460, June 1967.

[22] MacNeal, R. H., Structural Dynamics of the Heliogyro, NASA-CR-1745A, 1971.

[23] Marghitu, Dan B., and Malcolm J. Crocker. *Analytical Elements of Mechanisms*. Cambridge: Cambridge Unviversity P, 2001.

[24] Maxon Precision Motors, 1996-97 catalog.

[25] *Heliophysics: The New Science of the Sun-Solar System Connection : Recommended Roadmap for Science and Technology, 2005-2035*,www.nasa.gov, Feb. 2006.

[26] Mewaldt, R. A., and Liewer, P. C., "An Interstellar Probe Mission to the Boundaries of the Heliosphere and Nearby Interstellar Space http://interstellar. jpl. nasa. gov/outreach. html, 2000 - pdf.aiaa.org

[27] McInnes, Colin R. *Solar Sailing Technology, Dynamics and Mission Applications*. London: Springer, 1999.

[28] Meirovitch, Leonard. *Analytical Methods in Vibrations*. New York: Macmillan Company, Inc., 1967.

[29] Meirovitch, Leonard. *Elements of Vibration Analysis*. Second ed. New York: McGraw-Hill Book Company, 1986.

[30] *Instability of a rotating blade subjected to solar radiation pressure* Natori, Michihiro — Nemat-Nasser, S — Mitsugi, Jin *AIAA, ASME, ASCE, AHS, and ASC, Structures, Structural Dynamics and Materials Conference, 30th, Mobile, AL, Technical Papers. Part 1; 3-5 Apr. 1989. pp. 468-475. 1989*

[31] Nikravesh, P. E., R. A. Wehage, and O. K. Kwon. "Euler Parameters in Computational Kinematics and Dynamics, Part 1." *Journal of Mechanisms, Transmissions, and Automation in Design* 107 (1985): 358-69.

[32] ,Press, William H., *Numerical recipes in FORTRAN: the art of scientific computing, 2nd. ed.*,Cambridge University Press, 1992.

[33] Selby, Samuel M. *Standard Mathematical Tables*. Ed. William H. Beyer. 24th ed. Florida: CRC P, Inc., 1978.

[34] Shewchuk, Jonathan Richard. *An Introduction to the Conjugate Gradient Method Without the Agonizing Pain*. 4 Aug. 1994. Carnegie Mellon University. http://www-2. cs. cmu. edu/jrs/jrspapers. html.

[35] von Flotow, A. H., "A Solid State Heliogyro", technical proposal submitted to the Columbus Quincentenary Commission, Nov. 1989.

[36] Von Flotow, A. H., and D. Rosenthal. "Multi-Body Dynamics; An Algorithmic Approach Based Upon Kane's Equations." Class Notes. MIT, Boston. 18-22 June 1990.

[37] von Flotow, A. H., personal communication, July, 1990.

[38] Wells, Dare A. *Schaum's Outline of Theory and Problems of Lagrangian Dynamics with a treatment of Euler's Equations of Motion, Hamilton's Equations, and Hamilton's Principle*. New York: McGraw Hill Book Company, 1967.

[39] Wertz, James R., and Wiley J. Larson, eds. *Space Mission Analysis and Design*. Third ed. Torrance: Microcosm P, 1999.

APPENDICES

Appendix A

Pitch Parameter Transition

The blade pitch profile is given by the following equation:

$$\theta_{pitch} = \theta_{cyc} \sin\left(\omega\left(t - t_0\right) - \psi\right) + \theta_{1/2} \sin\left(\frac{1}{2}\left(\omega\left(t - t_0\right) - \frac{\pi}{2} - \psi\right)\right) + \theta_{coll} \tag{A.1}$$

Parameters determining the blade root pitch profile include

$$\begin{aligned}
\omega &= \text{ pitch angular velocity} \\
\psi &= \text{phase angle} \\
\theta_{cyc} &= \text{cyclic pitch amplitude} \\
\theta_{coll} &= \text{collective pitch amplitude} \\
\theta_{1/2} &= \text{half-p pitch amplitude} \\
t_0 &= \text{initial time}
\end{aligned}$$

Periodically, the parameters change to meet the control requirements.

Transitioning from one set of governing parameters to another requires a pair of smooth, second order continuous scaling functions to phase in the new profile and phase out the old. The function of choice is the half-sine wave. Illustrated in Figure A.1, the half-sine wave has zero slope at its beginning and end, providing a continuous profile throughout the transition.

The equation for the scaling function is

$$S = a + \frac{(b-a)}{2}\left[\sin\left(\omega_s t - \frac{\pi}{2}\right) + 1\right] \tag{A.2}$$

with

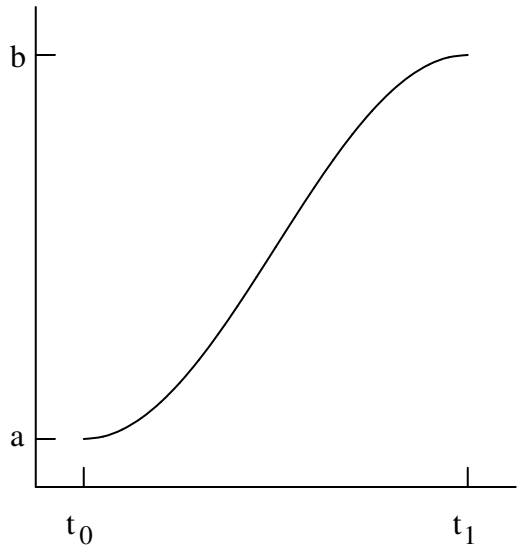


Figure A.1: Sine function for transition scaling factor

$$\omega_s = \frac{\pi}{(t_1 - t_0)}$$

$S =$ scaled value

$a =$ initial value

$b =$ final value

$t_1 =$ time at end of transition

Using the subscript A to indicate the old set of parameters and the subscript B to indicate the new, the pitch profile throughout the transition is

$$\theta_{pitch} = S_A\theta_A + S_B\theta_B \tag{A.3}$$

The values of a and b for cases A and B are shown in Table A.1

During a simulation the A parameters, the B parameters, and the transition time are specified. After transition, B parameters replace A parameters and a new set replaces B, based on the control law in place. An exception to this rule is ψ. Given a desired phase

Table A.1: Values of a and b for parameter sets A and B

	A	B
a	1	0
b	0	1

angle ψ_{des} at $t = t_1$, ψ_A and ψ_B are determined as follows, after the B parameters have replaced the A parameters:

$$\psi_A = \psi_B - \omega_A (t_1 - t_0) \tag{A.4}$$

$$\psi_B = \psi_{des} + \omega_B (t_1 - t_0) \tag{A.5}$$

In this way, the azimuth reference stays constant as the rotation rate changes.

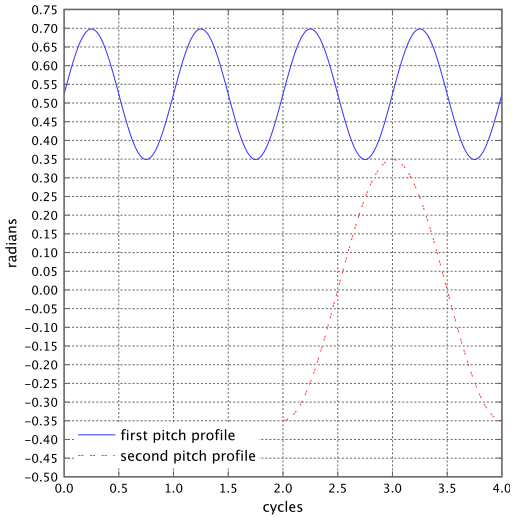
As an example of a transition, consider two profiles governed by parameter sets A and B in Table A.2. From Equations A.4 and A.5, ψ_A and ψ_B are unchanged. If the heliogyro rotation rate changes, ω_B will change, and then ψ_B will be different from the value before the transition.

Table A.2: Two example pitch profile parameter sets A and B

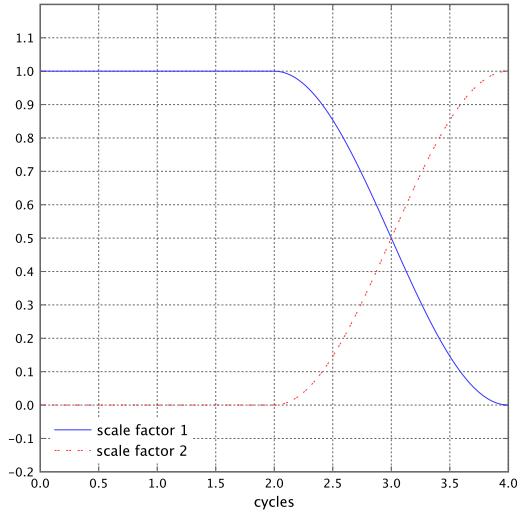
	A	B
ω	$\frac{\pi}{15}$	$\frac{\pi}{15}$
ψ	0	0
ψ_{des}		$\frac{\pi}{2}$
θ_{cyc}	$\frac{\pi}{18}$	0
θ_{coll}	$\frac{\pi}{6}$	0
$\theta_{1/2}$	0	$\frac{\pi}{9}$
t_0	60 s	
t_1		120 s

Using the given parameter sets, Figure A.2 illustrates the example given above. Figure A.2a shows the incoming and outgoing profiles; Figure A.2b shows the scale factors; and

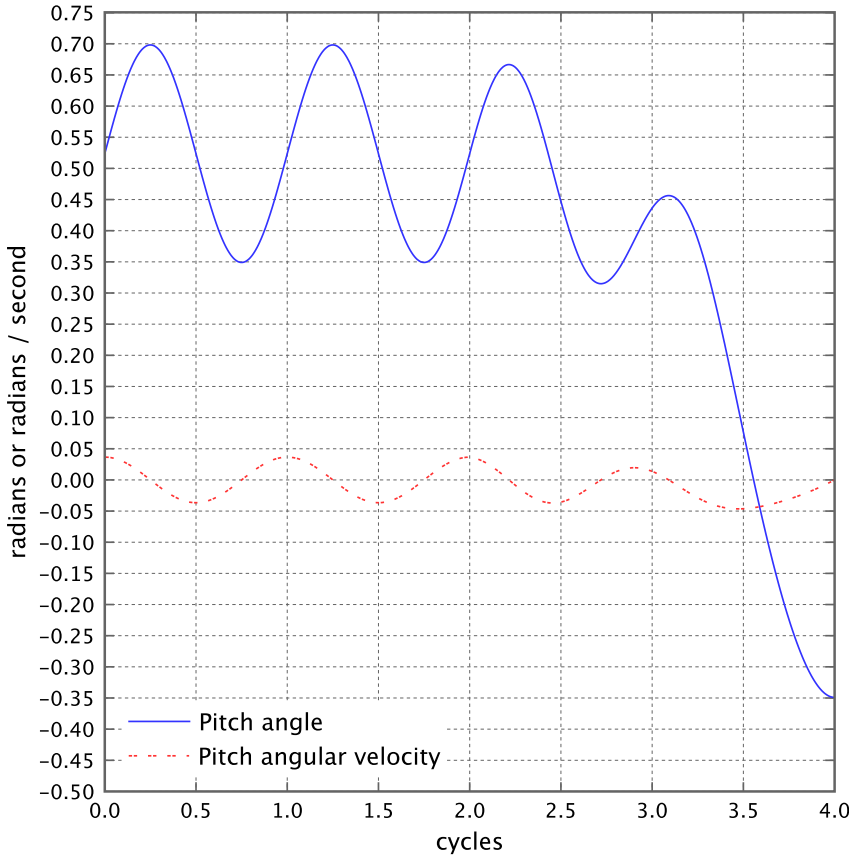
Figure A.2c illustrates the waveform and the derivative with respect to time of the waveform throughout the transition.



(a) Two profiles



(b) Scale factors for incoming and outgoing profiles



(c) Transition from incoming to outgoing profile

Figure A.2: Transition applied between two profiles

Appendix B

Particle Forces and Their Derivatives

B.1 Spring Force

The spring force between node A and node B is given by

$$\vec{F}_s = k_1 k_2 \vec{P}_d \tag{B.1}$$

where

$$k_1 = EA\left[\frac{\arctan\left[K\left[\frac{\|\vec{P}_d\|}{w}-1\right]\right]}{\pi}+0.5\right] \text{ for tension springs}$$

$$= \frac{EA}{\sqrt{2}\,(1+\nu)}\left[\frac{\arctan\left[K\left[\frac{\|\vec{P}_d\|}{w}-1\right]\right]}{\pi}+0.5\right] \text{ for shear springs}$$

$$k_2 = \left[\frac{1}{w}-\frac{1}{\left\|\vec{P}_d\right\|}\right]$$

$$\vec{P}_d = \vec{P}_B - \vec{P}_A$$

$K =$ nonlinear stiffness parameter

$w =$ resting distance between $\vec{P}_A$ and $\vec{P}_B$

$E =$ Young's Modulus for the blade material

$A =$ Cross-sectional area of material comprising the spring, $= wt$

$t =$ material thickness

The particle model in Section 2.3 requires the matrix of derivatives $\partial\vec{F}_{s_a}/\partial\vec{P}_{A_b}$, as well as the matrix of derivatives $\partial\vec{F}_{s_a}/\partial\vec{P}_{B_b}$, where $a = x,\ y,\ z$ refers to components of force and $b = x,\ y,\ z$ refers to components of position. To compactly write the matrices,

$$k_1' = \frac{CK}{\pi w\left[1+K^2\left(\frac{\|\vec{P}_d\|}{w}-1\right)^2\right]} \tag{B.2}$$

$$k_2' = \frac{1}{\left\|\vec{P}_d\right\|^2} \tag{B.3}$$

where $C = EA$ for tension springs and $C = EA/\sqrt{2}\,(1+\nu)$ for shear springs.

The matrix $\partial\vec{F}_{s_a}/\partial\vec{P}_{A_b}$ appears below. The matrix $\partial\vec{F}_{s_a}/\partial\vec{P}_{B_b}$ is $-\partial\vec{F}_{s_a}/\partial\vec{P}_{A_b}$.

$$\partial\vec{F}_{s_a}/\partial\vec{P}_{A_b} = -\left(k_1'k_2 + k_1k_2'\right)\cdot\begin{bmatrix} \frac{P_{d_x}^2}{\|\vec{P}_d\|}-k_1k_2 & \frac{P_{d_x}P_{d_y}}{\|\vec{P}_d\|} & \frac{P_{d_x}P_{d_z}}{\|\vec{P}_d\|} \\ \frac{P_{d_x}P_{d_y}}{\|\vec{P}_d\|} & \frac{P_{d_y}^2}{\|\vec{P}_d\|}-k_1k_2 & \frac{P_{d_y}P_{d_z}}{\|\vec{P}_d\|} \\ \frac{P_{d_x}P_{d_z}}{\|\vec{P}_d\|} & \frac{P_{d_y}P_{d_z}}{\|\vec{P}_d\|} & \frac{P_{d_z}^2}{\|\vec{P}_d\|}-k_1k_2 \end{bmatrix} \tag{B.4}$$

B.2 Damping Force

The equation for damping is

$$\vec{F}_d = C\left(\dot{\vec{P}}_d \cdot \vec{P}_d\right)\frac{\vec{P}_d}{\left\|\vec{P}_d\right\|^2} \tag{B.5}$$

where

$$C = \text{damping constant}$$
$$\vec{P}_d = \vec{P}_B - \vec{P}_A$$

With $\vec{F}_d$ a function of position and velocity, four derivative matrices are needed, namely $\partial\vec{F}_{d_a}/\partial\vec{P}_{A_b}$, $\partial\vec{F}_{d_a}/\partial\dot{\vec{P}}_{A_b}$, $\partial\vec{F}_{d_a}/\partial\vec{P}_{B_b}$, and $\partial\vec{F}_{d_a}/\partial\dot{\vec{P}}_{B_b}$, where $a = x, y, z$ refers to components of force and $b = x, y, z$ refers to components of position. The matrix $\partial\vec{F}_{d_a}/\partial\vec{P}_{A_b}$ appears below. The matrix $\partial\vec{F}_{d_a}/\partial\vec{P}_{B_b} = -\partial\vec{F}_{d_a}/\partial\vec{P}_{A_b}$.

(B.6)

$$\frac{\partial\vec{F}_{d_a}}{\partial\vec{P}_{A_b}} =$$
$$-C\cdot\begin{bmatrix} \frac{\dot{\vec{P}}_d\cdot\vec{P}_d+\dot{P}_{d_x}P_{d_x}}{\left\|\vec{P}_d\right\|^2}-\frac{2\left(\dot{\vec{P}}_d\cdot\vec{P}_d\right)P_{d_x}^2}{\left\|\vec{P}_d\right\|^4} & \frac{\dot{P}_{d_y}P_{d_x}}{\left\|\vec{P}_d\right\|^2}-\frac{2\left(\dot{\vec{P}}_d\cdot\vec{P}_d\right)P_{d_x}P_{d_y}}{\left\|\vec{P}_d\right\|^4} & \frac{\dot{P}_{d_z}P_{d_x}}{\left\|\vec{P}_d\right\|^2}-\frac{2\left(\dot{\vec{P}}_d\cdot\vec{P}_d\right)P_{d_x}P_{d_z}}{\left\|\vec{P}_d\right\|^4} \\ \frac{\dot{P}_{d_x}P_{d_y}}{\left\|\vec{P}_d\right\|^2}-\frac{2\left(\dot{\vec{P}}_d\cdot\vec{P}_d\right)P_{d_x}P_{d_y}}{\left\|\vec{P}_d\right\|^4} & \frac{\dot{\vec{P}}_d\cdot\vec{P}_d+\dot{P}_{d_y}P_{d_y}}{\left\|\vec{P}_d\right\|^2}-\frac{2\left(\dot{\vec{P}}_d\cdot\vec{P}_d\right)P_{d_y}^2}{\left\|\vec{P}_d\right\|^4} & \frac{\dot{P}_{d_z}P_{d_y}}{\left\|\vec{P}_d\right\|^2}-\frac{2\left(\dot{\vec{P}}_d\cdot\vec{P}_d\right)P_{d_y}P_{d_z}}{\left\|\vec{P}_d\right\|^4} \\ \frac{\dot{P}_{d_x}P_{d_z}}{\left\|\vec{P}_d\right\|^2}-\frac{2\left(\dot{\vec{P}}_d\cdot\vec{P}_d\right)P_{d_x}P_{d_z}}{\left\|\vec{P}_d\right\|^4} & \frac{\dot{P}_{d_y}P_{d_z}}{\left\|\vec{P}_d\right\|^2}-\frac{2\left(\dot{\vec{P}}_d\cdot\vec{P}_d\right)P_{d_y}P_{d_z}}{\left\|\vec{P}_d\right\|^4} & \frac{\dot{\vec{P}}_d\cdot\vec{P}_d+\dot{P}_{d_z}P_{d_z}}{\left\|\vec{P}_d\right\|^2}-\frac{2\left(\dot{\vec{P}}_d\cdot\vec{P}_d\right)P_{d_z}^2}{\left\|\vec{P}_d\right\|^4} \end{bmatrix}$$

The matrix $\partial\vec{F}_{d_a}/\partial\dot{\vec{P}}_{A_b}$ is in Equation B.7. The matrix $\partial\vec{F}_{d_a}/\partial\dot{\vec{P}}_{B_b} = -\partial\vec{F}_{d_a}/\partial\dot{\vec{P}}_{A_b}$.

$$\frac{\partial\vec{F}_{d_a}}{\partial\dot{\vec{P}}_{A_b}} = -\frac{C}{\left\|\vec{P}_d\right\|^2}\cdot\begin{bmatrix} {P_{d_x}}^2 & P_{d_x}P_{d_y} & P_{d_x}P_{d_z} \\ P_{d_x}P_{d_y} & {P_{d_y}}^2 & P_{d_y}P_{d_z} \\ P_{d_x}P_{d_z} & P_{d_y}P_{d_z} & {P_{d_z}}^2 \end{bmatrix} \tag{B.7}$$

B.3 Gravitational Force

Gravitational Force, $\vec{G}$, is

$$\vec{G}_{cb} = -\frac{GM_{cb}m_p}{\left\|\vec{P}_{pcb}\right\|^3}\vec{P}_{pcb} \tag{B.8}$$

with

$$\begin{aligned} G &= \text{gravitational constant} \\ M_{cb} &= \text{mass of a celestial body} \\ m_p &= \text{mass of a particle in the blade mesh} \\ \vec{P}_{pcb} &= \text{vector from a particle to the celestial body} \end{aligned}$$

The matrix $\partial\vec{G}_{cb_a}/\partial P_{p_b}$, where $a = x,\ y,\ z$ refers to components of force and $b = x,\ y,\ z$ refers to components of position, is

$$\frac{\partial\vec{G}_{cb}}{\partial P_p} = -GM_{cb}m_p \cdot \begin{bmatrix} \frac{1}{\left\|\vec{P}_{pcb}\right\|^3} - \frac{3{P_x}^2}{\left\|\vec{P}_{pcb}\right\|^5} & -\frac{3P_xP_y}{\left\|\vec{P}_{pcb}\right\|^5} & -\frac{3P_xP_z}{\left\|\vec{P}_{pcb}\right\|^5} \\ -\frac{3P_xP_y}{\left\|\vec{P}_{pcb}\right\|^5} & \frac{1}{\left\|\vec{P}_{pcb}\right\|^3} - \frac{3{P_y}^2}{\left\|\vec{P}_{pcb}\right\|^5} & -\frac{3P_yP_z}{\left\|\vec{P}_{pcb}\right\|^5} \\ -\frac{3P_xP_z}{\left\|\vec{P}_{pcb}\right\|^5} & -\frac{3P_yP_z}{\left\|\vec{P}_{pcb}\right\|^5} & \frac{1}{\left\|\vec{P}_{pcb}\right\|^3} - \frac{3{P_z}^2}{\left\|\vec{P}_{pcb}\right\|^5} \end{bmatrix} \tag{B.9}$$

B.4 Solar Force

The equation for solar force is

$$\vec{F}_{Solar} = \vec{F}_R + \vec{F}_A = 2\frac{SA}{c}\left(\frac{r_0}{r_s}\right)^2 f_r \cos^2\theta\vec{N} + \frac{SA}{c}\left(\frac{r_0}{r_s}\right)^2 (1 - f_r)\cos\theta S\vec{u}n \tag{B.10}$$

where

$F_R =$ force due to photon reflection

$F_A =$ force due to photon absorption

$S =$ Solar flux , $\approx 1367\ W/m^2$ at 1 AU

$r_0 =$ distance from the Earth to the center of the Sun

$r_s =$ distance from the heliogyro to the center of the Sun

$f_r =$ coefficient of reflectivity

$\theta =$ angle between the Sun vector and the sail surface normal

$\vec{N} =$ sail surface normal

$\vec{Sun} =$ Sun vector

$A =$ sail surface area

$c =$ speed of light.

To calculate the solar force and its derivative matrix, the blade mesh is divided into triangles, with the solar force divided among the three nodes comprising each triangle. For a triangle with nodes 1, 2, and 3, the vectors $\vec{A} = \vec{P}_2 - \vec{P}_1$ and $\vec{B} = \vec{P}_3 - \vec{P}_1$ are computed. The following calculations then follow.

(B.11) $$C_1 = \frac{S\, f_r}{c}\left(\frac{r_0}{r_s}\right)^2$$

(B.12) $$C_2 = \frac{S\,(1-f_r)}{2c}\left(\frac{r_0}{r_s}\right)^2$$

(B.13) $$\vec{D} = \vec{A} \times \vec{B}$$

(B.14) $$\cos\theta = \frac{\vec{D}}{\left\|\vec{D}\right\|} \cdot \vec{Sun}$$

(B.15) $$\vec{N} = \frac{\vec{D}}{\left\|\vec{D}\right\|}$$

(B.16) $$\vec{F}_{Solar} = C_1 \cos\theta^2 \vec{D} + C_2 \cos\theta \left\|\vec{D}\right\| \vec{Sun}$$

(B.17) $$\frac{\partial F_{Sun_a}}{\partial D_b} = C_1 \left[2D_a \left(\frac{\left\|\vec{D}\right\|^2 Sun_b \left(\vec{D} \cdot \vec{Sun}\right) - \left(\vec{D} \cdot \vec{Sun}\right)^2 D_b}{\left\|\vec{D}\right\|^4} \right) \right] + C_2 Sun_a Sun_b + (\text{ if b = a }) C_1 \cos\theta^2$$

(B.18) $$\frac{\partial \vec{D}}{\partial P_{2_b}} = \begin{bmatrix} 0 & B_z & -B_y \\ -B_z & 0 & B_x \\ B_y & -B_x & 0 \end{bmatrix}$$

(B.19) $$\frac{\partial \vec{D}}{\partial P_{3_b}} = \begin{bmatrix} 0 & -A_z & A_y \\ A_z & 0 & -A_x \\ -A_y & A_x & 0 \end{bmatrix}$$

(B.20) $$\frac{\partial \vec{D}}{\partial P_{1_b}} = -\left(\frac{\partial D_a}{\partial P_{2_b}} + \frac{\partial D_a}{\partial P_{3_b}}\right)$$

(B.21) Finally, $\frac{\partial \vec{F}_{Solar}}{\partial P_i} = \frac{\partial \vec{F}_{Solar}}{\partial \vec{D}} \frac{\partial \vec{D}}{\partial P_i}$ where i is particle 1,2,or 3

Appendix C

Sinusoid_fit.m: A Matlab Script for Sinusoid Curve Fitting. [16]

```
% sinusoid_fit.m Fit a 4-parameter sinusoid curve
%
% phi = sinusoid_fit(th,y,phi0) fits a 4-parameter sine curve of
% the form:
% y = phi(1)*cos(phi(4)*th) + phi(2)*sin(phi(4)*th) + phi(3)
% % where
% phi = vector of estimates
% th = vector of joint angle readings
% y = vector of output readings
% phi0 = initial estimate of phi
%
% uses ordinary least squares iteratively to the linearized sine curve

function phi = sinusoid_fit(th,y,phi0)

% Set initial conditions
phi = phi0; N = size(th,1);

% Apply OLS iteratively. Set boundaries of the search
niter = 200; iter = 0; res = 1;

disp(' Iteration Residual');
format compact; format short e;
while (iter ¡ niter & res ¿ 1e-10),
iter = iter + 1;
theta = phi(4) * th;
sine = sin(theta); cosine = cos(theta);

% Compute the output error
```

```
dy = y - (phi(1) * cosine + phi(2) * sine + phi(3));

% Compute the gradient
C(:,1) = cosine;
C(:,2) = sine;
C(:,3) = ones(N,1);
C(:,4) = th .* (-phi(1)*sine + phi(2)*cosine);

% Apply OLS, update results, and display residual

dphi = (C  dy); phi = phi + dphi;
res = norm(dphi); disp([iter,res]);
end

% Plot comparison of measured to predicted points

plot(th,y,'rx-',th,phi(1)*cos(phi(4)*th)+phi(2)*sin(phi(4)*th)+phi(3),'bo-')
```

Appendix D

Sine Fit Parameters

Table D.1: Primary parameters ϕ for blade root, blade tip, and 90% of span for a 10 meter blade undergoing cyclic pitch and with no solar pressure present.

Pitch Freq. Ratio		ϕ_1	ϕ_2	ϕ_3	ϕ_4	Amplitude (rad)	Phase (rad)	Amp. Ratio w/Root
0.2	root	2.19E-04	5.24E-01	5.69E-09	4.19E-02	5.24E-01	1.57	
	tip	-9.03E-03	3.87E-01	3.82E-03	4.23E-02	3.87E-01	1.59	0.739
	90%	-9.39E-03	3.97E-01	3.59E-03	4.23E-02	3.97E-01	1.59	0.759
0.4	root	4.39E-04	5.24E-01	2.06E-08	8.38E-02	5.24E-01	1.57	
	tip	-4.39E-03	4.04E-01	-2.08E-03	8.40E-02	4.04E-01	1.58	0.771
	90%	-4.79E-03	4.12E-01	-1.56E-03	8.40E-02	4.12E-01	1.58	0.786
0.6	root	6.58E-04	5.24E-01	-3.87E-09	1.26E-01	5.24E-01	1.57	
	tip	-1.70E-03	4.31E-01	-5.22E-05	1.26E-01	4.31E-01	1.57	0.822
	90%	-2.23E-03	4.35E-01	3.40E-05	1.26E-01	4.35E-01	1.58	0.831
0.8	root	8.77E-04	5.24E-01	-2.57E-09	1.68E-01	5.24E-01	1.57	
	tip	6.37E-03	4.71E-01	1.01E-04	1.67E-01	4.71E-01	1.56	0.899
	90%	6.07E-03	4.73E-01	-5.23E-05	1.67E-01	4.73E-01	1.56	0.904
1.0	root	1.10E-03	5.24E-01	-6.38E-10	2.09E-01	5.24E-01	1.57	
	tip	2.27E-03	5.74E-01	2.07E-04	2.09E-01	5.74E-01	1.57	1.097
	90%	1.97E-03	5.71E-01	2.03E-04	2.09E-01	5.71E-01	1.57	1.091
1.2	root	1.32E-03	5.24E-01	-6.30E-08	2.51E-01	5.24E-01	1.57	
	tip	6.20E-03	6.40E-01	4.69E-03	2.51E-01	6.40E-01	1.56	1.222
	90%	6.12E-03	6.33E-01	4.38E-03	2.51E-01	6.33E-01	1.56	1.209

Table D.2: Primary parameters ϕ for blade root, blade tip, and 90% of span for a 10 meter blade undergoing cyclic pitch and with solar pressure present.

Pitch Freq. Ratio		ϕ_1	ϕ_2	ϕ_3	ϕ_4	Amplitude (rad)	Phase (rad)	Amp. Ratio w/Root
0.2	root	2.19E-04	5.24E-01	2.03E-07	4.19E-02	5.24E-01	1.57	
	tip	-1.54E-02	3.54E-01	1.18E-03	4.25E-02	3.54E-01	1.61	0.676
	90%	-1.53E-02	3.65E-01	6.64E-04	4.25E-02	3.65E-01	1.61	0.698
0.4	root	4.39E-04	5.24E-01	1.96E-07	8.38E-02	5.24E-01	1.57	
	tip	4.58E-03	3.81E-01	7.52E-04	8.39E-02	3.81E-01	1.56	0.727
	90%	3.80E-03	3.87E-01	2.48E-04	8.39E-02	3.87E-01	1.56	0.740
0.6	root	6.58E-04	5.24E-01	1.87E-07	1.26E-01	5.24E-01	1.57	
	tip	5.39E-03	4.14E-01	3.61E-03	1.26E-01	4.14E-01	1.56	0.791
	90%	5.50E-03	4.19E-01	3.14E-03	1.26E-01	4.19E-01	1.56	0.799
0.8	root	8.77E-04	5.24E-01	1.59E-07	1.68E-01	5.24E-01	1.57	
	tip	8.00E-03	4.54E-01	1.02E-03	1.67E-01	4.55E-01	1.55	0.868
	90%	6.94E-03	4.57E-01	7.50E-04	1.67E-01	4.57E-01	1.56	0.873
1.0	root	1.10E-03	5.24E-01	1.56E-07	2.09E-01	5.24E-01	1.57	
	tip	5.31E-03	5.70E-01	6.42E-04	2.09E-01	5.70E-01	1.56	1.089
	90%	5.50E-03	5.68E-01	2.66E-04	2.09E-01	5.68E-01	1.56	1.085
1.2	root	1.32E-03	5.24E-01	1.82E-07	2.51E-01	5.24E-01	1.57	
	tip	-3.99E-03	6.45E-01	3.00E-03	2.51E-01	6.45E-01	1.58	1.231
	90%	-3.70E-03	6.38E-01	2.71E-03	2.51E-01	6.38E-01	1.58	1.219

Table D.3: Primary parameters ϕ for blade root, blade tip, and 90% of span for a 100 meter blade undergoing cyclic pitch and with no solar pressure present.

Pitch Freq. Ratio		ϕ_1	ϕ_2	ϕ_3	ϕ_4	Amplitude (rad)	Phase (rad)	Amp. Ratio w/Root
0.2	root	2.19E-04	5.24E-01	-7.22E-12	4.19E-02	5.24E-01	1.57	
	tip	-1.98E-03	2.34E-01	1.12E-03	4.21E-02	2.34E-01	1.58	0.447
	90%	-2.32E-03	2.54E-01	9.37E-04	4.21E-02	2.54E-01	1.58	0.485
0.4	root	4.39E-04	5.24E-01	-3.06E-11	8.38E-02	5.24E-01	1.57	
	tip	-1.05E-02	2.58E-01	-2.65E-03	8.40E-02	2.58E-01	1.61	0.494
	90%	-9.81E-03	2.76E-01	-2.44E-03	8.40E-02	2.77E-01	1.61	0.528
0.6	root	6.58E-04	5.24E-01	5.52E-11	1.26E-01	5.24E-01	1.57	
	tip	2.83E-03	2.99E-01	-4.23E-04	1.26E-01	2.99E-01	1.56	0.572
	90%	1.79E-03	3.16E-01	-3.74E-04	1.26E-01	3.16E-01	1.57	0.604
0.8	root	8.77E-04	5.24E-01	-8.16E-11	1.68E-01	5.24E-01	1.57	
	tip	7.05E-03	3.98E-01	4.68E-03	1.68E-01	3.98E-01	1.55	0.760
	90%	6.58E-03	4.08E-01	3.34E-03	1.68E-01	4.08E-01	1.55	0.778
1.0	root	1.10E-03	5.24E-01	-1.85E-10	2.09E-01	5.24E-01	1.57	
	tip	6.24E-02	6.95E-01	-2.48E-03	2.08E-01	6.98E-01	1.48	1.334
	90%	5.21E-02	6.77E-01	-3.28E-03	2.08E-01	6.79E-01	1.49	1.297
1.2	root	1.32E-03	5.24E-01	1.74E-07	2.51E-01	5.24E-01	1.57	
	tip	-8.15E-01	-5.72E-01	-2.66E-02	2.51E-01	9.96E-01	-2.53	1.901
	90%	-9.40E-01	-5.72E-01	-3.34E-02	2.51E-01	1.10E+00	-2.60	2.102

Table D.4: Primary parameters ϕ for blade root, blade tip, and 90% of span for a 100 meter blade undergoing cyclic pitch and with solar pressure present.

Pitch Freq. Ratio		ϕ_1	ϕ_2	ϕ_3	ϕ_4	Amplitude (rad)	Phase (rad)	Amp. Ratio w/Root
0.2	root	2.19E-04	5.24E-01	9.28E-09	4.19E-02	5.24E-01	1.57	
	tip	-7.88E-04	2.35E-01	-8.07E-03	4.12E-02	2.35E-01	1.57	0.448
	90%	-7.31E-03	2.52E-01	-7.39E-03	4.15E-02	2.52E-01	1.60	0.481
0.4	root	4.29E-04	5.24E-01	-2.46E-06	8.38E-02	5.24E-01	1.57	
	tip	-4.42E-02	2.41E-01	-2.35E-02	8.78E-02	2.45E-01	1.75	0.467
	90%	-4.30E-02	2.40E-01	-2.01E-02	8.75E-02	2.44E-01	1.75	0.466
0.6	root	6.58E-04	5.24E-01	1.63E-08	1.26E-01	5.24E-01	1.57	
	tip	4.61E-04	2.89E-01	-4.42E-04	1.26E-01	2.89E-01	1.57	0.552
	90%	1.76E-03	3.05E-01	-2.06E-05	1.26E-01	3.05E-01	1.57	0.583
0.8	root	8.77E-04	5.24E-01	3.70E-07	1.68E-01	5.24E-01	1.57	
	tip	7.98E-02	3.26E-01	-2.14E-03	1.70E-01	3.35E-01	1.33	0.641
	90%	8.38E-02	3.32E-01	2.64E-04	1.70E-01	3.43E-01	1.32	0.654
1.0	root	1.10E-03	5.24E-01	3.68E-09	2.09E-01	5.24E-01	1.57	
	tip	2.60E-02	7.55E-01	1.09E-02	2.09E-01	7.55E-01	1.54	1.443
	90%	2.49E-02	7.35E-01	1.22E-02	2.09E-01	7.35E-01	1.54	1.404
1.2	root	1.32E-03	5.24E-01	-5.35E-08	2.51E-01	5.24E-01	1.57	
	tip	-8.14E-01	-3.97E-01	1.83E-02	2.52E-01	9.06E-01	-2.69	1.730
	90%	-9.51E-01	-4.87E-01	8.01E-02	2.54E-01	1.07E+00	-2.67	2.040

Table D.5: Primary parameters ϕ for blade root, blade tip, and 90% of span for a 1000 meter blade undergoing cyclic pitch and with no solar pressure present.

Pitch Freq. Ratio		ϕ_1	ϕ_2	ϕ_3	ϕ_4	Amplitude (rad)	Phase (rad)	Amp. Ratio w/Root
0.2	root	2.19E-04	5.24E-01	-1.32E-10	4.19E-02	5.24E-01	1.57	
	tip	1.16E-02	2.49E-01	-4.92E-03	4.13E-02	2.50E-01	1.52	0.477
	90%	5.38E-03	2.64E-01	-1.32E-03	4.16E-02	2.64E-01	1.55	0.504
0.4	root	4.39E-04	5.24E-01	-8.61E-11	8.38E-02	5.24E-01	1.57	
	tip	2.68E-03	2.75E-01	-5.39E-06	8.35E-02	2.75E-01	1.56	0.526
	90%	9.68E-03	2.85E-01	1.34E-03	8.34E-02	2.85E-01	1.54	0.545
0.6	root	6.58E-04	5.24E-01	-2.85E-11	1.26E-01	5.24E-01	1.57	
	tip	-6.69E-03	3.39E-01	1.01E-02	1.27E-01	3.39E-01	1.59	0.647
	90%	-7.73E-04	3.27E-01	2.22E-03	1.26E-01	3.27E-01	1.57	0.625
0.8	root	8.77E-04	5.24E-01	-1.13E-11	1.68E-01	5.24E-01	1.57	
	tip	2.43E-02	4.09E-01	-2.91E-03	1.67E-01	4.10E-01	1.51	0.782
	90%	-9.30E-03	4.14E-01	-2.59E-03	1.68E-01	4.14E-01	1.59	0.792
1.0	root	1.10E-03	5.24E-01	-6.48E-11	2.09E-01	5.24E-01	1.57	
	tip	-9.54E-02	6.93E-01	2.47E-03	2.11E-01	7.00E-01	1.71	1.340
	90%	3.38E-02	6.42E-01	2.00E-03	2.09E-01	6.43E-01	1.52	1.230
1.2	root	1.32E-03	5.24E-01	-1.26E-09	2.51E-01	5.24E-01	1.57	
	tip	-6.37E-01	2.40E-01	1.96E-01	2.56E-01	6.80E-01	2.78	1.300
	90%	-1.12E+00	4.28E-01	6.00E-03	2.52E-01	1.20E+00	2.78	2.280

Table D.6: Primary parameters ϕ for blade root, blade tip, and 90% of span for a 1000 meter blade undergoing cyclic pitch and with solar pressure present.

Pitch Freq. Ratio		ϕ_1	ϕ_2	ϕ_3	ϕ_4	Amplitude (rad)	Phase (rad)	Amp. Ratio w/Root
0.6	root	6.58E-04	5.24E-01	2.79E-08	1.26E-01	5.24E-01	1.57	
	tip	1.41E-02	3.12E-01	7.13E-03	1.25E-01	3.12E-01	1.53	0.596
	90%	-9.43E-03	3.35E-01	1.65E-03	1.26E-01	3.35E-01	1.60	0.639
0.8	root	8.77E-04	5.24E-01	4.27E-09	1.68E-01	5.24E-01	1.57	
	tip	-1.56E-02	4.17E-01	-8.28E-04	1.69E-01	4.17E-01	1.61	0.797
	90%	6.91E-03	4.10E-01	5.92E-03	1.68E-01	4.10E-01	1.55	0.782
1.0	root	1.10E-03	5.24E-01	4.42E-09	2.09E-01	5.24E-01	1.57	
	tip	-8.65E-02	7.42E-01	3.92E-03	2.11E-01	7.47E-01	1.69	1.426
	90%	1.31E-02	7.07E-01	5.65E-03	2.10E-01	7.07E-01	1.55	1.351
1.2	root	-4.34E-03	5.24E-01	1.60E-08	2.51E-01	5.24E-01	1.58	
	tip	1.14E-01	-3.46E-01	-2.94E-01	2.19E-01	3.64E-01	-1.25	0.696
	90%	-9.41E-01	1.28E-01	1.05E-02	2.55E-01	9.49E-01	3.01	1.813

Table D.7: Primary parameters ϕ for blade root, blade tip, and 90% of span for a 1000 meter blade with battens every 50 m undergoing cyclic pitch and with no solar pressure present.

Pitch Freq. Ratio		ϕ_1	ϕ_2	ϕ_3	ϕ_4	Amplitude (rad)	Phase (rad)	Amp. Ratio w/Root
1.0	root	1.10E-03	5.24E-01	-1.13E-11	2.09E-01	5.24E-01	1.57	
	tip	7.67E-02	6.81E-01	4.44E-03	2.08E-01	6.85E-01	1.46	1.31
	90%	7.00E-02	6.64E-01	3.69E-03	2.08E-01	6.68E-01	1.47	1.28

Table D.8: Secondary parameters ϕ for blade root, blade tip, and 90% of span for a 10 meter blade undergoing cyclic pitch and with no solar pressure present.

Pitch Freq. Ratio		ϕ_1	ϕ_2	ϕ_3	ϕ_4	Amplitude (rad)	Phase (rad)	Amp. Ratio w/Root
0.2	tip	4.20E-03	5.78E-03	-7.14E-06	5.35E-01	7.15E-03	0.94	0.752
	90%	3.73E-03	4.68E-03	-8.04E-06	5.34E-01	5.98E-03	0.90	0.770
0.4	tip	4.70E-04	-1.21E-02	-5.30E-06	4.18E-01	1.21E-02	-1.53	0.794
	90%	8.51E-04	-1.10E-02	-5.82E-06	4.19E-01	1.10E-02	-1.49	0.807
0.6	tip	1.80E-03	-2.45E-02	-5.01E-06	3.78E-01	2.45E-02	-1.50	0.869
	90%	2.16E-03	-2.28E-02	-6.49E-06	3.78E-01	2.30E-02	-1.48	0.875
0.8	tip	1.16E-03	2.94E-02	-7.65E-06	5.03E-01	2.94E-02	1.53	0.955
	90%	8.94E-04	2.64E-02	-9.00E-06	5.03E-01	2.64E-02	1.54	0.954
1.0	tip	-8.54E-04	5.01E-03	3.00E-06	6.30E-01	5.08E-03	1.74	1.107
	90%	-5.88E-04	4.49E-03	1.93E-07	6.30E-01	4.53E-03	1.70	1.100
1.2	tip	3.42E-02	5.35E-02	-1.29E-04	5.02E-01	6.35E-02	1.00	1.343
	90%	3.30E-02	4.88E-02	-1.18E-04	5.01E-01	5.89E-02	0.98	1.322

Table D.9: Secondary parameters ϕ for blade root, blade tip, and 90% of span for a 10 meter blade undergoing cyclic pitch and with solar pressure present.

Pitch Freq. Ratio		ϕ_1	ϕ_2	ϕ_3	ϕ_4	Amplitude (rad)	Phase (rad)	Amp. Ratio w/Root
0.2	tip	1.05E-02	-6.76E-03	-4.11E-05	3.89E-01	1.25E-02	-0.57	0.700
	90%	9.66E-03	-6.02E-03	-4.18E-05	3.89E-01	1.14E-02	-0.56	0.720
0.4	tip	1.76E-02	1.01E-02	-1.28E-04	4.19E-01	2.03E-02	0.52	0.766
	90%	1.71E-02	8.87E-03	-1.20E-04	4.19E-01	1.92E-02	0.48	0.776
0.6	tip	2.07E-02	-3.82E-02	1.12E-04	3.73E-01	4.34E-02	-1.07	0.874
	90%	1.96E-02	-3.63E-02	9.62E-05	3.73E-01	4.13E-02	-1.07	0.878
0.8	tip	2.72E-03	2.09E-02	-3.53E-05	5.04E-01	2.11E-02	1.44	0.908
	90%	3.20E-03	1.93E-02	-3.33E-05	5.03E-01	1.96E-02	1.41	0.910
1.0	tip	-5.43E-03	1.93E-02	1.19E-05	4.17E-01	2.01E-02	1.84	1.128
	90%	-4.87E-03	1.81E-02	9.64E-06	4.17E-01	1.87E-02	1.83	1.121
1.2	tip	3.00E-03	1.80E-02	-2.52E-04	5.11E-01	1.82E-02	1.41	1.266
	90%	2.68E-03	1.69E-02	-2.39E-04	5.11E-01	1.71E-02	1.41	1.251

Table D.10: Secondary parameters ϕ for blade root, blade tip, and 90% of span for a 100 meter blade undergoing cyclic pitch and with no solar pressure present.

Pitch Freq. Ratio		ϕ_1	ϕ_2	ϕ_3	ϕ_4	Amplitude (rad)	Phase (rad)	Amp. Ratio w/Root
0.2	tip	-4.23E-02	4.02E-02	-1.12E-03	3.10E-01	5.83E-02	2.38	0.559
	90%	-3.63E-02	3.57E-02	-9.89E-04	3.10E-01	5.09E-02	2.37	0.582
0.4	tip	-6.77E-02	-5.15E-02	3.14E-03	3.09E-01	8.51E-02	-2.49	0.656
	90%	-5.96E-02	-4.44E-02	2.74E-03	3.09E-01	7.44E-02	-2.50	0.670
0.6	tip	4.66E-02	-3.28E-02	5.55E-04	3.09E-01	5.70E-02	-0.61	0.681
	90%	4.01E-02	-2.94E-02	5.00E-04	3.09E-01	4.97E-02	-0.63	0.699
0.8	tip	6.29E-02	2.42E-02	-2.59E-03	3.02E-01	6.74E-02	0.37	0.889
	90%	5.49E-02	2.44E-02	-2.36E-03	3.03E-01	6.01E-02	0.42	0.893
1.0	tip	3.29E-01	-6.28E-02	1.95E-03	2.86E-01	3.35E-01	-0.19	1.974
	90%	2.92E-01	-5.58E-02	1.63E-03	2.86E-01	2.97E-01	-0.19	1.865
1.2	tip	-1.91E-01	2.87E-01	1.12E-03	3.00E-01	3.44E-01	2.16	2.559
	90%	-2.45E-01	3.59E-01	2.37E-03	2.99E-01	4.35E-01	2.17	2.933

Table D.11: Secondary parameters ϕ for blade root, blade tip, and 90% of span for a 100 meter blade undergoing cyclic pitch and with solar pressure present.

Pitch Freq. Ratio		ϕ_1	ϕ_2	ϕ_3	ϕ_4	Amplitude (rad)	Phase (rad)	Amp. Ratio w/Root
0.2	tip	9.08E-02	-2.74E-01	8.89E-03	3.08E-01	2.89E-01	-1.25	1.000
	90%	8.25E-02	-2.47E-01	7.97E-03	3.08E-01	2.60E-01	-1.25	0.978
0.4	tip	-1.10E-02	2.95E-01	-7.64E-03	2.79E-01	2.95E-01	1.61	1.031
	90%	1.74E-02	2.79E-01	-8.28E-03	2.78E-01	2.80E-01	1.51	1.000
0.6	tip	-3.02E-02	1.98E-02	5.61E-04	6.26E-01	3.61E-02	2.56	0.621
	90%	-1.22E-02	5.58E-03	2.39E-04	6.28E-01	1.35E-02	2.71	0.608
0.8	tip	-1.63E-01	2.51E-02	3.09E-03	5.02E-01	1.65E-01	2.99	0.956
	90%	-1.19E-01	3.81E-02	2.03E-03	5.01E-01	1.25E-01	2.83	0.892
1.0	tip	-7.49E-02	1.56E-01	-2.91E-03	2.83E-01	1.73E-01	2.02	1.774
	90%	-6.70E-02	1.45E-01	-2.83E-03	2.82E-01	1.60E-01	2.00	1.710
1.2	tip	5.50E-01	1.37E-01	-1.83E-03	7.43E-01	5.67E-01	0.24	2.812
	90%	5.15E-01	1.84E-01	-2.33E-03	7.45E-01	5.47E-01	0.34	3.084

Table D.12: Secondary parameters ϕ for blade root, blade tip, and 90% of span for a 1000 meter blade undergoing cyclic pitch and with no solar pressure present.

Pitch Freq. Ratio		ϕ_1	ϕ_2	ϕ_3	ϕ_4	Amplitude (rad)	Phase (rad)	Amp. Ratio w/Root
0.2	tip	1.84E-02	7.58E-02	3.55E-04	3.69E-01	7.80E-02	1.33	0.626
	90%	1.11E-02	2.93E-02	8.07E-05	3.67E-01	3.14E-02	1.21	0.564
0.4	tip	5.37E-02	1.34E-02	-1.64E-03	3.08E-01	5.54E-02	0.24	0.631
	90%	3.92E-02	1.87E-02	-1.20E-03	3.10E-01	4.34E-02	0.45	0.627
0.6	tip	-5.82E-03	-7.67E-02	6.03E-04	3.62E-01	7.69E-02	-1.65	0.794
	90%	-2.78E-02	4.47E-02	-1.38E-03	3.10E-01	5.27E-02	2.13	0.725
0.8	tip	-5.90E-02	-3.52E-02	3.05E-03	3.05E-01	6.87E-02	-2.60	0.913
	90%	-4.79E-02	-2.88E-02	2.38E-03	3.06E-01	5.59E-02	-2.60	0.898
1.0	tip	1.71E-01	1.96E-02	-5.16E-03	2.93E-01	1.72E-01	0.11	1.665
	90%	1.39E-01	-3.41E-03	-3.45E-03	2.91E-01	1.39E-01	-0.02	1.493
1.2	tip	2.66E-01	-4.40E-01	9.90E-03	3.06E-01	5.14E-01	-1.03	2.282
	90%	-2.74E-01	-1.99E-01	1.14E-02	3.10E-01	3.39E-01	-2.51	2.932

Table D.13: Secondary parameters ϕ for blade root, blade tip, and 90% of span for a 1000 meter blade undergoing cyclic pitch and with solar pressure present.

Pitch Freq. Ratio		ϕ_1	ϕ_2	ϕ_3	ϕ_4	Amplitude (rad)	Phase (rad)	Amp. Ratio w/Root
0.6	tip	2.81E-02	-6.06E-02	-8.70E-04	3.35E-01	6.68E-02	-1.14	0.724
	90%	-3.76E-02	-2.95E-02	1.28E-03	3.12E-01	4.78E-02	-2.48	0.731
0.8	tip	1.08E-01	4.81E-02	-5.12E-03	3.04E-01	1.18E-01	0.42	1.022
	90%	9.27E-02	3.99E-02	-4.27E-03	3.04E-01	1.01E-01	0.41	0.975
1.0	tip	-1.46E-01	2.71E-02	2.99E-03	3.72E-01	1.49E-01	2.96	1.710
	90%	-6.38E-02	1.22E-02	1.34E-03	3.72E-01	6.49E-02	2.95	1.475
1.2	tip	-2.87E-01	-1.85E-01	1.74E-02	2.63E-01	3.42E-01	-2.57	1.349
	90%	-1.37E-01	-1.28E-01	9.71E-03	2.16E-01	1.87E-01	-2.39	2.171

Table D.14: Secondary parameters ϕ for blade root, blade tip, and 90% of span for a 1000 meter blade with battens every 50 m, undergoing cyclic pitch and with solar pressure present.

Pitch Freq. Ratio		ϕ_1	ϕ_2	ϕ_3	ϕ_4	Amplitude (rad)	Phase (rad)	Amp. Ratio w/Root
1.0	tip	3.05E-01	5.62E-02	-5.72E-03	2.89E-01	3.10E-01	0.18	1.900
	90%	2.72E-01	5.08E-02	-5.15E-03	2.89E-01	2.77E-02	0.18	1.804